# 5 Modelling active surface area development

## 5.1 Thermogravimetric analysis

Before analysing the experimentally obtained thermogravimetric data, it is sensible to review and categorise the factors that might affect the observed oxidation behaviours. In addition, methods to alleviate and reduce the number of these factors are discussed.

As is clear from previous discussions, there is still significant uncertainty about the exact kinetic mechanism. Firstly, the kinetic dependence on the reactant and product partial pressures should be taken into consideration. This is heavily affected by the choice of mechanism – whether it be a simple power law, Langmuir-Hinshelwood, a three-step semi-global mechanism or a more complex expression affected by surface heterogeneity. The choice of a highly crystalline graphitic material should mitigate the effects of microscopic surface site heterogeneity to a large extent, as compared with an amorphous material. Atomic surface heterogeneity as defined by the surface complex formation will be discussed shortly. The effect of the kinetic mechanism, depending on the gaseous composition, can be largely diminished by choosing pure oxygen as the gas reactant (operating under very high purge rates) and to a large extent conducting the kinetic study at relatively low reaction rates. This will ensure that product gas concentrations around the solid reactant are minimised, reducing their effect on the measured kinetics. Furthermore, by using pure oxygen at one atmosphere, the need to determine a reaction order, assuming a simple power law-based model is generally applicable, is simplified for comparing the kinetic parameters of different graphite samples analysed under the same conditions.

A related kinetic issue is the influence of the carbon-oxygen surface complexes. Depending on their nature, these can have an exceedingly complex influence on the reaction kinetics. Specifically, they can impart non-Arrhenius-type temperature dependencies and induce multiple reaction pathways. The possibility of transient versus stable surface complexes will have a direct influence on the ASA development since the ASA may be effectively reduced as a stable oxygen complex accumulates. This is assuming that the stable complex is not acting as a reactionary intermediate, as stated by several of the

investigations mentioned earlier. In the latter case its effect on the reaction rate will be even more complex. Given the uncertainty, mitigating this factor is difficult and it should therefore be taken into account during the modelling.

External mass transfer limitations are of special concern as these will negate the direct measurement of the kinetic parameters. A few experimental conditions may be adjusted to reduce the presence of these limitations. Since powdered samples are used in this investigation, the choice of sample size is an especially important parameter. Reducing the sample size will reduce the consumption of the reactant gas and reduce the likelihood of gas depletion towards the centre of the sample. However, when working with large flakes the matter of sample reproducibility may become an issue. Reducing the sample size reduces the number of flakes, thus reducing the averaging effect across all the many subtle microstructural variations that are possible in a given sample. This would compromise the repeatability of experiments with the same sample. Thus a trade-off is necessary between the sample size and the particle size present in the different graphite samples.

In this case too, using a high purge gas flow rate and a low reaction rate will lessen the probability of mass transfer limitations. A final consideration is sample holder geometry. In general, thermal analysis is conducted by placing the sample into a sample cup, in this case a 90 µl cup in platinum pans. However, gas flow in the cup will follow a complex pattern and the possibility of dead zones developing seems highly likely. Instead, it was decided to turn the cups upside down and use the flat bottom surface as the sample support. This allows smooth, even gas flow across the sample and the sample can be spread out over the pan into a thin layer. Based on the reaction rate and purge gas flow rate, the development of a concentration gradient in the flow direction due to a boundary layer was calculated to be negligible.

For the RFL graphite sample it was found that an additional limitation developed when the sample size was increased beyond 5 mg. In this case the reaction rate was found to develop an inverse relationship to the purge gas flow, i.e. when the purge gas flow was reduced, the reaction rate increased. This is the converse of the relationship expected for mass transfer limitations. Instead, it was deduced that a localised temperature rise was being generated. If the purge rate is increased, the heat produced by the sample is more readily removed and the

sample is at a comparatively lower temperature. It is generally assumed that the entire reaction chamber is at the same temperature. However, due to the decision to place the sample on the base of the cup, it is possible that a different temperature may be present in the sample which is not measured by the thermocouple in the beam. A solution would be to redesign the sample holder to have a flat surface with a solid base in direct contact with the thermocouple. However, since this effect was not noticeable below a sample size of 5 mg, a sample size of around 1–3 mg was chosen. The lower limit is based on repeated trials to confirm sample-to-sample repeatability for the different graphite samples, with larger flakes requiring a larger sample.

Internal mass transfer limitations should also be considered. In the case of the synthetic graphite (SNG) it is clear that these are likely to be of significance. The situation is further complicated by the unique porosity that develops in the synthetic material during oxidation. This may lead to mass transfer limitations becoming active only after the oxidation has proceeded to some extent, due to the creation of narrow slit-like pores along the basal plane of the particles. To alleviate internal mass transfer limitations, a small particle size should be chosen. Unfortunately, for the same sample size this may lead to the development of external mass transfer limitations. For the RFL and Kish graphite samples this consideration is largely negated by the observation that the particles are non-porous flakes.

The particle size will directly influence the reaction rate of different samples by changing the ASA. Ideally, particles of the same size should be compared to reduce this effect, at least during the initial stages of reaction before other microstructural developments occur. This consideration is accentuated by the presence of a particle size distribution rather than a collection of particles of the same size. For the RFL, PRFL and CPRFL these effects are negated by the original ethanol washing and sieving procedure.

A key consideration that was analysed in depth in the previous section is the effect of the particle microstructure. These factors cannot be removed and must be taken into consideration during modelling. Of special importance are:

- The crystallite domain sizes
- The particle shape and geometry

- Inherent flaws within the macrostructure
- Particle agglomeration
- Particle damage due to milling
- Precursor type, e.g. needle coke or derived from binder pitch

Because of the presence of two distinct, very different microstructures in the synthetic graphite, the issue of sample reproducibility may be even greater in this sample than in the other samples. Finally, the presence of impurities will also massively affect the observed behaviours in very wide variety of ways. Given the fact that the type and concentration of impurities present in these samples are largely unknown, these effects are impossible to mitigate and should be taken into consideration during modelling.

Other factors also influence the oxidation, which are not directly attributable to the sample under consideration. These include issues such as sample handling and the limits of TGA performance. A key consideration during sample handling is contamination. Since the TGA cups are generally reused for different samples, sample-to-sample cross-contamination is a large concern. To eliminate this issue a single cup is used for each graphite sample. The cup is cleaned by scrubbing with ethanol and a new paper towel between each run. If it becomes necessary to use a cup previously used for another sample for a new sample, the cup is first polished with fine sandpaper to reveal a completely virgin surface. This procedure is applied to all cups from time to time to ensure that no accumulation of minute quantities of contaminants is taking place.

As discussed previously, TGA repeatability is a concern. This is affected by many sample-related issues but measurement accuracy will vary from experiment to experiment, even under identical conditions. These effects cannot be eliminated and will add to the statistical variance of the measurements. They will determine the number of repeat experiments necessary to obtain a statistically significant result. However, certain effects are present that have a fairly repeatable effect on the measured data. Two issues were found to be of significant concern: firstly, time-based drift in the TGA mass signal, and secondly, gas buoyancy effects.

Modern TGA machines have a superb mass resolution, of the order of $10^{-4}$ mg for the machine utilised in this investigation. This would seem to imply that an extremely low reaction temperature can be chosen to alleviate the negative effects caused by high reaction rates. At this resolution the machine would detect reaction rates of the order of 1 x $10^{-7}$ mg/h. However, the manufacturer stated that baseline drift for the TGA model used in this investigation is 0.025 mg/h. The observed value was around 0.02 mg/h, but it is dependent on the reaction temperature during isothermal experiments. For a 2 mg sample this equates to a 1% drift over 1 h. In general, this implies that experiments lasting anything longer than 10 h will have an inherent uncertainty of at least 10% in addition to any sample-to-sample variations. This is very significant and places a severe limitation on the possible experimental conditions. Thus the temperature chosen should be high enough to ensure a reaction rate of at least 0.2 mg/h to negate the drift effect.

During isothermal experiments the gas atmosphere is changed from inert to reactive. In this case argon with an atomic mass of 40 and oxygen with an atomic mass of 32 are used. Since the densities of these gases differ by 5%, when changing from inert to oxidising the buoyancy of the beams in the gas should increase by a proportional amount. Thus the beams will measure different sample masses under these conditions. This effect is further accentuated by the fact that during the gas change the atmosphere in the reaction chamber is highly turbulent, especially at higher purge gas flow rates.

Assuming the beam drift and gas change effects are repeatable, these issues can be largely mitigated by performing control experiments with an empty sample holder before each experiment under identical reaction conditions. These signals are then subtracted from the measured signals during the actual experiment to, at most, partially remove these effects from the observed signals. Although beam buoyancy effects are not a concern during non-isothermal experiments, drift will still occur. Thus this compensation was done for each data set reported in this investigation.

## 5.2 Solid state kinetic equations for graphite

As a starting point for the solid state kinetic approach, Eqs (2.43) and (2.45) are combined to give the general expression for the reaction rate ($R_{T0}$):

$$\mathrm{R}_{\mathrm{T0}} = \frac{d\alpha}{dt} = k(T) f(\alpha) = k_0 e^{-\frac{E_A}{RT}} f(\alpha) \quad (5.1)$$

For the time being the accommodation function is set to one, i.e. assuming a simple power law-based expression for the pressure dependence with the partial pressure of the oxygen being one in all cases. However, when required, i.e. under special, limited conditions, where the partial pressure of oxygen is not one, the power law accommodation function is used, as mentioned. In this case *k (T)* has units of g carbon reacted/g carbon present at the start of the experiment/s. At this point three different approaches for relating Eq. (5.1) to experimental data are possible. A few assumptions must be made first regarding the solid reactant:

- Ideal flakes are assumed to be solid, i.e. non-porous, homogenous and perfectly crystalline, thus having a density of $\rho_c$ = 2.26 g/cm$^3$.
- These ideal flakes are assumed to be roughly circular, flat discs.

Thus the ideal graphite flake is modelled by the flat, circular disc shown in Figure 5-1 with thickness (*d*) and radius ($r_t$). The basal plane is orientated along the surface of the disc, thus the disc only reacts from the edges.

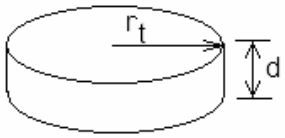


Figure 5-1: Ideal graphite flake

For this circular disc the expressions for the active surface area (*ASA*) and mass (*m*) at any time (*t*) are given by:

$$ASA = 2\,\pi\, r_t\, d \quad (5.2)$$

$$m_t = \pi\, r_t^2\, d\, \rho_c \quad (5.3)$$

The approach widely followed in solid state kinetics, as pointed out by Khawam and Flanagan [248], is to assume that the reaction rate is determined by the progression of the reaction interface towards the centre of the particle, in which case the following relationship is applicable:

$$r_t = r_{t=0} - vt \quad (5.4)$$

where the radius is some characteristic dimension of the particle and will depend on the geometry and *v* is the constant edge-recession rate. The subscript *0* is used to denote the value of any particular variable at the start of the experiment and the subscript *t* denotes the same value at any time.

Since the reaction proceeds only from the edges, i.e. the basal plane is completely inert, the thickness remains constant throughout. Hence the dimensionless degree of conversion may be written as:

$$\alpha = \frac{m_0 - m_t}{m_0} = \frac{\pi\ r_{t=0}^2\ d\ \rho_c - \pi\ r_t^2\ d\ \rho_c}{\pi\ r_{t=0}^2\ d\ \rho_c} = 1 - \frac{r_t^2}{r_{t=0}^2} \quad (5.5)$$

By substituting Eq. (5.4) into Eq. (5.5) and taking the derivative, the following expression is obtained:

$$\frac{d\alpha}{dt} = \frac{2v}{r_{t=0}}(1-\alpha)^{0.5} \quad (5.6)$$

If one assumes that:

$$k(T) = \frac{v}{r_{t=0}} \quad (5.7)$$

then the conversion function is found to be:

$$f(\alpha) = n(1-\alpha)^{\frac{n-1}{n}} \quad (5.8)$$

with n = 2 as expected from Table 2-12 for the two-dimensional case under consideration.

However, difficulties arise when trying to interpret the reaction rate constant given by expression (5.7) for different particles. The dimensions of *k(T)* mentioned earlier, are difficult to reconcile with the units of the edge recession rate *v*, which from expression (5.4) are clearly $m.s^{-1}$. The reason for this is that the stipulation of reaction rate solely as a function of edge recession rate already contains inherent assumptions regarding the regularity of the particle, the characteristic dimension and well defined active surface area development. Hence, it is very difficult to relate such dimensions to generally reported reaction rate data from different studies for different, real particles.

Furthermore, this case is specific only to two-dimensional disc-like particles and three-dimensional spherical particles, the reason being the assumption that the reaction rate is linear, based on the particles' characteristic dimension. For complex two-dimensional particles that do not have a readily definable characteristic dimension, such as those shown in Figure 5-2, the approach cannot be generalised.

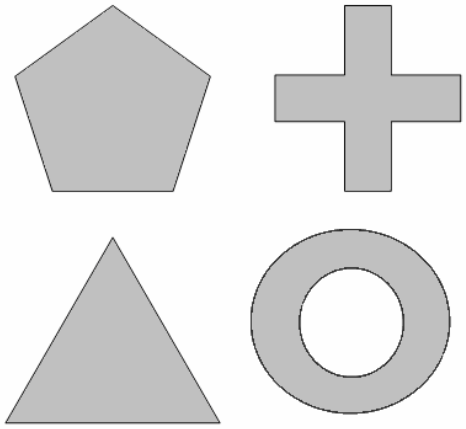

Figure 5-2: Complex particle geometries

However, as was recently shown by the author of this thesis and co-workers [345], it is possible to extend this approach to such particles not on the basis of a characteristic dimension, but by applying Eq. (5.4) to all the edges of complex geometries simultaneously, among others those shown in Figure 5-2. However, the problem mentioned earlier of relating such a rate constant to generally measured reaction rate data from different studies with unknown

particle configurations still remains. To generalise this approach, two more assumptions are needed:

- Reaction rate is proportional solely to the number of active sites, i.e. the type of surface complex present, and secondary reactions are ignored. Thus the reaction rate is assumed to be governed by a single-step mechanism at the active site. Since the accommodation function has been set to one, this is most conveniently thought of as "desorption control".
- The surface area occupied by a single carbon atom is 0.083 $nm^2$, as assumed by Laine *et al.* [132]. Thus the surface site density, $\rho_{ASA}$, is 2.403 x $10^{-4}$ g of reactive carbon/$m^2$ ASA, using Avogadro's number and the atomic mass of carbon.

Ideally, the number of carbon atoms reacted in a given time period is proportional to the number of carbon atoms exposed at the reactive edge. This is expressed mathematically as:

$$-\frac{dn}{dt} = k_i(T)\, n_{edge} \quad (5.9)$$

By multiplying both sides of the equation by Avogadro's number and the atomic mass of carbon, the expression can be converted to mass:

$$-\frac{dm}{dt} = k_i(T)\, m_{edge} \quad (5.10)$$

As a basis, an infinitesimal cube on the side of an infinite sheet is considered, as shown in Figure 5-3. The intrinsic reaction rate constant, $k_i\,(T)$, has units of g carbon reacted/g of reactive carbon/s and is related to the active surface area rate constant, $k_{ASA}\,(T)$, by the active site density, $\rho_{ASA}$.

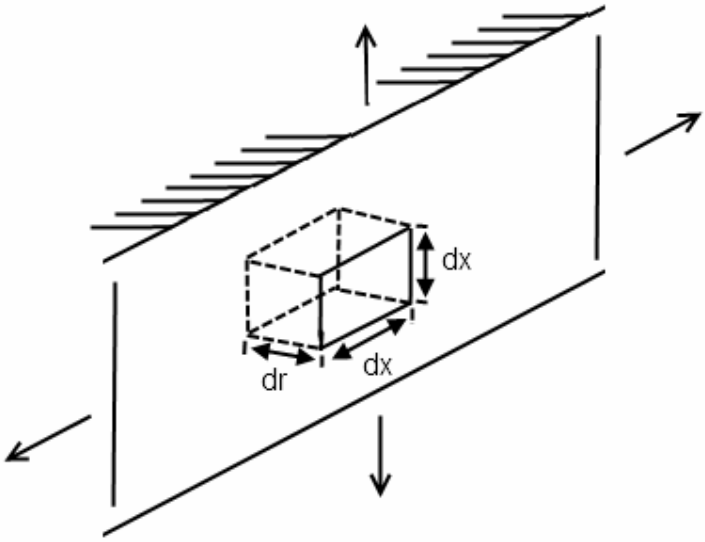


Figure 5-3: Infinitesimal cube in an infinite flat sheet

The mass of the cube is given by:

$$m_{cube} = dr\ dx\ dx\ \rho_c \quad (5.11)$$

By taking the derivative of Eqs (5.4) and (5.11), one finds that:

$$\frac{dr_t}{dt} = -v \quad (5.12)$$

$$\frac{dm}{dt} = dx^2 \rho_c \frac{dr_t}{dt} \quad (5.13)$$

Substituting Eq. (5.12) into Eq. (5.13) and substituting the result into Eq. (5.10) gives the expression:

$$dx^2 \rho_c\ v = k_i(T)\, m_{edge} \quad (5.14)$$

Using the active site density, the mass of edge atoms may be calculated as follows:

$$m_{edge} = \rho_{ASA}\ dx^2 \quad (5.15)$$

Substituting into Eq. (5.14) and simplifying gives:

$$v = \frac{k_i(T)\,\rho_{ASA}}{\rho_c} \quad (5.16)$$

Thus the ASA rate constant, $k_{ASA}(T)$, is related to the edge-recession rate by:

$$v = \frac{k_{ASA}(T)}{\rho_c} \quad (5.17)$$

By substituting Eq. (5.17) into Eq. (5.6) and multiplying both sides of the expression by the initial mass of the disc, one obtains:

$$m_0 \frac{d\alpha}{dt} = \frac{2\,k(T)\,\rho_{ASA}}{r_{t=0}\,\rho_c}(1-\alpha)^{0.5}\pi\, r_{t=0}^2\, d\, \rho_c \quad (5.18)$$

which may be simplified as:

$$m_0 \frac{d\alpha}{dt} = k(T)\,\rho_{ASA}\, ASA_0\,(1-\alpha)^{0.5} \quad (5.19)$$

However, Eq. (5.5) may be rewritten as:

$$r_t = r_{t=0}\,(1-\alpha)^{0.5} \quad (5.20)$$

Substituting this into Eq. (5.2) for the ASA gives:

$$ASA = 2\,\pi\, r_{t=0}\, d\,(1-\alpha)^{0.5} = ASA_0\,(1-\alpha)^{0.5} \quad (5.21)$$

Thus one finds that, in general:

$$\frac{d\alpha}{dt} = \frac{ASA\,k_{ASA}(T)}{m_0} \quad (5.22)$$

which may be rewritten as:

$$\frac{d\alpha}{dt} = ASA\, k^0_{ASA}(T) \quad (5.23)$$

This expression is valid for any starting geometry with any possible, conversion-based, active surface area development. This expression is far more general than the original solid state kinetic expression since the conversion function may now be directly thought of as the active surface area. This is very convenient since it implies that if the reaction rate expression (5.23) is divided by the initial active surface area, the conversion function must start at one. Thus the true active surface area-based conversion function expression for the disc is not expression (5.8) but rather:

$$f(\alpha) = ASA = ASA_0(1-\alpha)^{0.5} \quad (5.24)$$

or, in general:

$$f(\alpha) = ASA_0\, f^0(\alpha) \quad (5.25)$$

where $f^0(\alpha)$ is the normalised conversion function, which always starts at one. Thus the generalised expression for the reaction rate given in Eq. (5.1), but applicable to any single-step reaction where the active site distribution governs the reaction rate, is:

$$\mathrm{R}_{\mathrm{T0}} = \frac{d\alpha}{dt} = k^0_{ASA} \exp\left(\frac{-E_A}{RT}\right) ASA_0\, f^0(\alpha) \quad (5.26)$$

However, this definition of the reaction rate is slightly different from that generally found in the carbon literature (Eq. 2.27) as defined by Radovic and co-workers [149] and Ahmed and Back [203]. In those studies the reaction rate ($R$) has units of g carbon reacted/g carbon remaining at any time/s, thus:

$$R_R = \mathrm{R}_{\mathrm{T0}} \frac{m_0}{m} = \frac{1}{1-\alpha} \frac{d\alpha}{dt} = k_f(T) C_f \quad (5.27)$$

and, in general:

$$R_R = k^0_{ASA}(T) ASA_0 \frac{f^0(\alpha)}{(1-\alpha)} \quad (5.28)$$

Thus:

$$R_R = k_{ASA}(T) \frac{ASA_0 f^0(\alpha)}{m_0(1-\alpha)} = k_{ASA}(T) \frac{ASA}{m} \quad (5.29)$$

## 5.3 Ideal solid state kinetic modelling

Based on Eq. (5.26), an ideal model can be constructed for the case of the shrinking disc discussed in the previous section. The kinetic parameters shown in Table 5-1 are estimated from the values provided in the literature survey (Section 2.10), where $k_{ASA}(T) = k_{ASA}\, exp(-E_A/RT)$:

Table 5-1: Ideal kinetic parameters

| | | |
|---|---|---|
| $k_f$ | $1 \times 10^{10}$ | g/g/s |
| $k_{ASA}$ | $2.403 \times 10^6$ | g/m$^2$/s |
| $E_A$ | 180 | kJ/mol |

The specific surface area given in Chapter 3 by the supplier for as-received RFL graphite is 0.8 m$^2$/g. From visual inspection of the SEM images the thickness of an RFL graphite flake is estimated to be around 20 µm, with an average width of 225 µm obtained by sieving. Based on these dimensions and the graphite crystal density, the specific surface area may be estimated as 0.05 m$^2$/g, which is significantly lower than the measured value. This may be the result of several factors, including the removal of a significant fraction of finer material during sieving, the real flake geometry differing from the ideal disc shape and possibly also due to an erroneous measurement of such a low surface area

value. Based on the flake dimensions, the specific active surface may be calculated as 0.008 $m^2/g$, the value that will be used in the simulation. Using these parameters and Eq. (5.26), an ideal incremental step simulation can be created as follows:

- Firstly, a time step is chosen. The choice of step size is critical to ensure a good resolution while not making the simulation too long before 100% conversion is achieved. The resolution must be such that the incremental reaction occurring between steps is very small. Through trial and error a step size of 0.01 min was chosen.
- Now the time vector can be calculated, starting at $t_0$ = 0 minutes and incrementing by the chosen time step up to some value that ensures 100% conversion, in this case approximately 3 h.
- Next, the temperature vector may be calculated. This can be simply a constant value for isothermal simulations, or it can be a linear function of time, such as: $T = T_0 + \beta t$ for non-isothermal simulations. In the case of the latter, the choice of starting temperature is also critical. This value must be chosen such that the reaction rate is not too low at the initial point, i.e. so that it does not take a very long time before the simulated reaction rate reaches a sizeable value; this is, of course, also dependent on the ramp rate. Furthermore, this value must not be too high, since then the initial portion of the non-isothermal experiment will not be simulated as the reaction rate will already be comparatively high. For the initial simulation a ramp rate of $\beta$ = 3 ºC/min and a starting temperature of $T_0$ = 400 ºC were chosen by trial and error.
- Next, the reaction rate constant $k_{ASA}$ can be calculated as a function of the temperature vector just constructed and the reaction rate constant and activation energy given in Table 5-1.
- The starting conversion at $t_0$ is taken as zero. Using this, the initial value for the conversion function can be calculated $f(\alpha) = f(0) = 1$.
- This value can be multiplied by the reaction rate constant, the initial active surface area (estimated as $ASA_0$ = 0.008 $m^2/g$) and the time step ($dt$) to calculate the expected change in conversion ($d\alpha$) for that time step.

- Finally, the conversion vector may be constructed as $\alpha_t = \alpha_{t-1} + d\alpha$.

Such a simulation was constructed in Microsoft Excel®. The simulation result for the dimensionless conversion for the ideal disc shape, $f(\alpha) = (1 - \alpha)^{0.5}$, the chosen kinetic values and the selected ramp rate is shown in Figure 5-4 and the reaction rate is shown in Figure 5-5.

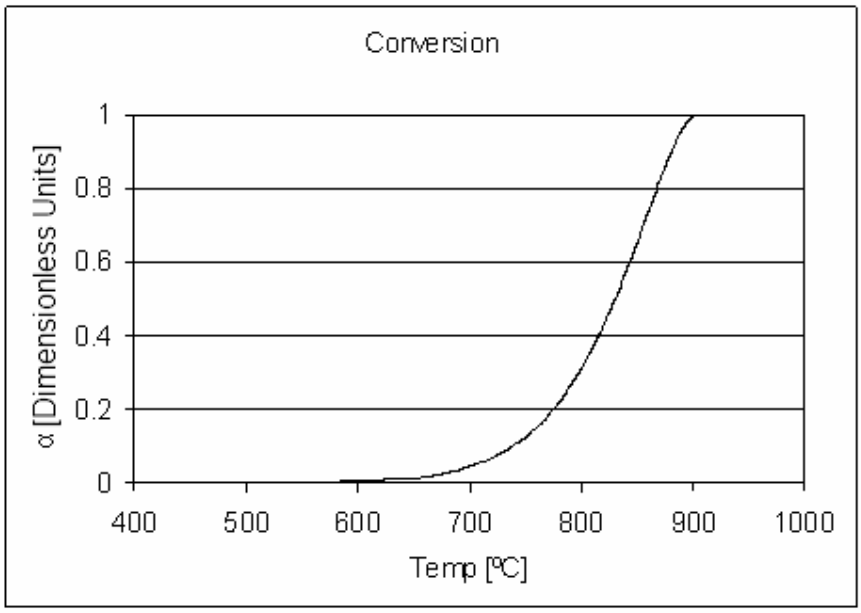


Figure 5-4: Ideal disc simulation – conversion

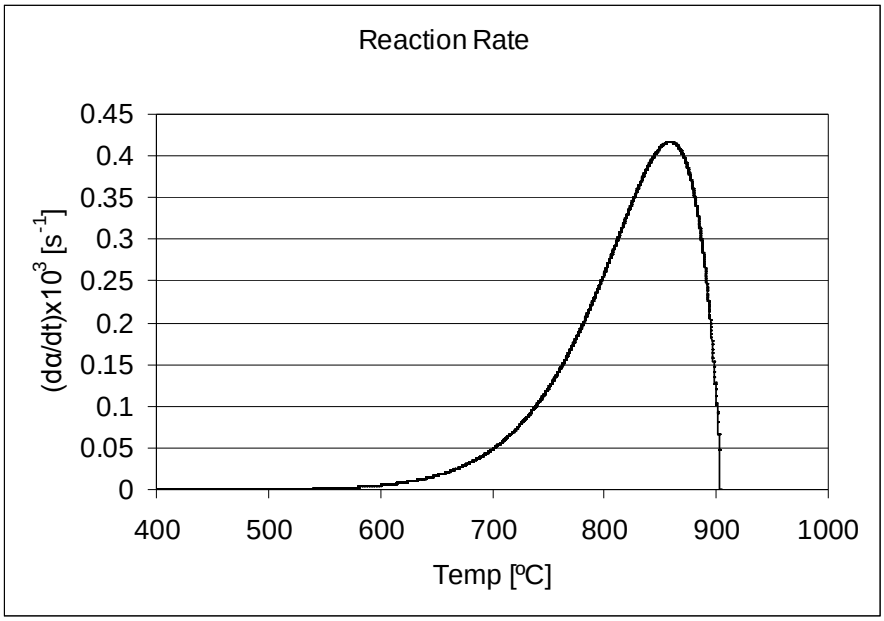


Figure 5-5: Ideal disc simulation – reaction rate

It is trivial, but to show that the simulation is functioning correctly, the conversion function may be calculated by dividing the reaction rate by the calculated rate constant and the initial active surface area. A plot of this conversion function against conversion is shown in Figure 5-6.

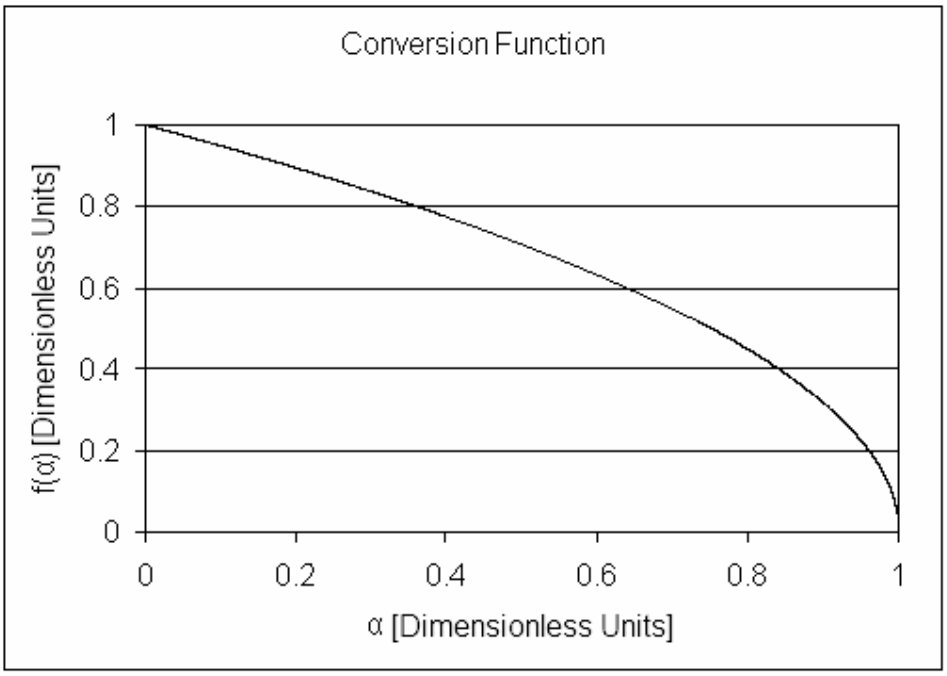


Figure 5-6: Ideal disc simulation – conversion function

It is now possible to apply the solid state kinetic methodology suggested by Galwey [265] in Section 2.12. This approach may be summarised as follows:

- A step-wise increment in the conversion is chosen; as a starting point $\Delta\alpha_i$ = 0.001 was chosen. Using this, a vector from zero to full conversion may be constructed.
- Next, the time interval ($\Delta t_i$) to complete each incremental step in conversion is calculated.
- The mean temperature for each conversion step is calculated from the reaction temperature before and after each step.
- Then, assuming a linear rate of reaction within each small reaction interval, the (zero-order) reaction rate constant can be calculated as $k_i = \Delta\alpha_i/\Delta t_i$.

- The experiment must be repeated for at least two different non-isothermal ramp rates. Then, at a single conversion point, the two or more calculated reaction rate constants can be used to calculate the activation energy directly.

The result of this calculation is shown in Figure 5-7, using two simulated temperature ramp rates of 3 and 5 ºC/min.

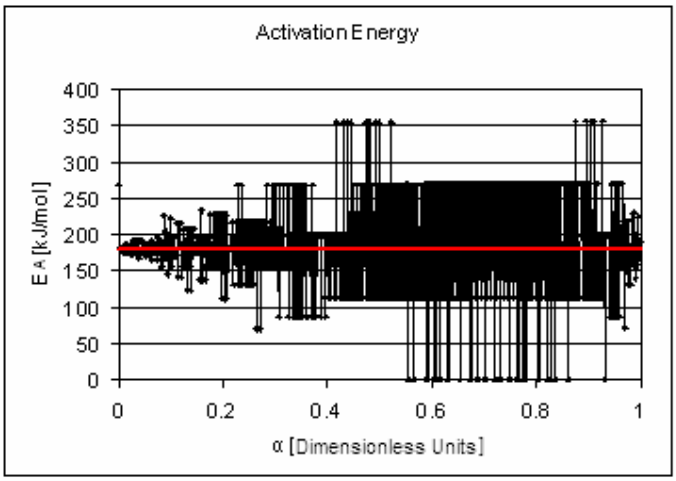


Figure 5-7: Activation energy – Galwey's method of small intervals

As can be seen from Figure 5-7, a significant amount of spread is present in the estimated activation energy, despite this being a perfect, ideal simulation. The activation energy is estimated as 183 ± 68.5 kJ/mol, using a simulated value of 180 kJ/mol. The reason for the spread is the decision to use the change in time over fixed conversion intervals. In most instances the change in time during these intervals is simply too small. A solution might be to increase the chosen conversion interval ($\Delta\alpha_i$). As shown in Figure 5-8, this significantly improves the estimation for $\Delta\alpha_i = 0.01$.

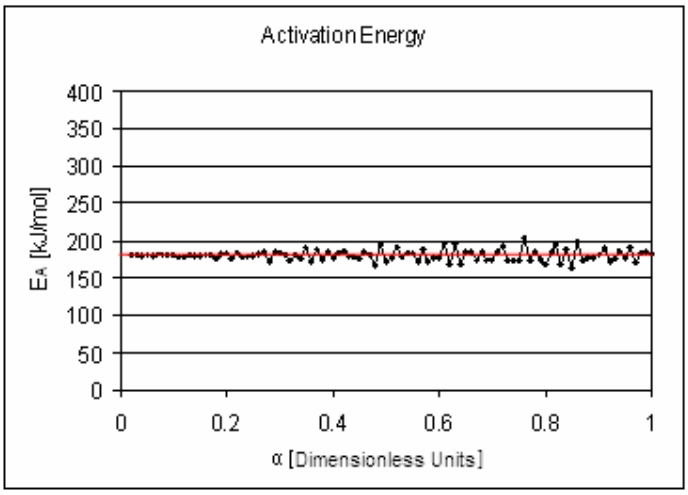


Figure 5-8: Activation energy – Galwey's method

The calculated activation energy is now 180 ± 7.2 kJ/mol, which is very close to the simulated value. One very important point to take note of is that this method is independent of the underlying conversion function. The extent to which this is true can be easily evaluated by the simulation using a variety of different conversion functions. For example, when the fairly arbitrary conversion function shown in Figure 5-9 is used, the predicted activation energy is hardly affected. The uncertainty is very slightly increased to ± 7.5 kJ/mol for the activation energy plot shown in Figure 5-10. Thus even with a perfect model which contains no uncertainty, this approach imparts a standard deviation on the estimated activation energy value of more than 4%.

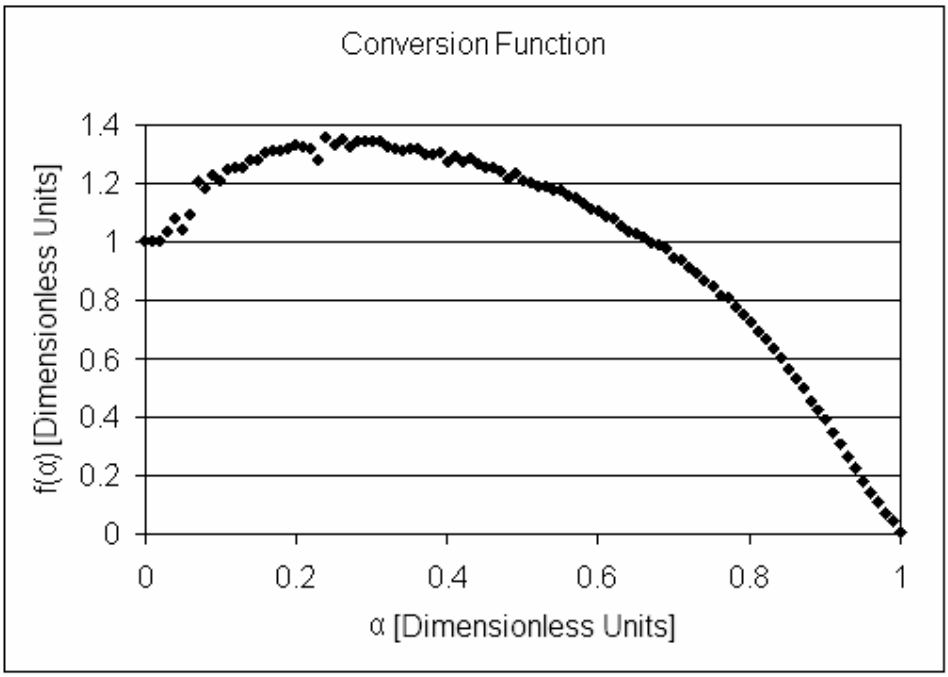


Figure 5-9: Arbitrary conversion function

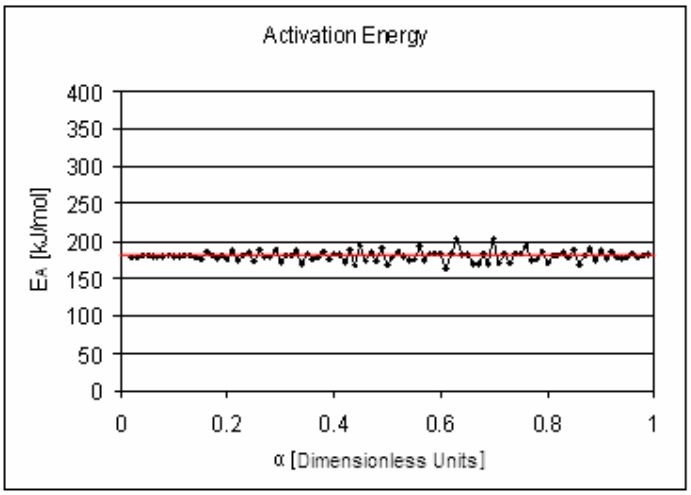


Figure 5-10: Activation energy – Arbitrary conversion function

Thus this method is sensitive only to effects that truly influence the activation energy or change the active conversion function, i.e. when another mechanism becomes rate controlling. This is valid only if the conversion function can be pinned to a single mechanism. For real samples it is difficult to discern whether regions of the observed conversion function represent the action of the true mechanism, e.g. active surface area development, or secondary effects such

as the actions of metallic catalysts. An alternative method for estimating the activation energy from non-isothermal data could be formulated as follows. Rewriting Eq. (5.26), one finds:

$$\frac{d\alpha / dt}{f^0(\alpha)} = ASA_0 k_{ASA} \exp\left(\frac{-E_A}{RT}\right) \quad (5.30)$$

Taking the natural logarithm of both sides and multiplying by minus one gives:

$$-\ln\left(\frac{d\alpha / dt}{f^0(\alpha)}\right) = \frac{E_A}{RT} - \ln\left(ASA_0 k_{ASA}\right) \quad (5.31)$$

Since the last term on the right-hand side of Eq. (5.30) is simply a constant, plotting the left-hand side of the expression against 1/T should yield the activation energy as the slope of the curve, in the traditional Arrhenius fashion. However, the reaction rate ($d\alpha/dt$) can be generated using a given conversion function and the simulation mentioned earlier. Then a different conversion function can be used to construct the Arrhenius plot. This is equivalent to assuming the incorrect conversion function model to interpret an experimental data set. Four different conversion functions were judiciously chosen for this comparison, as shown in Figure 5-11.

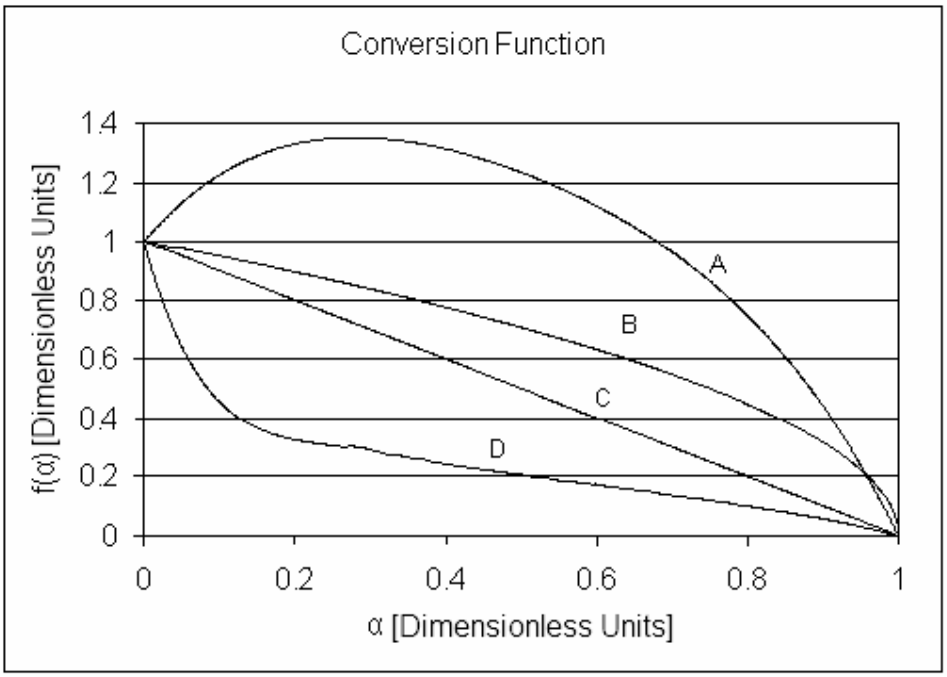


Figure 5-11: Possible conversion functions

Conversion function B in Figure 5-11 is simply the ideal disc model, whereas function C is the same model but with a first order conversion function, i.e. $f(\alpha) = 1 - \alpha$. These two models are fairly similar, accordingly the Arrhenius plot resulting from using the disc model as the true model and the first-order model as the assumed conversion function to determine the activation energy, is shown in Figure 5-12. For clarity, the straight line that should be obtained if the two models are identical is added to the plot as the dashed line.

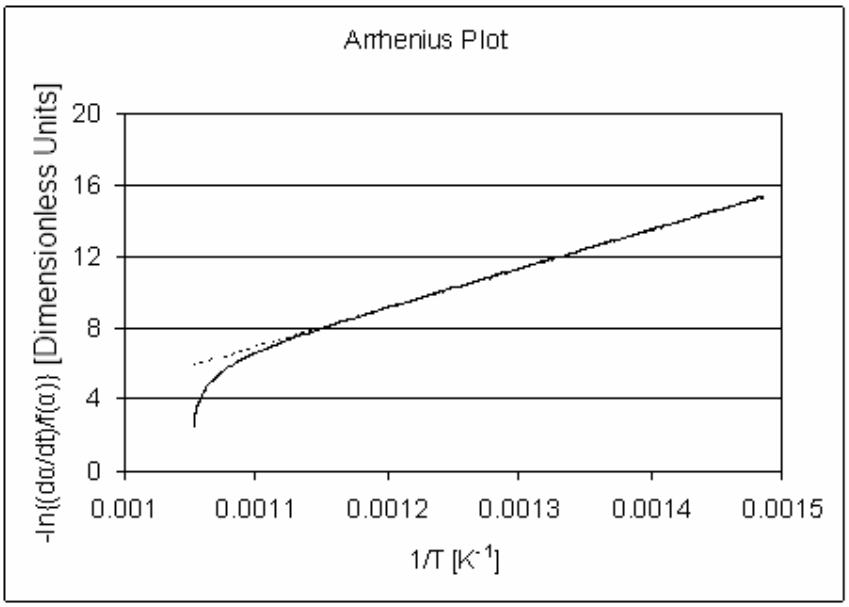


Figure 5-12: Arrhenius plot for conversion function mismatch

As expected, the two lines are very similar and in this case a minimal error would be made if the data up to around 600 ºC were used to estimate the activation energy. This corresponds to using the data from zero conversion up to 21%, i.e. the initial portion of the reaction curve. In general, it was found, using various combinations of the conversion functions in Figure 5-11, that there is always a roughly linear region in the data which can be used to fit a straight line. In most cases the linear fit is very good, as indicated by a high correlation coefficient ($R^2$). Thus the data can be plotted and a suitable linear region found to be used to estimate the true activation energy of 180 kJ/mol. The results for various combinations of this procedure are shown in Table 5-2.

Table 5-2: Results for conversion function mismatch ($E_A$ = 180 kJ/mol)

| True conversion function | Assumed conversion function | Correlation coefficient ($R^2$) | Conversion range used (%) | Calculated activation energy (kJ/mol) | % Error |
|---|---|---|---|---|---|
| A | B | 0.999 | 0 – 80 | 193 | 7 |
| D | B | 0.994 | 0 – 65 | 151 | -16 |
| A | C | 0.991 | 0 – 100 | 210 | 17 |
| D | C | 0.996 | 0 – 98 | 161 | -10 |
| A | D | 0.989 | 0 – 100 | 228 | 27 |

Despite having excellent correlation coefficients, i.e. very good linear fits, and utilising fairly large regions of conversion, the values for the estimated activation energy have quite large errors. The size of the error does vary as the difference in conversion functions increases, e.g. the error between combination AD is larger than that between either AB or AC. Furthermore, if the real conversion function is larger than the assumed function, the error is consistently positive, i.e. the activation energy is overestimated. The situation is significantly worsened if a slightly lower true activation energy is chosen, as is shown in Table 5-3 for $E_A$ = 150 kJ/mol.

Table 5-3: Results for conversion function mismatch ($E_A$ = 150 kJ/mol)

| True conversion function | Assumed conversion function | Correlation coefficient ($R^2$) | Conversion range used (%) | Calculated activation energy (kJ/mol) | % Error |
|---|---|---|---|---|---|
| A | B | 0.9995 | 0 – 74 | 183 | 22 |
| D | B | 0.996 | 0 – 85 | 103 | -31 |
| A | C | 0.995 | 0 – 100 | 220 | 47 |
| D | C | 0.981 | 0 – 85 | 124 | -17 |
| A | D | 0.996 | 0 – 100 | 246 | 64 |

The situation in both cases is worst for the two most dissimilar conversion functions. This indicates the danger involved in assuming the incorrect form of the underlying conversion function, despite getting what appears to be excellent Arrhenius plots. Using this approach can lead to serious errors in the estimated activation energy.

## 5.4 Experimental solid state kinetic modelling

The method suggested by Galwey [265] to estimate the activation energy has been applied to all the graphite samples considered in this study. All samples were subjected to at least two heating rates of between 2 and 6 ºC/min, in IG oxygen. The results are shown in Figure 5-13 to Figure 5-20. The area indicated by the green box was used for estimating the activation energy.

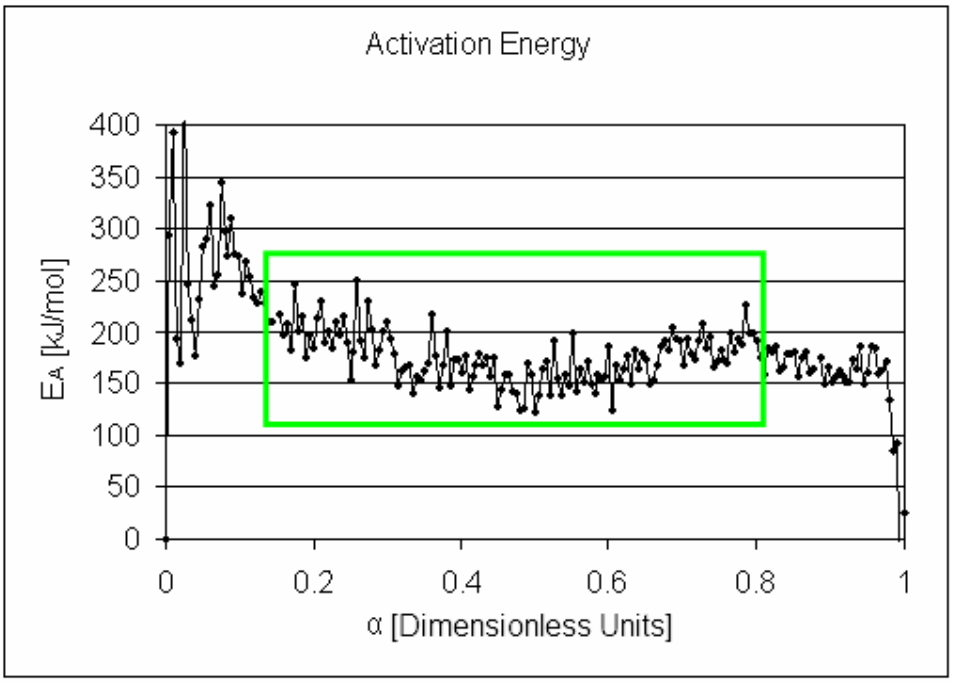


Figure 5-13: Galwey's method for NNG

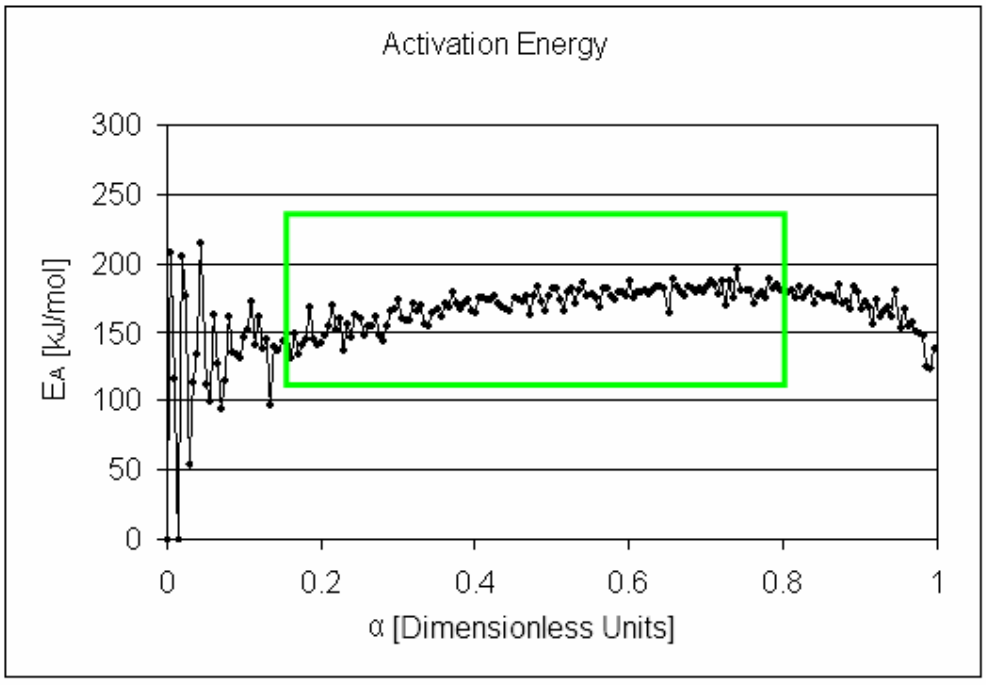


Figure 5-14: Galwey's method for NSG

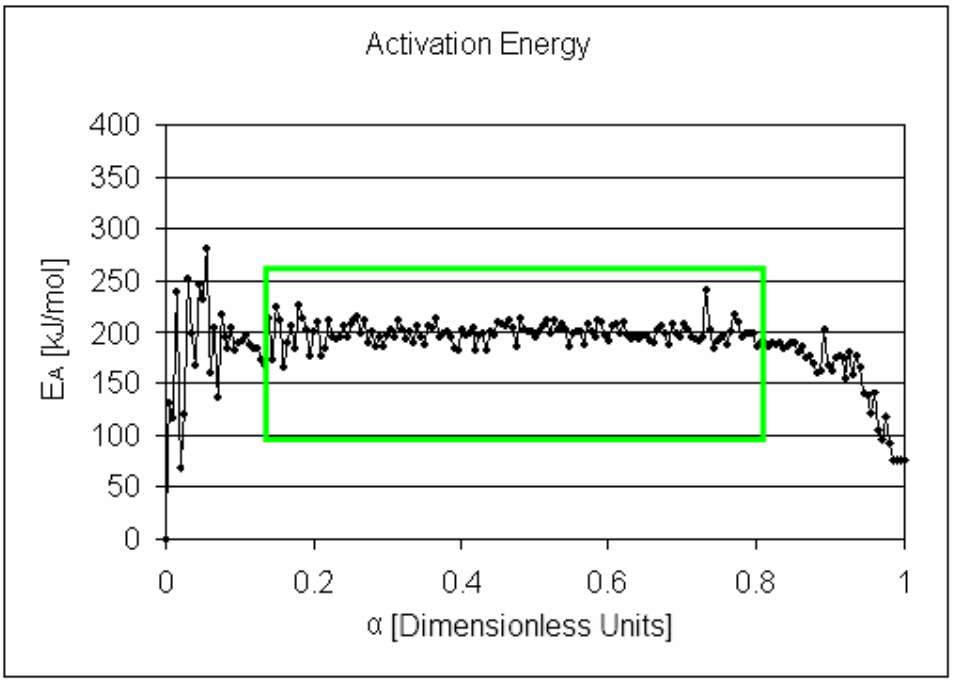


Figure 5-15: Galwey's method for ZNG

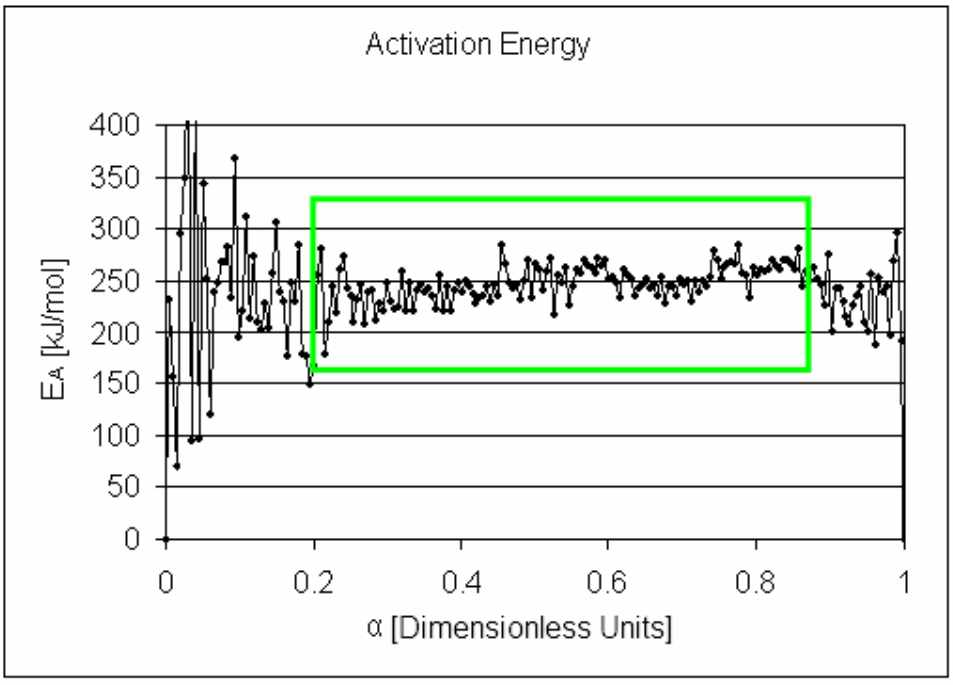


Figure 5-16: Galwey's method for KISH

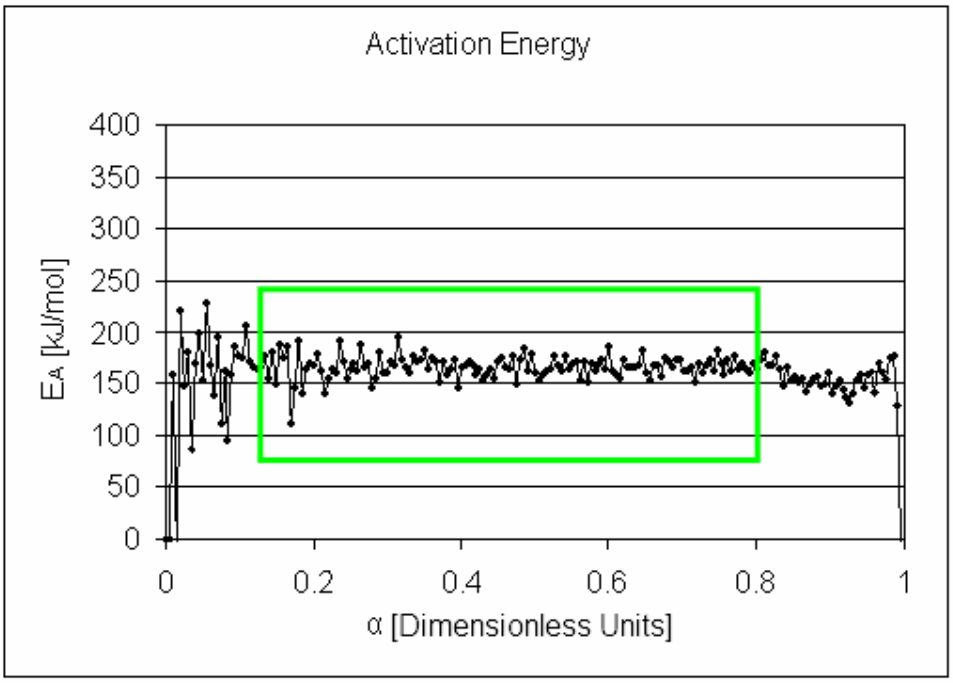


Figure 5-17: Galwey's method for FSG

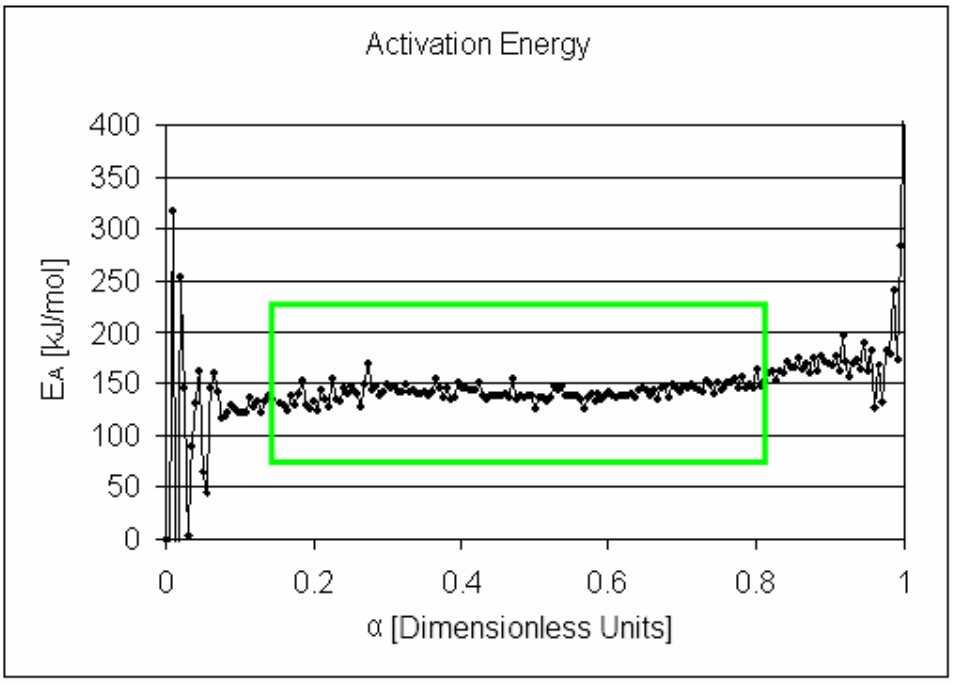


Figure 5-18: Galwey's method for RFL

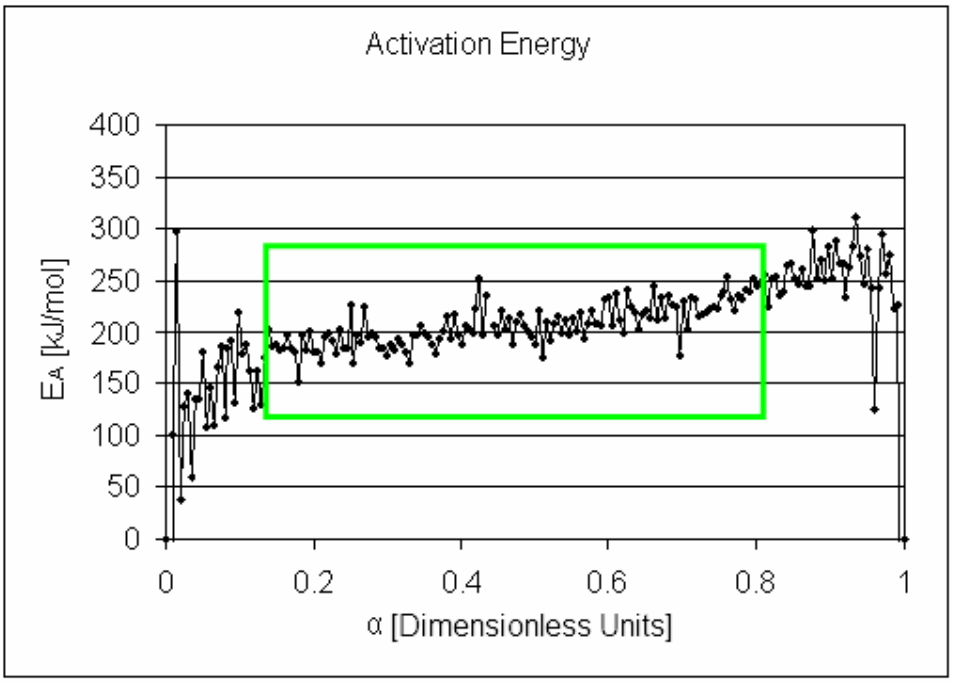


Figure 5-19: Galwey's method for PRFL

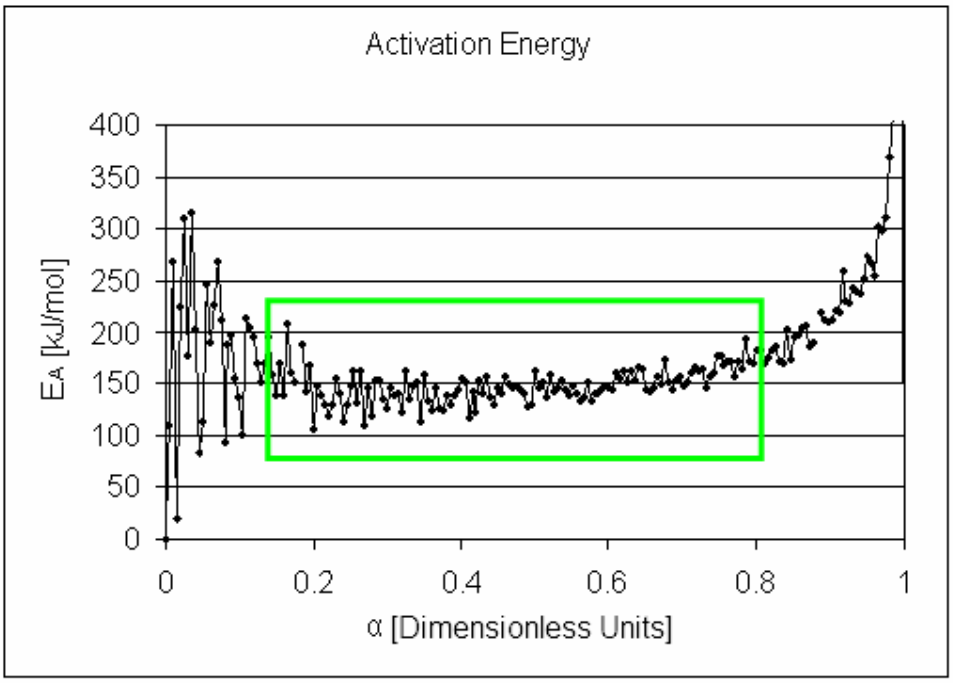


Figure 5-20: Galwey's method for CPRFL

As can be seen from the foregoing plots, none of the samples exhibits a constant activation energy. This would indicate that none of the samples have a true, single rate-controlling mechanism. In all cases the samples exhibited a large degree of uncertainty or drift during the final and initial stages of the oxidation. Such behaviour is not unexpected for a variety of reasons: the samples are not perfect disc shapes, and they contain surface irregularities and a distribution of particles. Thus during the initial stages of burn-off such irregularities will cause fluctuations in the reaction rate and small particles will tend to oxidise faster. Presumably however, at some point fairly regular structures are achieved and the inherent macrogeometry of the particle takes over, leading to regular oxidation with a clear activation energy.

At high conversions, on the other hand, secondary impurity effects might start playing larger and larger roles as the particles shrink. This may include catalyst agglomeration and inhibitor accumulation. These effects, coupled with geometric considerations, e.g. pit and channel coalescence, would result in sporadic fluctuations in the reaction rate which would contribute to the uncertainty in estimating the activation energy during these periods. Nonetheless, most samples have a fairly large region of stable activation energy, as indicated by the low standard deviation. The calculated activation energies are shown in Table 5-4, together with the relevant statistics.

Table 5-4: Results for Galwey's method for the determination of activation energy

| Sample | Conversion range used (%) | Calculated activation energy (kJ/mol) | Std Dev. (kJ/mol) | % Std Dev. |
|---|---|---|---|---|
| NNG | 15-80 | 175.8 | 25.1 | 14.3 |
| NSG | 15-80 | 170.0 | 13.5 | 8.0 |
| ZNG | 15-80 | 199.4 | 9.7 | 4.9 |
| KISH | 15-80 | 246.9 | 18.8 | 7.6 |
| FSG | 15-80 | 166.8 | 11.1 | 6.6 |
| RFL | 15-80 | 151.6 | 7.3 | 4.8 |
| PRFL | 15-80 | 206.7 | 20.0 | 9.7 |
| CPRFL | 15-80 | 154.2 | 16.5 | 10.7 |

The modelling in a previous section indicated that for the oxidation reaction under consideration, the conversion functions should all start at one if the initial active surface area is used to normalise the observed reaction rate data. Combining Eqs (5.22) and (5.24) yields:

$$\frac{d\alpha}{dt} = \frac{k_{ASA}(T)}{m_0} ASA_0 f^0(\alpha) \quad (5.32)$$

which may be rewritten as:

$$\frac{d\alpha/dt}{k_{ASA}(T)} \left[ \frac{ASA_0}{m_0} \right]^{-1} = \frac{d\alpha/dt}{k_{ASA}(T)} \frac{1}{\chi_0} = f^0(\alpha) \quad (5.33)$$

Thus using the value from literature for the pre-exponential factor given in Table 5-1 and the activation energy previously determined for each sample, a plot of the left-hand side of Eq. (5.33) may be constructed. A suitable value for the initial specific active surface area ($\chi_0$) of the sample may then be chosen such that the observed conversion function lies between zero and one. The result of this operation, i.e. the scaled conversion functions, for the non-isothermal experiments conducted on the samples used to estimate the activation energy are shown in Figure 5-21 to Figure 5-28. The estimated initial specific active surface areas are given in Table 5-5.

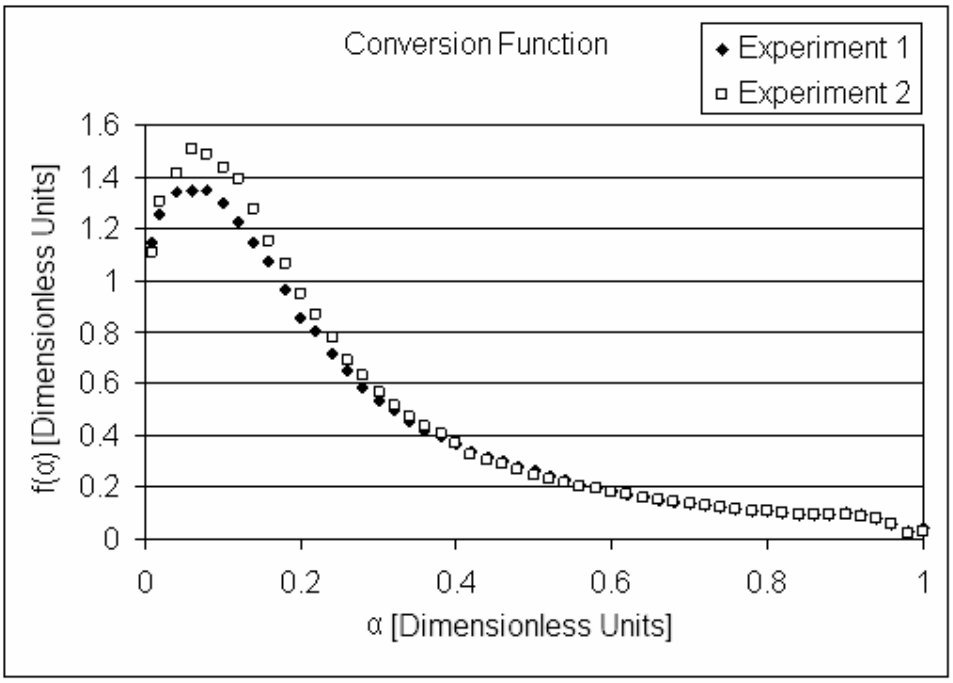


Figure 5-21: Conversion function for NNG

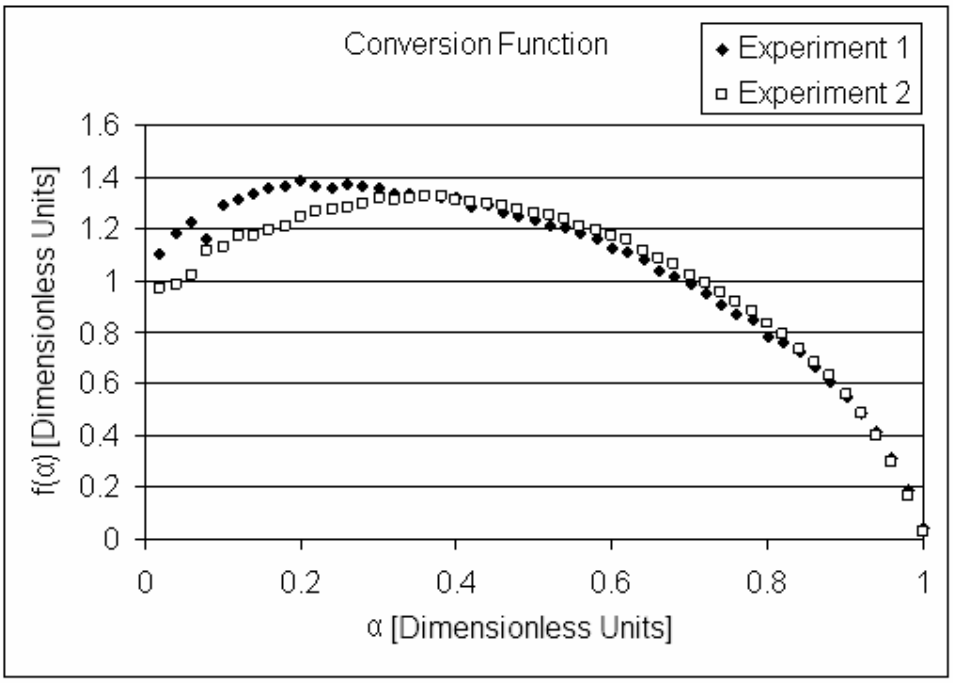


Figure 5-22: Conversion function for NSG

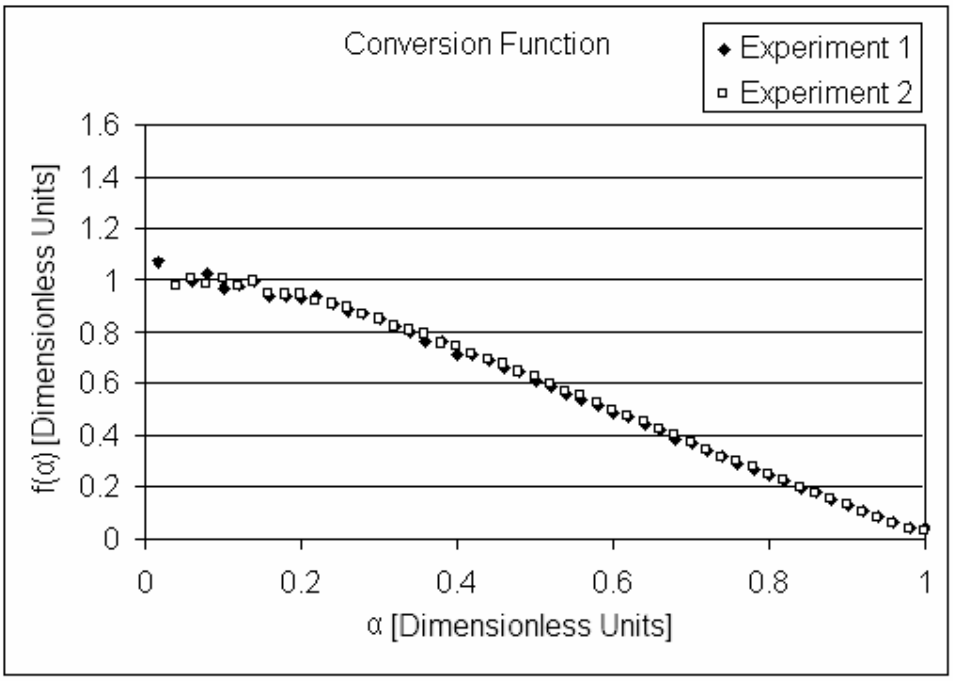


Figure 5-23: Conversion function for ZNG

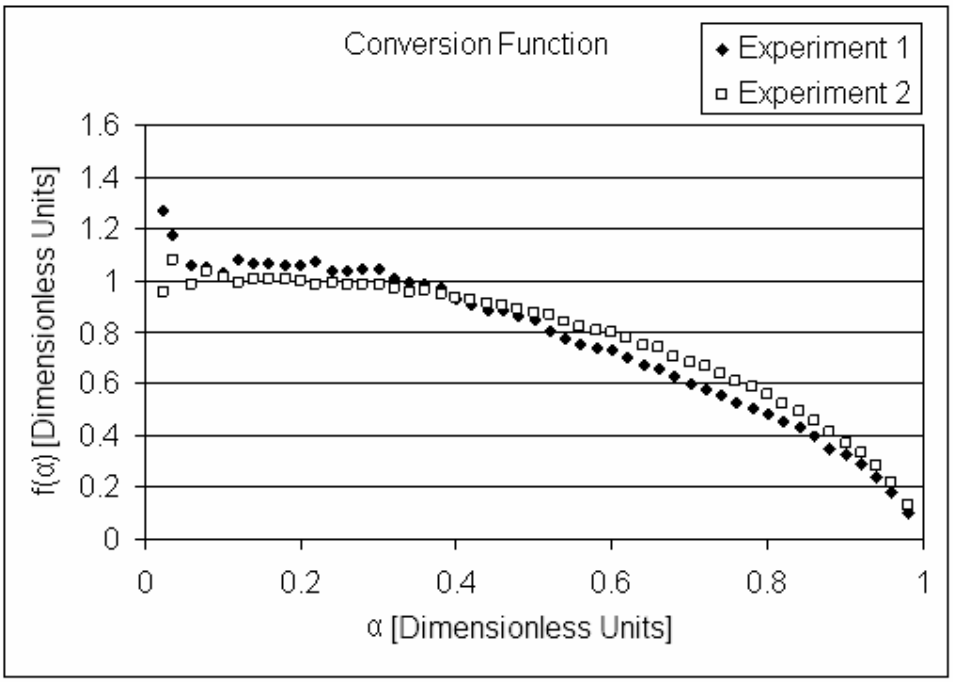


Figure 5-24: Conversion function for KISH

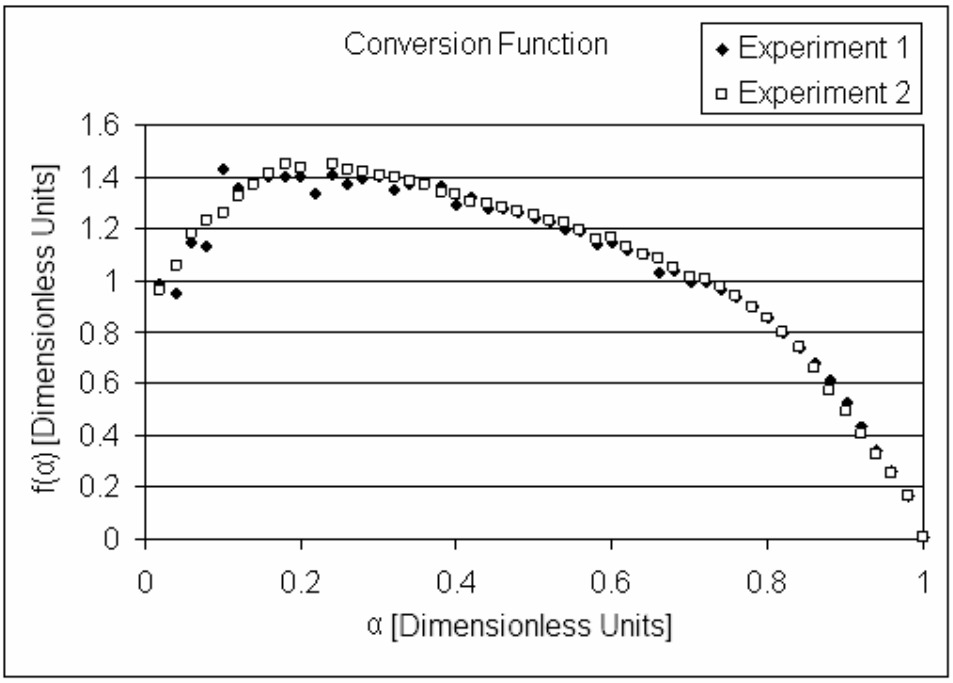


Figure 5-25: Conversion function for FSG

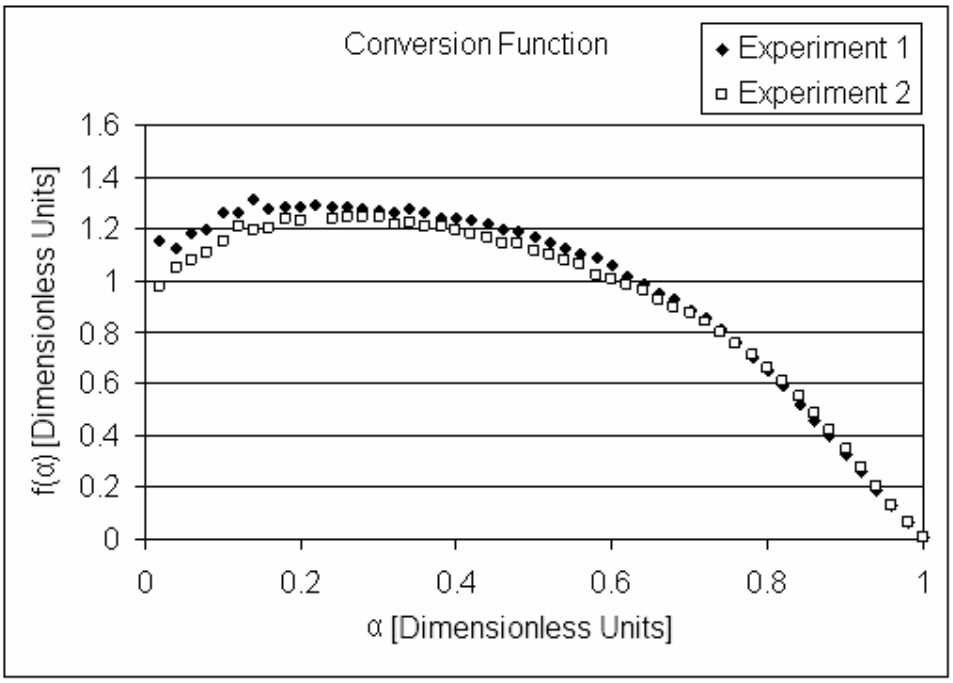


Figure 5-26: Conversion function for RFL

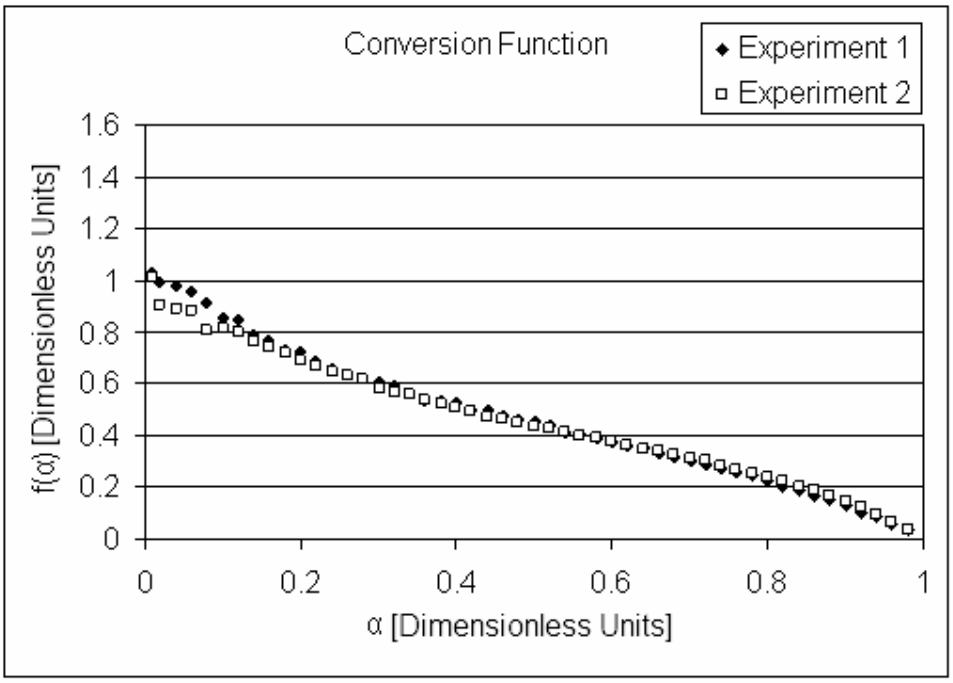


Figure 5-27: Conversion function for PRFL

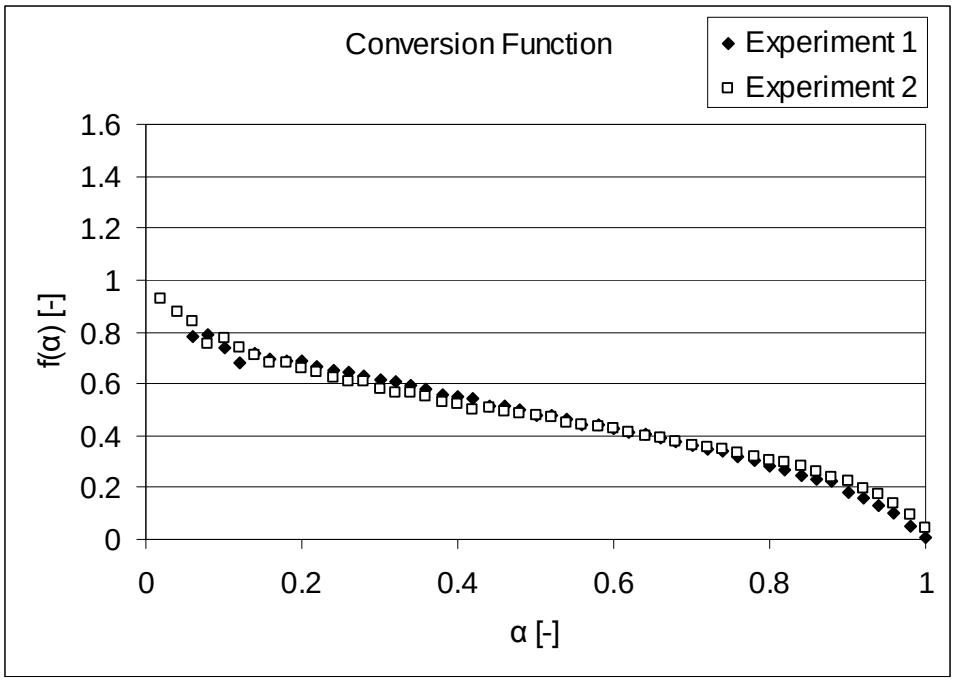


Figure 5-28: Conversion function for CPRFL

Table 5-5: Estimated initial specific active surface area

| Sample | $X_0$ Specific $ASA_0$ ($m^2/g$) | Calculated activation energy (kJ/mol) |
|---|---|---|
| NNG | 1.457 | 175.8 |
| NSG | 0.070 | 170.0 |
| ZNG | 2.083 | 199.4 |
| KISH | 55.483 | 246.9 |
| FSG | 0.125 | 166.8 |
| RFL | 0.008 | 151.6 |
| PRFL | 2.633 | 206.7 |
| CPRFL | 0.008 | 154.2 |

The observed behaviours are similar, but subtly different. Broadly, the conversion functions can be placed into two categories, i.e. decreasing over the whole range of conversion, or initially increasing then decreasing. The most complex behaviour is exhibited by the NNG sample. This sample undergoes an initial acceleration in the reaction rate, followed by a rapid deceleration and finally a slow decay. These behaviours will be evaluated on the basis of more complex flake geometries than the simple disc, which will be developed in the next section.

The calculated initial active surface areas are remarkably close to expected values for some of the samples. This is fairly unexpected given the uncertainty in these estimates:

- The values were calculated using a pre-exponential factor ($k_{ASA}$) taken from the literature, based on pit growth studies on HOPG [202].
- The active surface area of graphite is extremely small.
- The activation energy calculation shows significant amounts of uncertainty in the initial burn-off region relevant to this value.
- The assumption is made that the sole factor governing initial reactivity is active surface area.
- These samples contain catalytic and other impurities which affect activation in an, as yet, unknown fashion.

In addition, it appears that these results are affected by the kinetic compensation effect. A clear trend is visible in Figure 5-29, showing an increase in the estimate of the initial active surface area with an increase in the separately determined activation energy. This effect is of special concern for the RFL samples which clearly show this dependence moving from the as-received to the purified and back to the contaminated samples. In general, the initial ASA of these samples is not expected to change at all due to these treatments.

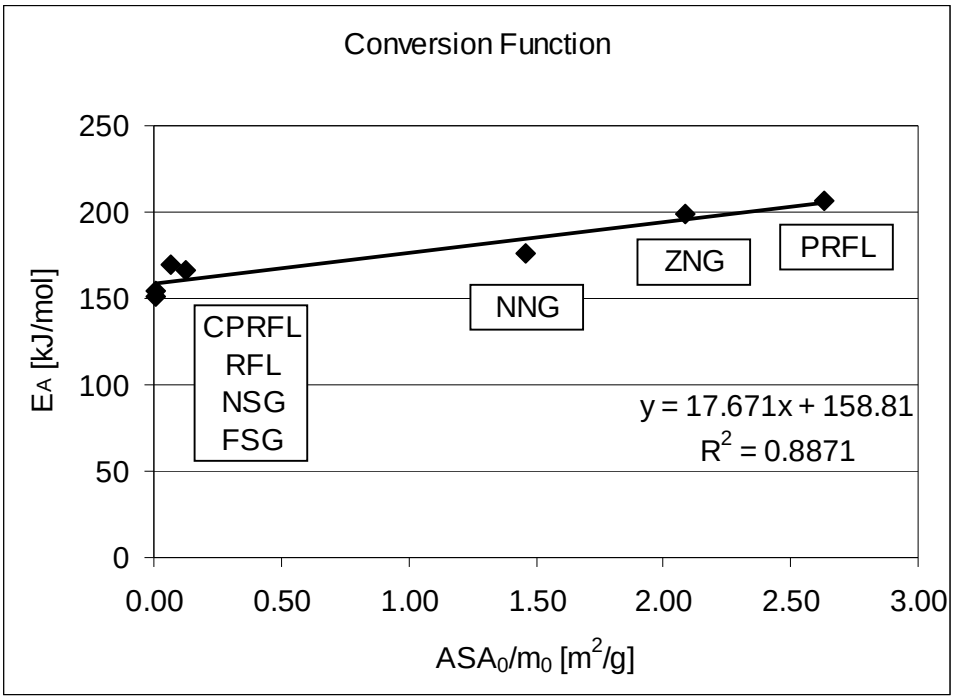


Figure 5-29: Kinetic compensation effect across all samples

Despite these facts, most of the active surface area values are reasonable. This would indicate that it may indeed be possible to unite several, somewhat disparate, oxidation behaviours from different samples under one coherent reaction scheme. To ensure that consistent results were being obtained, the RFL samples were also analysed isothermally to validate the observed conversion functions. If the isothermal conversion function agreed with the non-isothermal behaviour, it would indicate excellent consistency with the determined kinetic parameters.

This is critically important for two reasons. Firstly, the conversion function is the basis for understanding the mechanism (e.g. ASA development) that

governs the observed oxidation behaviour. Secondly, the shape of the conversion function is highly dependent on the estimated kinetic parameters for non-isothermal experiments. However, this is not the case for isothermal experiments. During an isothermal experiment a plot of the dimensionless reaction rate should provide the conversion function, simply scaled by the relevant kinetic parameters, thus validating the conversion function obtained and increasing confidence in the underlying mechanism based on this function.

The as-received RFL sample was analysed over a 200 ºC temperature range at 50 ºC intervals. The kinetic parameters in Table 5-6 were found, based on Eq. (5.33), to unite the observed behaviours, as shown in Figure 5-30.

Table 5-6: Isothermal kinetic parameters

| | | |
|---|---|---|
| $k_{ASA}$ | $2.403 \times 10^6$ | $g/m^2/s$ |
| $E_A$ | 156.7 | kJ/mol |
| $X_0$ | 0.019 | $m^2/g$ |

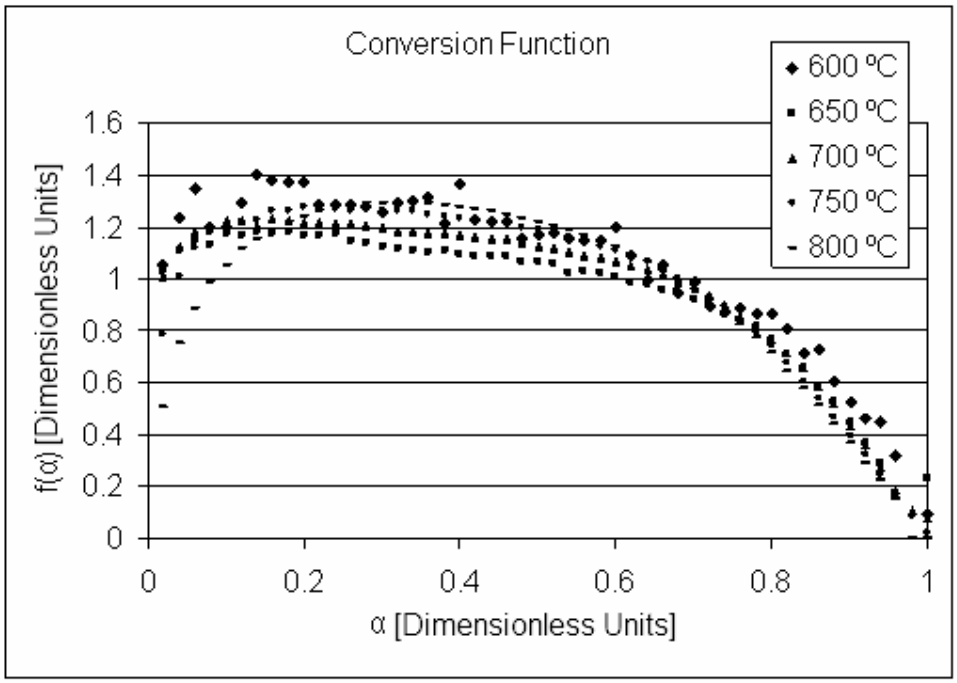


Figure 5-30: Isothermal conversion function for RFL

The estimated activation energy and estimated initial active surface area are in excellent agreement with the kinetic parameters obtained from the

non-isothermal studies. However, if the initial region of the curve is evaluated more closely as in Figure 5-31, a systematic error is noticeable. Due to the low reaction rate, the experiment at 600 ºC shows significant noise and was omitted from this figure.

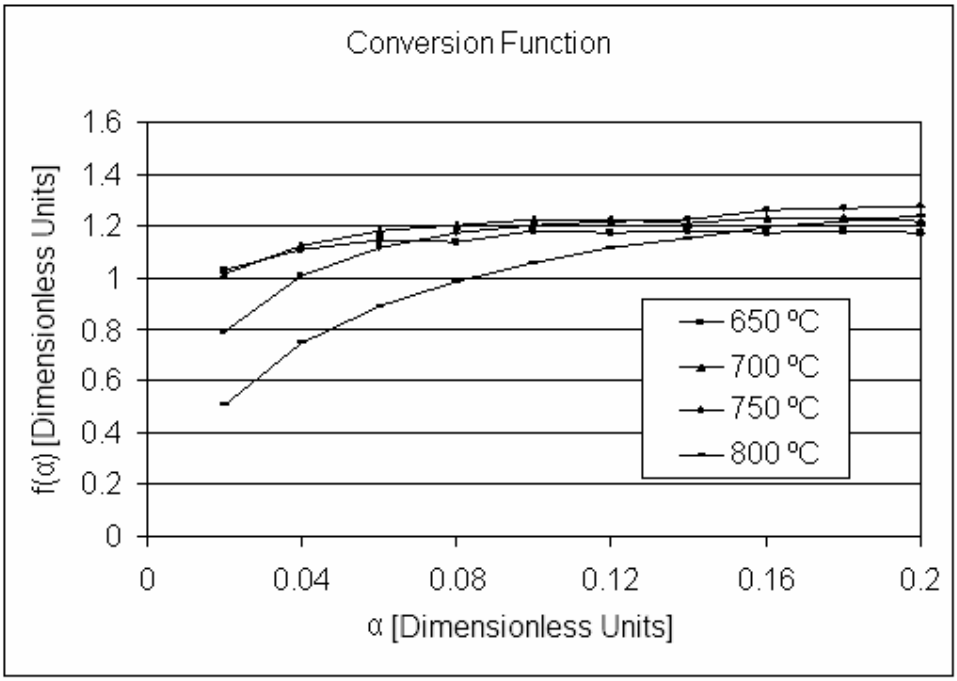


Figure 5-31: Systematic error in RFL conversion function

As can be seen from Figure 5-31, the initial conversion function is progressively lower at higher temperatures. This is caused by a lower than expected measured reaction rate. In all cases, however, the rate returns to the expected trajectory. This effect is caused by the gas change from inert to oxidising. At higher temperatures the reaction rate is higher, thus the effect persists to higher conversions (but the same elapsed time). As mentioned in Section 3, the time constant for a gas change was experimentally determined as $\tau' \sim 2.6$ min. Furthermore, a simple *n*-th order approximation for the gas-phase reaction dependence or accommodation function is chosen with $n \sim 0.4$. Using these values, the samples can be compensated for this effect and the result is shown in Figure 5-32.

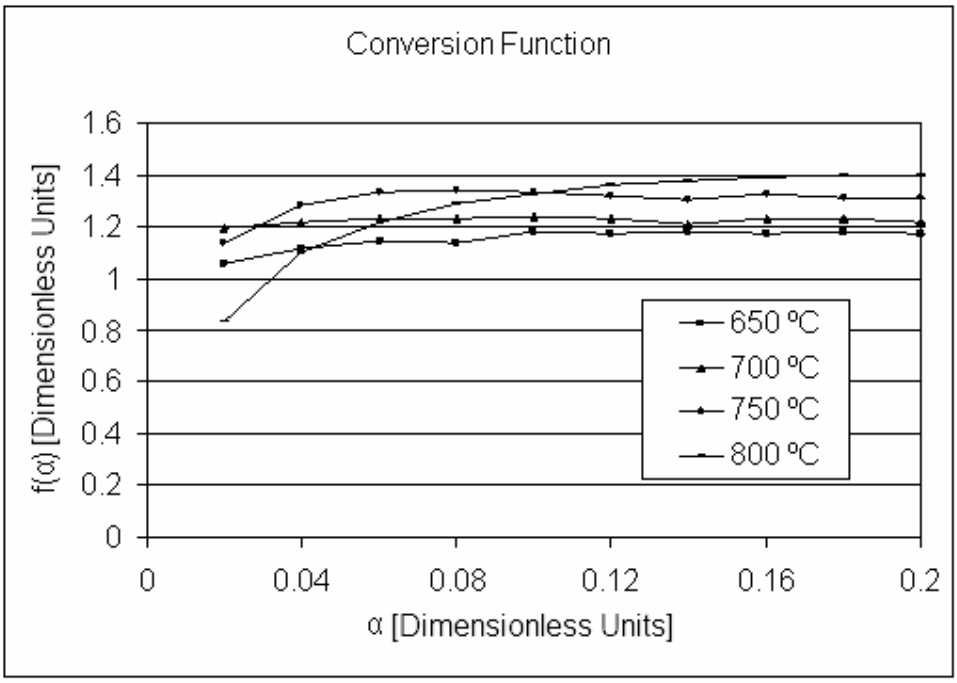


Figure 5-32: Compensated RFL conversion function

The effect is not completely eliminated, but it is reduced. This would indicate that the *n*-th order approximation is probably not adequate. However, for the purposes of this comparison the improvement is adequate. The average value of all the compensated, isothermal conversion functions is now compared with the average value of the non-isothermal conversion functions. As can be seen from Figure 5-33, the agreement is excellent.

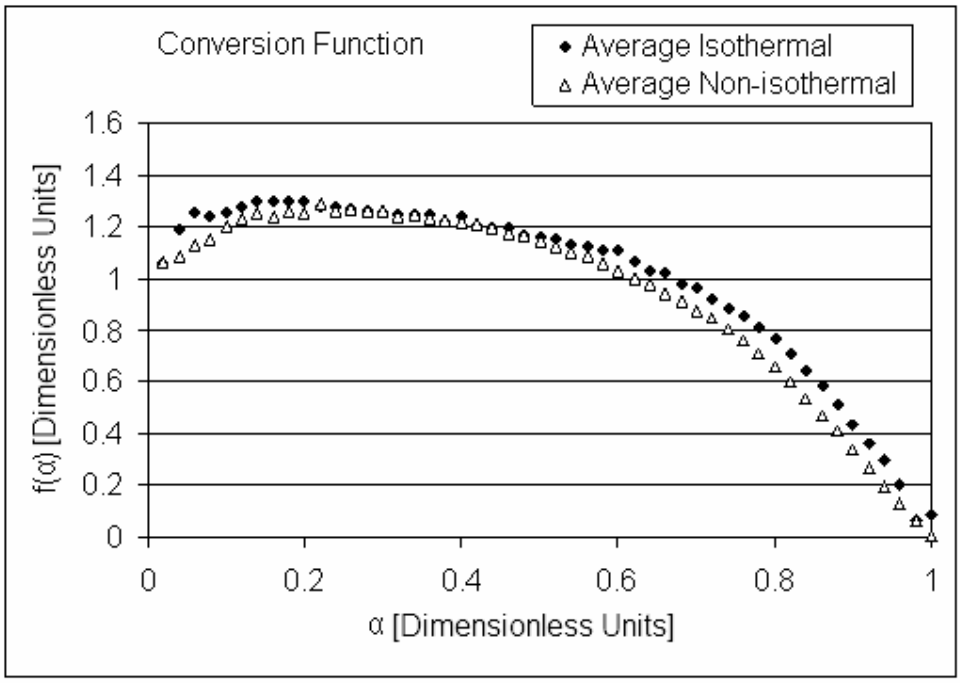


Figure 5-33: RFL conversion function comparison

This provides considerable confidence that the conversion function is consistent across a wide temperature range and that the kinetic parameters are correct. A similar analysis was done for the purified, PRFL, and contaminated, CPRFL, graphite samples. In these cases the same activation energy was used for both datasets and the calculated initial active surface areas were found to be $\chi_0$ = 4.39 and 0.0098 $m^2/g$ respectively for the purified and contaminated samples. These values agree well with the non-isothermal data. The results are shown in Figure 5-34 and Figure 5-35 for compensated isothermal data.

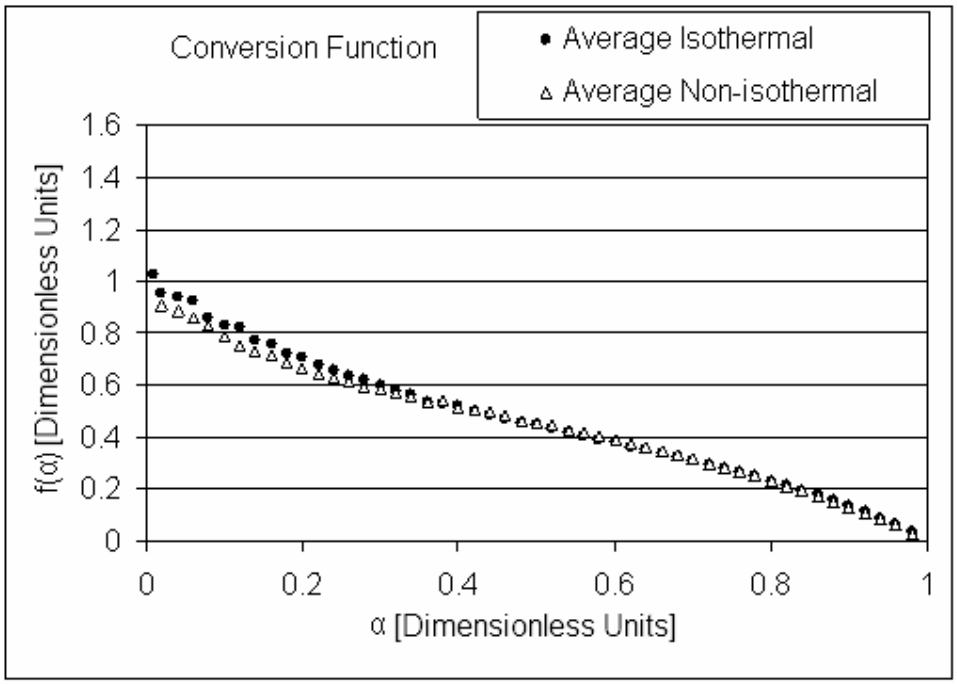


Figure 5-34: PRFL conversion function comparison

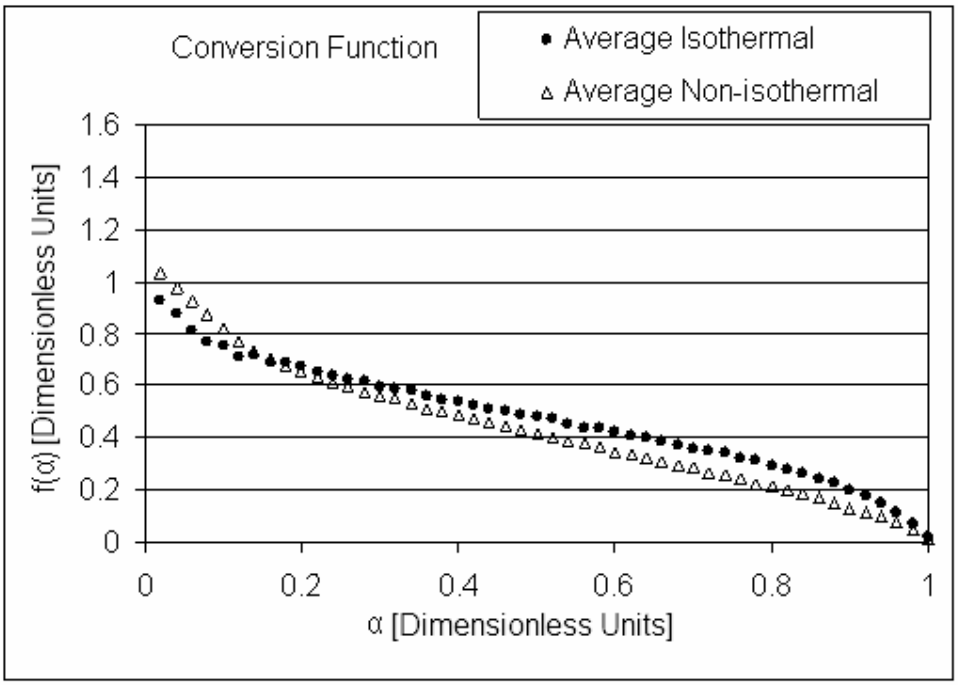


Figure 5-35: CPRFL conversion function comparison

Both figures demonstrate excellent consistency between the isothermal and non-isothermal data. If a mechanism can be found that will account for these

observed conversion behaviours, based on physical observations, it could be considered plausible with a high degree of confidence.

## 5.5 Active surface area development in complex shapes

In the previous sections only concave shapes were considered. Of particular interest, however, are convex shapes. A concave polygon is shown in Figure 5-36 (A); it will always have internal angles of less than 180º. On the other hand, a convex polygon will always have at least one internal angle greater than 180º, as shown in Figure 5-36 (B). An extreme case is the star shape which has several internal angles, e.g. Figure 5-36 (C).

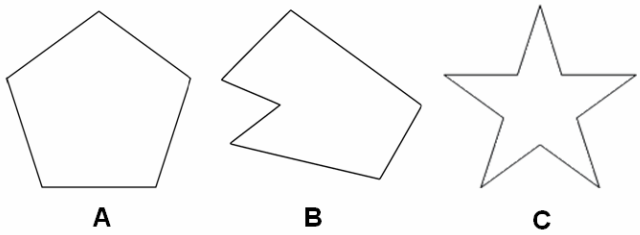


Figure 5-36: Convex shapes

Modelling these shapes analytically represents an especially tricky problem. The problem arises at the pinnacle of the internal angle that is greater than 180º. At this point a new surface is continually being created. The underlying assumption in previous discussions, i.e. Eq. (5.4), is that an edge continually recedes at a constant rate, at an angle exactly perpendicular to its surface. However, this assumption imparts no information regarding the formation of new surfaces. To understand the creation of a new surface, it is necessary to reduce the scale to the atomic level. Consider the atomic arrangement shown in Figure 5-37.

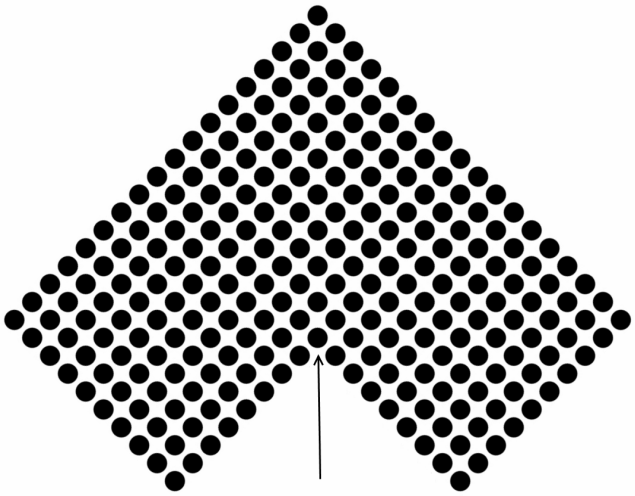

Figure 5-37: Atomic configuration at convex angle

The atom at the pinnacle, indicated by the arrow, will experience steric hindrance from the adjacent atoms and thus has a lower probability to react. For argument's sake, the assumption is made that all the adjacent edge atoms are removed, except the one at the pinnacle, resulting in the structure shown in Figure 5-38.

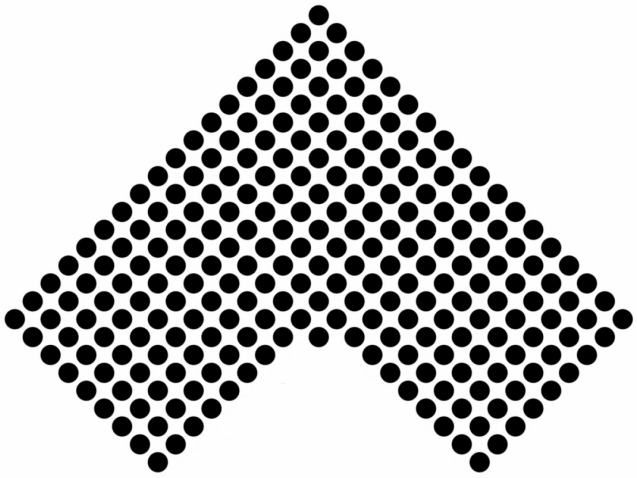

Figure 5-38: Atomic configuration at convex angle after one reaction step

A new infinitesimal flat surface has been created, one atom wide. The atom under consideration previously now has two adjacent neighbours, although they are further away than other neighbours by a factor of sin(45º) = 1.414.

Assuming this atom and all the other edge atoms react, the substructure shown in Figure 5-39 results.

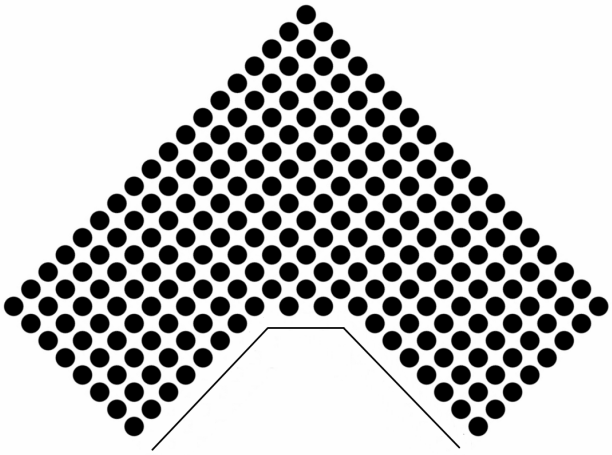

Figure 5-39: Atomic configuration at convex angle after two reaction steps

As can be seen from the straight lines, a very small, new, flat face has been created with two new convex angles greater than 180º. In accordance with the assumption underlying Eq. (5.4), this new face will continue to recede at a constant velocity, perpendicular to the surface. This idealised progression may be approximated as shown in Figure 5-40.

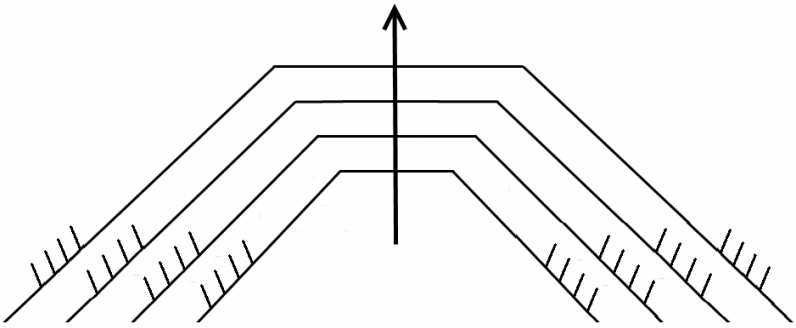

Figure 5-40: Idealised surface progression for convex pinnacle

However, such a progression is incorrect. The previous analysis must be applied incrementally at each of the new convex angles that are created. Thus the true edge creation will follow a fractal-type surface creation, leading to the formation of a pseudo-circular edge, consisting of countless angles, as shown in Figure 5-41.

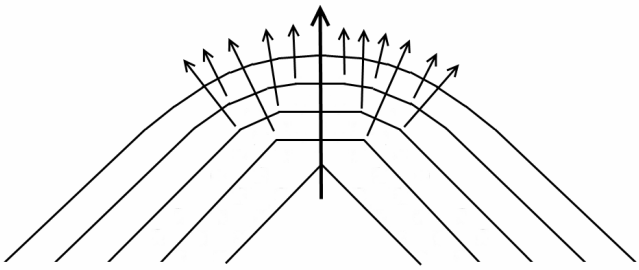

Figure 5-41: Fractal surface progression for convex pinnacle

It is interesting to note, however, that at some point the angles at the edge in the direction of the original concave angle, i.e. perpendicular to the large arrow, will become infinitesimally small. At this point the edge will no longer subdivide and will act as a completely flat surface. Again, this flat surface has to conform to the underlying modelling assumption and recede at a constant rate. This surface will therefore flatten out and the convex corner will tend to move laterally, as illustrated in Figure 5-42.

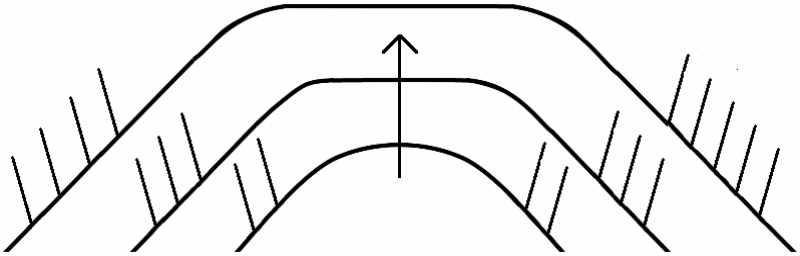

Figure 5-42: Expected surface progression for convex pinnacle

Deriving an analytical expression to simulate this effect would be very complex. Another noteworthy structure to consider is the reverse of the construction just considered. This may be thought of as a surface irregularity on one edge of an infinite plate, depicted schematically in Figure 5-43.

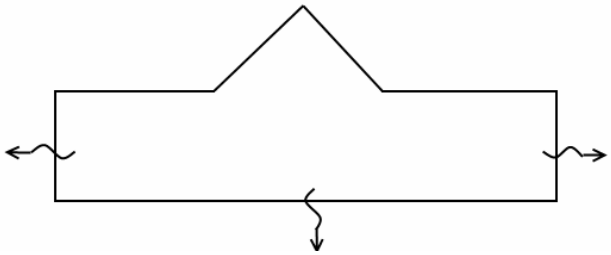

Figure 5-43: Surface irregularity on an infinite plate

It is fairly easy to visualise that at the pinnacle of the irregularity, the reaction is occurring from two angles simultaneously. Thus relative to the flat edge the irregularity will recede and eventually disappear, as shown in Figure 5-44.

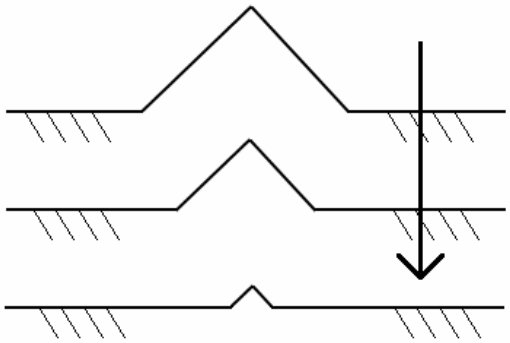

Figure 5-44: Fate of surface irregularity on an infinite sheet

However, in the light of the previous discussion, a more accurate representation would be that the concave edges achieve a more rounded appearance as the reaction proceeds since these are convex angles similar to the one just considered. Nevertheless, the key point is that the surface irregularity will recede and eventually disappear. Thus it is tempting to assume that shapes with surface irregularities will necessarily flatten out these edges and achieve a rounded geometry. For example, consider the two constructions shown in Figure 5-45.

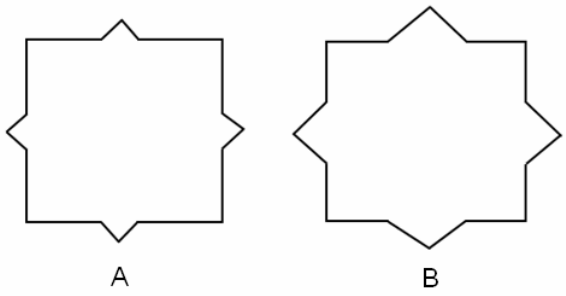


Figure 5-45: Surface irregularities on a particle

In the first case, Figure 5-45 (A), it seems that the surface irregularities are small enough relative to the flat edges of the square for them to recede and disappear without influencing the overall particle geometry. Thus given the fact that all the edges recede at a constant rate, the construction will retain its square shape throughout the reaction. However, for the second construction shown in Figure 5-45 (B), the situation is quite different. It is no longer clear whether the irregularities will recede such that the structure will retain its square shape or whether they will become round and the structure will eventually become a circle. Here a complex interplay between all the effects just discussed is occurring. The exact relationship between the initial convex angle and the rounding achieved in the remaining convex corners, as shown in Figure 5-42, must be known. Without this it is not possible to determine the point at which the edges align to achieve a circular progression or not.

It may be possible to derive the analytical expressions for such regular shapes, such as the star of Figure 5-36 (C), or even more complex shapes which are an arbitrary mixture of convex and concave angles. However, such a task would be extremely arduous for all the shapes possible in flake graphite. Furthermore, certain geometries would be impossible to solve analytically, e.g. combinations of randomly curved shapes. Such structures are especially important during catalysed oxidation and they are frequently formed when catalyst particles exhibit channelling behaviour. For example, see the erratic channels traced in the graphite basal plane as shown in Figure 5-46 and Figure 5-47.

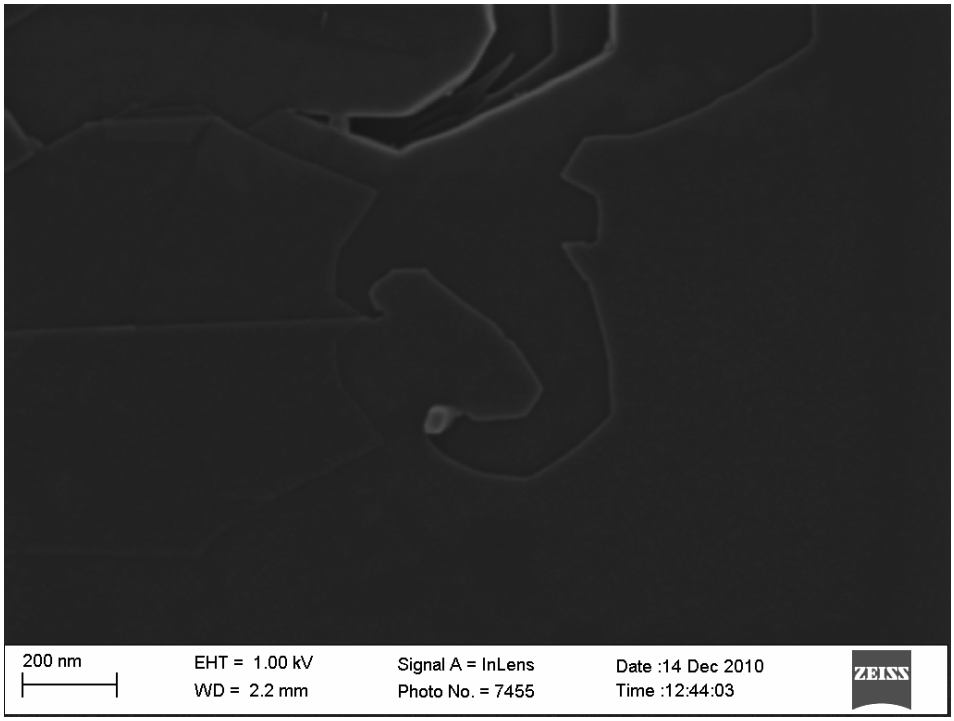


Figure 5-46: Erratic channel formed by catalytic particle

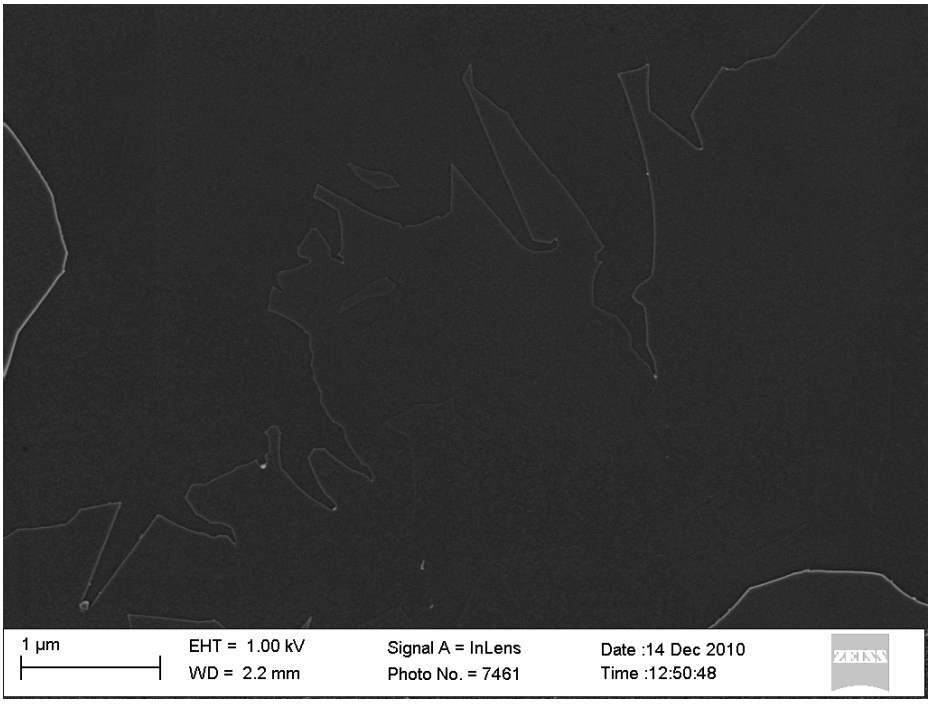


Figure 5-47: Erratic edge formed by channelling catalyst particles at a basal step on graphite

Thus a new approach is needed to simulate quickly and easily the surface area development of all of the geometries just discussed.

## 5.6 Probability-based ASA modelling

The atomistic considerations in the previous section provide a starting point for modelling complex ASA development. A probability-based, Monte Carlo-type simulation was developed using the finite element approach as follows. Consider the infinitesimal edge cube used previously, but in this case as part of an infinite flat sheet of thickness, *d*, shown in Figure 5-48.

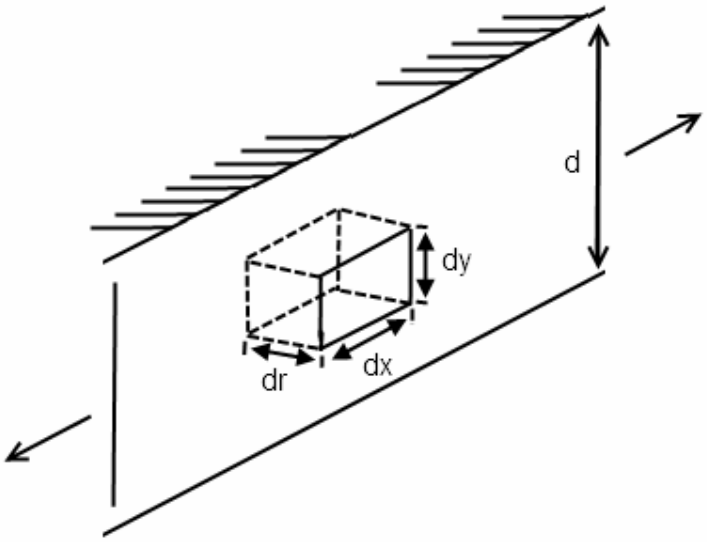


Figure 5-48: Infinitesimal cube at the edge of a flat sheet

The reaction rate Eq. (5.22) may be rewritten as:

$$\frac{d\alpha}{dt} = \frac{-1}{m_0}\frac{dm}{dt} = \frac{ASA\, k_{ASA}(T)}{m_0} \quad (5.\ 34)$$

Consider a small incremental time step ($\Delta t$). The change in mass for the entire object during this step may be approximated as:

$$dm \approx \Delta t \frac{dm}{dt} = -\Delta t\ ASA\, k_{ASA}(T) \quad (5.\ 35)$$

This is assuming that the ASA change during the time step is negligible, that is to say the time step is very small. The change in mass may be reformulated in terms of the probability that a single cube reacted during that time step as follows. Since the cube is lost, the change in mass is negative. Thus:

$$dm = -P_{cube}\ n_{edge}\ m_{cube} \quad (5.\ 36)$$

where $P_{cube}$ is the probability that a single cube reacts during the given time step, and $n_{edge}$ is the number of cubes exposed at the edge of the plate since only these are available to react. The mass ($m_{cube}$) and ASA ($ASA_{cube}$) of the cube are:

$$m_{cube} = dr\ dx\ dy\ \rho_C \quad (5.\ 37)$$

$$ASA_{cube} = dx\ dy \quad (5.\ 38)$$

but the number of edge cubes may be calculated by:

$$n_{edge} = \frac{ASA}{ASA_{cube}} \quad (5.\ 39)$$

Equating expressions (5.35) and (5.36) and substituting the relevant values, one finds:

$$P_{cube} = k_{ASA}(T)\frac{\Delta t}{dr\ \rho_C} \quad (5.\ 40)$$

The density of the graphite crystal ($\rho_C$) is constant for a given simulation. Thus the reaction probability for a single cube is dependent only on its depth, *dr*, and the chosen simulation time step, *Δt*. The probability must always be less than or equal to one. This places a restriction on the combination of depth and time-step values that are possible, as given by:

$$\frac{\Delta t}{dr} \leq \frac{\rho_C}{m_0\ k_{ASA}(T)} \quad (5.\ 41)$$

The situation is slightly more complex for cubes that are exposed at more than one surface, e.g. the corner cube shown in Figure 5-49.

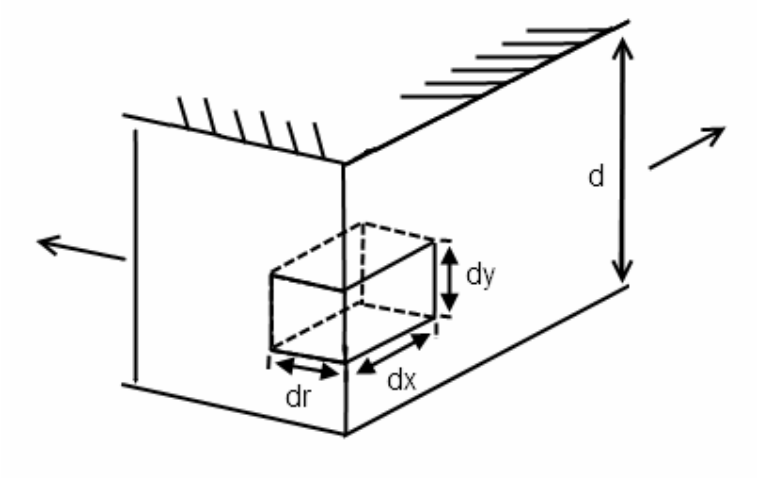


Figure 5-49: Infinitesimal corner cube at the edge of a flat sheet

In this case it is easier to set all sides of the cube equal. The probability that this cube was not reacted in a certain time step may be most conveniently stated as the probability that the cube was not removed via reaction from face 1, nor was it removed from face 2. This is represented by the expression:

$$P_{not\ react}^{2\,sided} = P_{not\ react}^{Face\,1} \bigcap P_{not\ react}^{Face\,2} \quad (5.\ 42)$$

This expression removes the need to consider possible union combinations. Furthermore, it is readily generalised into the three- or four-dimensional case where more sides are exposed, as follows:

$$P_{not\ react}^{4\,sided} = P_{not\ react}^{Face\,1} \bigcap P_{not\ react}^{Face\,2} \bigcap P_{not\ react}^{Face\,3} \bigcap P_{not\ react}^{Face\,4} \quad (5.\ 43)$$

since the probability that a cube did not react from a single face is:

$$P_{not\ react}^{1\,sided} = 1 - P_{cube} \quad (5.\ 44)$$

Hence the probability of reaction within a given time step for a cube exposed at one, two, three or four surfaces respectively, is summarised as:

$$P_{cube}^{1\ sided} = P_{cube} \quad (5.45)$$

$$P_{cube}^{2\ sided} = 1 - \left(1 - P_{cube}\right)^2 \quad (5.46)$$

$$P_{cube}^{3\ sided} = 1 - \left(1 - P_{cube}\right)^3 \quad (5.47)$$

$$P_{cube}^{4\ sided} = 1 - \left(1 - P_{cube}\right)^4 \quad (5.48)$$

To simulate a specific geometry, consider the square finite element grid shown in Figure 5-50. The simplest case is to assume that the grid is only one cube thick and all remaining sides of the cube are equal, hence *dy* = *d*, *dx* = *dr*.

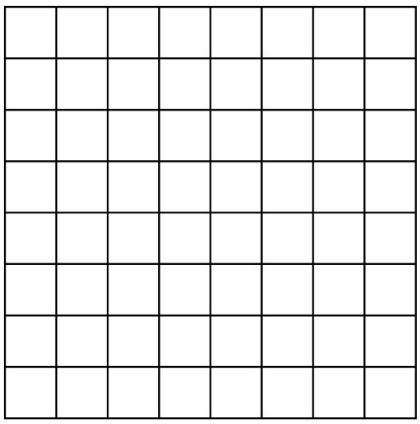

Figure 5-50: Finite element grid

For simplicity, only a single-layer simulation was considered. The simulation can easily be extended to include multiple layers. However, this simply amounts to summing over several single-layer simulations with varying characteristic dimensions, leading to an averaging effect. On this grid, virtually any shape can be approximated. For example, the ideal disc shape could be approximated as shown in Figure 5-51.

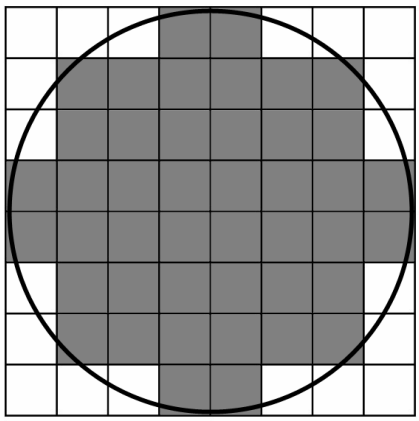

Figure 5-51: Finite element approximation of the ideal disc

By choosing a suitable grid size, the approximation can be improved. However, decreasing the size of the subelements enhances the approximation, but also increases the computational load and simulation time since more elements must be considered. As a starting point, the simulation parameters given in Table 5-7 were chosen:

Table 5-7: Simulation parameters

| | | |
|---|---|---|
| $k_{ASA}$ | $2.403 \times 10^6$ | $g/m^2/s$ |
| D | 200 | µm |
| dy = d | 20 | µm |
| dx = dr | 2 | µm |
| Δt | 5 | s |
| $E_A$ | 150 | kJ/mol |
| $T_0$ | 750 | ºC |
| β | 0 | ºC/min |

Based on the particle dimensions and the assumption that the flake is perfectly crystalline, the starting mass and active surface area can be calculated. Since the diameter is 200 µm and the subelement size is 2 µm, the number of subelements in the grid is 100. Using these parameters, the reaction probability of a single subelement, with one edge exposed, may be calculated as 0.587. For each subelement with one edge exposed, a random number generator is used to spawn a number between zero and one. If the number is less than the reaction

probability, the subelement is deemed to have reacted and is removed from the simulation before the next cycle.

This process is repeated for all subelements that have at least one edge exposed, using the appropriate reaction probability. After each cycle the number of elements remaining is calculated, which allows the conversion to be tracked. Furthermore, at the end of each cycle the active surface area is calculated from the total number of edges exposed at that point. Such a simulation was constructed in Matlab®. The result of this simulation compared with the analytical model for a disc, i.e. $ASA = ASA_0 * (1-\alpha)^{0.5}$, is shown in Figure 5-52.

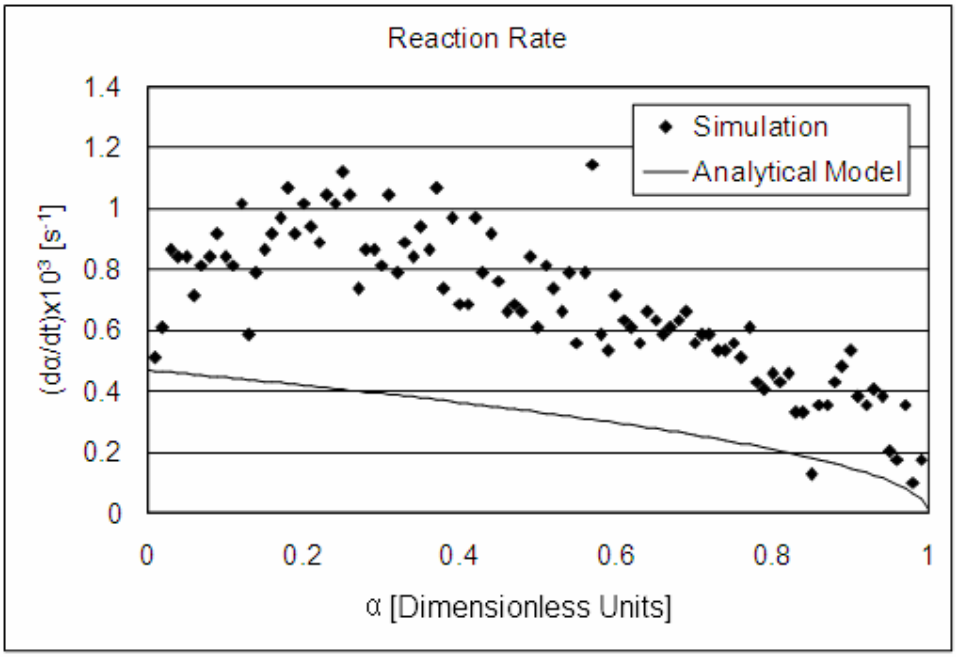


Figure 5-52: Simulation result for disc 100 x 100

As expected, due to the choice of a coarse grid size, the approximation is very rough and there is a significant amount of noise in the data. Figure 5-53 and Figure 5-54 show the simulation results for increasing the grid size to 500 x 500 and 1 000 x 1 000 subelements respectively.

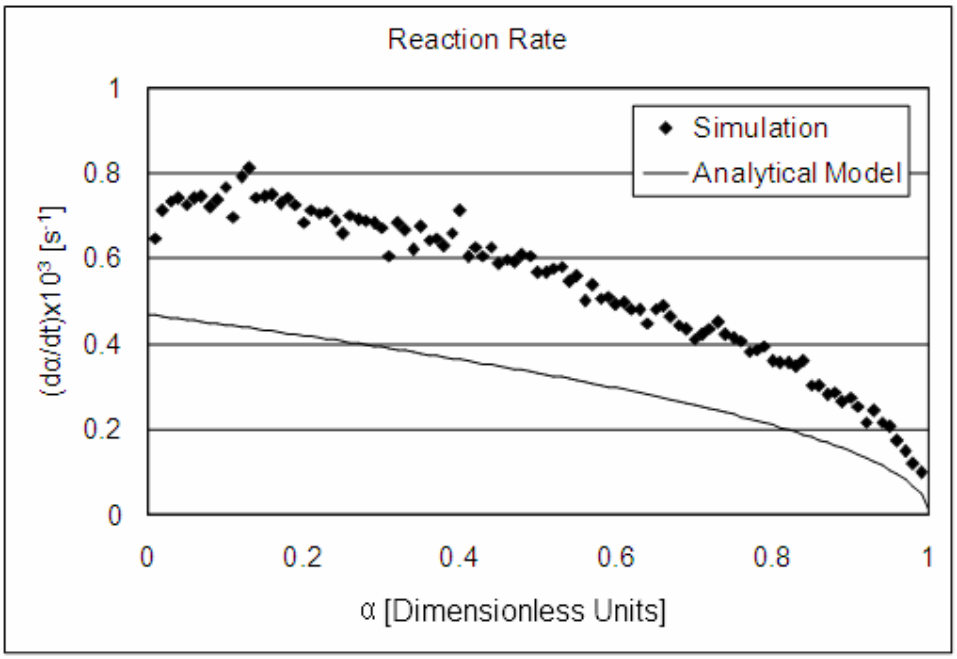


Figure 5-53: Simulation result for disc 500 x 500

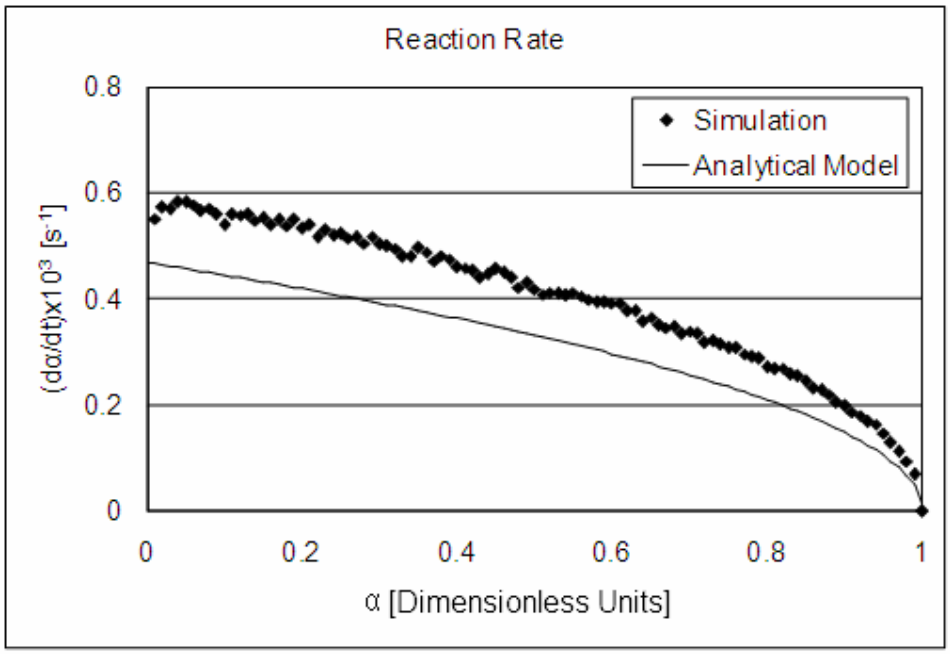


Figure 5-54: Simulation result for disc 1 000 x 1 000 – fine grid size

As can be seen from Figure 5-54, the simulation result is significantly improved for a finer grid size. However, two noteworthy aspects remain. Firstly, the simulated reaction rate is consistently higher than the analytically predicted rate and, secondly, the initial reaction rates are different. From a comparison of

the figures it is clear that as the grid size is increased, the simulated reaction rate approaches that of the analytically predicted rate more closely. All of these effects are related to the difference in active surface area between the simulated and analytical models. The grid approximation of the smooth analytical disc is very rough, as can be clearly seen from Figure 5-51. The active surface area of the simulation is initially higher than that of the analytical model, namely 16 000 $\mu m^2$ and 12 566 $\mu m^2$ respectively. As soon as the simulation proceeds, the ASA development is a complex interplay between the random removal of subelements, which induces surface roughening, and the increased reactivity of these subelements with multiple exposed edges, which tends to smooth the surface. Thus the surface roughness in the simulation increases from its initial value and eventually achieves a steady state. This effect is worse for a coarse grid size, leading to a higher steady state surface roughness and requiring a longer time to achieve this roughness, as can be seen from Figure 5-55.

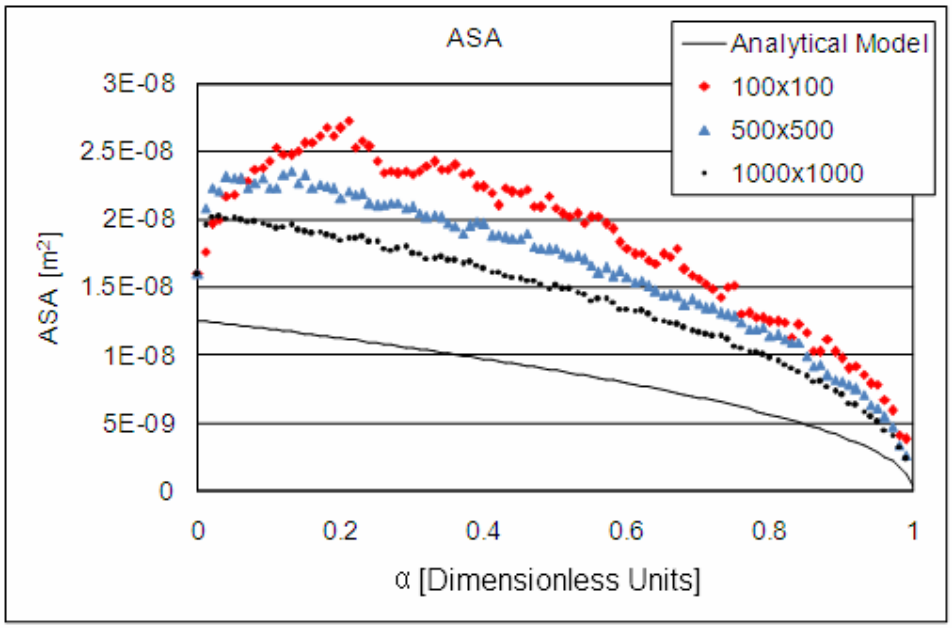


Figure 5-55: Simulation result for disc 1 000 x 1 000 – coarse grid size

This effect will also be dependent on the reactivity of a subelement. The ratio (*RR*) of the simulated ASA and the analytical ASA illustrates the achievement of steady state roughening, as shown in Figure 5-56. The average value is 1.69, which is significantly higher than the initial 1.27.

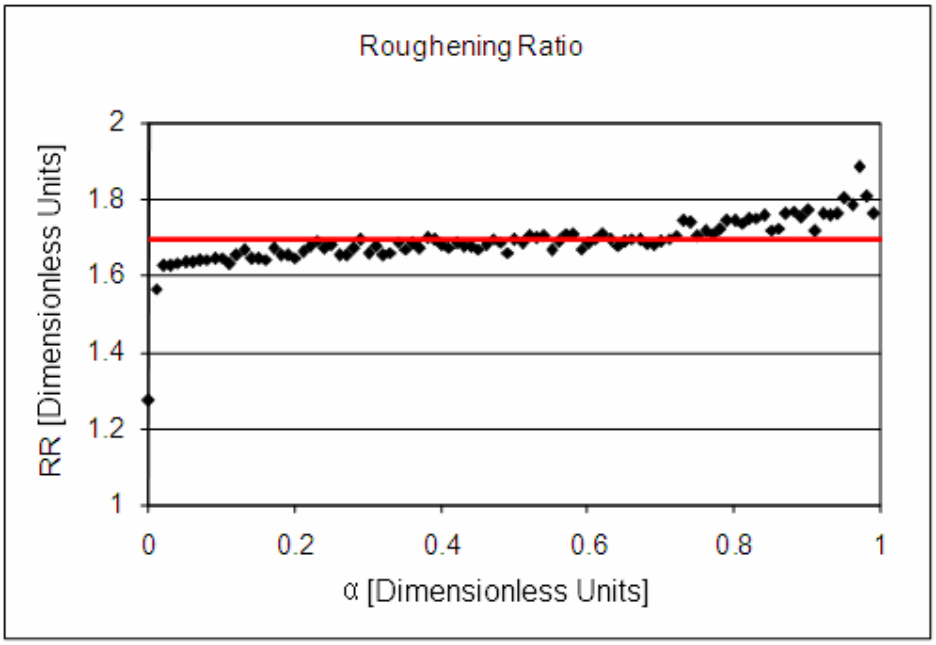


Figure 5-56: Surface roughening ratio for disc 1 000 x 1 000

A gradual increase in the roughening ratio, i.e. reaction rate discrepancy, is still visible. This is to be expected since the effect will become more pronounced as the size of the disc shrinks relative to the surface roughness. The surface roughness is a function only of the subelement size and hence is constant. This roughening effect must always be borne in mind when comparing the simulation results with analytical models and experimental data.

However, according to Eq. (5.26), if the ASA developments are governed by the same underlying geometric shape, the effect of a difference in ASA due to roughening on the reaction rate should be compensated for by simply dividing by the ratio. It should be noted, however, that the factor of 1.69 is a combination of two effects, namely the initial difference in surface areas and the subsequent development of a steady state surface roughness ratio. This may be expressed as:

$$ASA^{sim} = ASA^{\mathrm{mod}\,el}.ASA_0^{RR}.Rate_{Rxn} \quad (5.\ 49)$$

If the reaction rate for the simulation is divided by this factor, the reaction rate curves obtained are as shown in Figure 5-57.

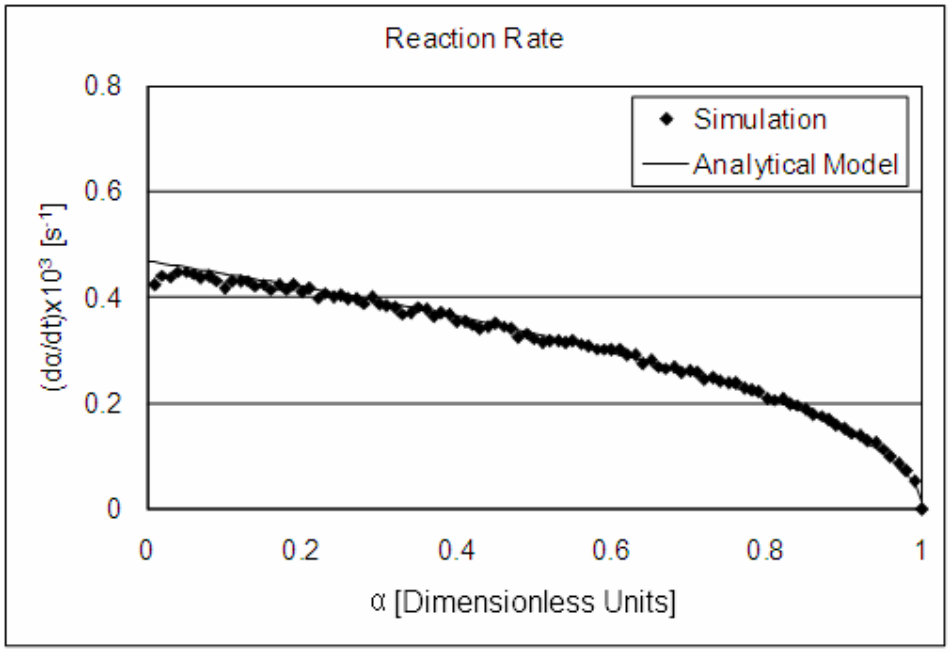


Figure 5-57: Compensated simulation reaction rate

Thus the reaction rate of simulation is initially slightly below the reaction rate predicted by the analytical model until such time that the surface roughening achieves steady state. This is not strictly speaking correct and the reaction rate should be compensated for differences only in the initial ASAs. However, this figure serves to illustrate the fact that if the surface roughening effect is simply compensated for by a constant factor, the simulation gives excellent agreement on the shape of the reaction rate curve generated by the analytical mode. Hence the probability-based finite element model provides a good approximation of the true conversion function model if the surface roughening effects (initial and progressive) are offset.

It is now possible to use the model to study the active surface area development of some of the complex surface structures discussed previously. In order to establish a baseline for the surface roughening effect, a flat surface is reacted from only one direction. This represents oxidation from a single face and should therefore proceed at a constant rate. The same parameters used for the disc simulation are used again, with a grid of 1 000 subdivisions. Based on Eq. (5.22), a plot of the reaction rate times the starting mass, divided by the initial ASA, should simply give the rate constant, assuming of course that the active

surface area remains constant throughout. The simulated reaction rate constant is shown in Figure 5-58.

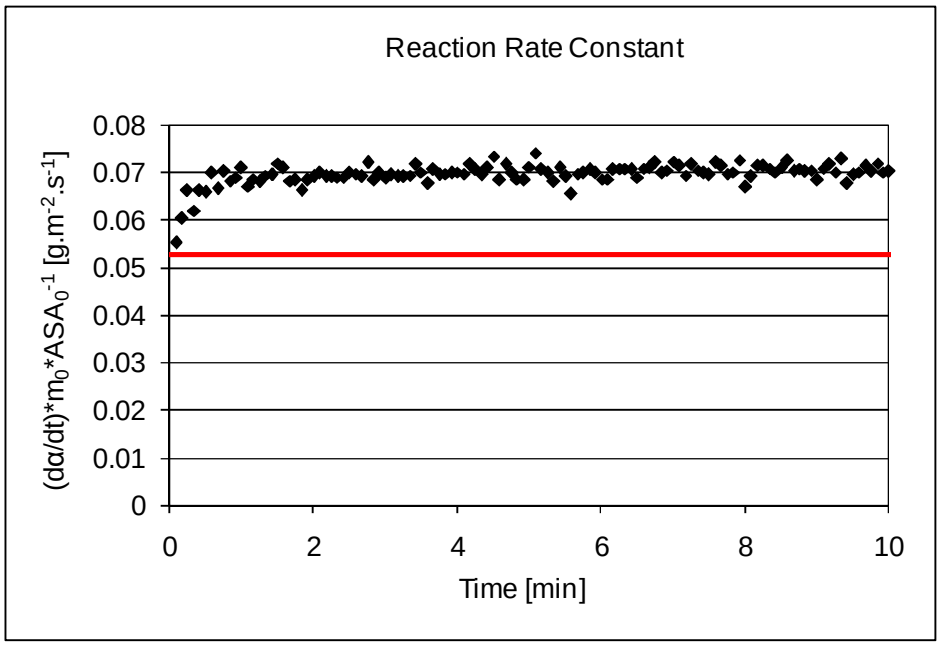


Figure 5-58: Reaction rate for a single flat face

From the values in Table 5-7 the true reaction rate constant is:

$$k_{ASA}(T) = k_{ASA} \exp\left(\frac{-E_A}{RT}\right) = 0.0528 \quad (5.\ 50)$$

As can be seen from Figure 5-58, the choice of such a fine grid and the reasonable reactivity allows the surface to rapidly achieve steady state roughening and a constant reaction rate. The reaction rate achieved is roughly 1.32 * 0.0528, which is consistent with the previously achieved roughening ratio since 1.69/1.27 = 1.33. This confirms the previous assertion that the roughening effect (at the same reactivity) is a function only of the size of the subelements. Thus within two minutes' simulation time, all surface roughening effects should be at steady state.

It is interesting to note that, based on theoretical derivations, the expected conversion functions for a square disc and a circular disc are identical. When the simulation results for a circular disc and a square disc with the same starting

edge area are compared, this is also found to be the case, as shown in Figure 5-59.

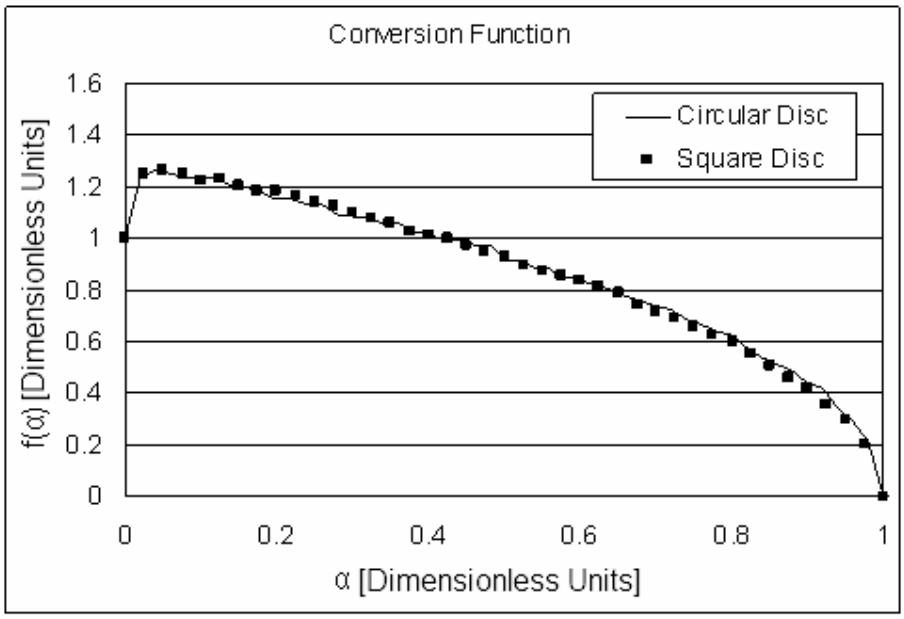


Figure 5-59: Comparison of conversion function for square and circular discs

Thus simulation appears to perform satisfactorily as a representation of disc- or flake-like behaviour. Firstly, the development of a new surface at the pinnacle of a notch in a flat surface will be investigated. A visual representation of the notch is shown in Figure 5-60.

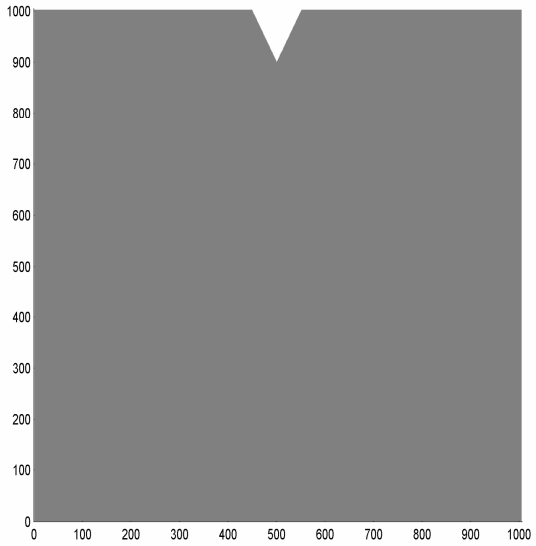


Figure 5-60: Simulated representation of a notch

The surface is allowed to react only from the top face under the same reaction parameters used previously. The progression of the notch is shown in Figure 5-61.

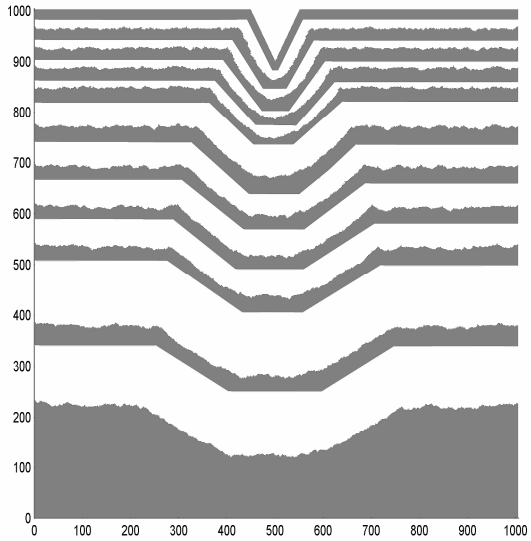


Figure 5-61: Oxidation progression of a notch

The simulated behaviour is exactly in line with the expectations discussed in the previous section. At first, a rounded shape is initiated at the pinnacle of the convex angle. As this shape propagates into the edge, it tends to flatten out until the roundness achieved approximates a flat surface. At this point the new flat surface moves at exactly the same rate as the original surface and the depth of the notch clearly does not grow. The depth of the notch is approximately equal to the starting depth, reinforcing the idea that as soon as the notch is oxidised, an infinitesimal flat surface results, which immediately recedes at a constant rate perpendicular to its surface.

These observations substantiate the earlier theoretical discussion and lend credence to the model's ability to simulate this edge phenomenon. Two more aspects are visible. Firstly, all edges attain a certain degree of roundness and despite the edge progression looking similar to the approximation of Figure 5-40, the angle of the notch is continually decreasing. Hence the notch is flattening out while retaining its original depth. Secondly, the other edge structure of

importance mentioned earlier is a surface irregularity. A schematic representation of such a structure in the simulation is shown in Figure 5-62.

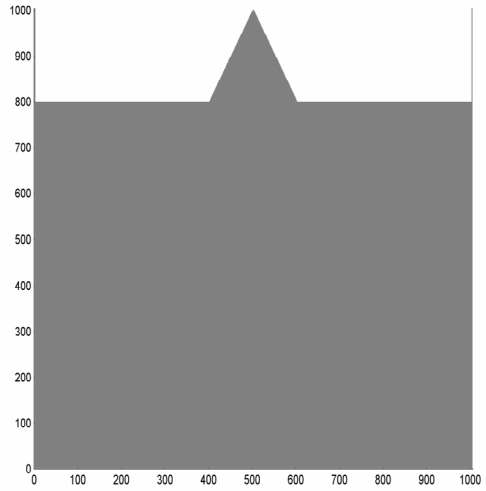


Figure 5-62: Simulated representation of a surface irregularity

Again the surface is allowed to react only from the top face under the same reaction parameters. The progression of the irregularity is shown in Figure 5-63.

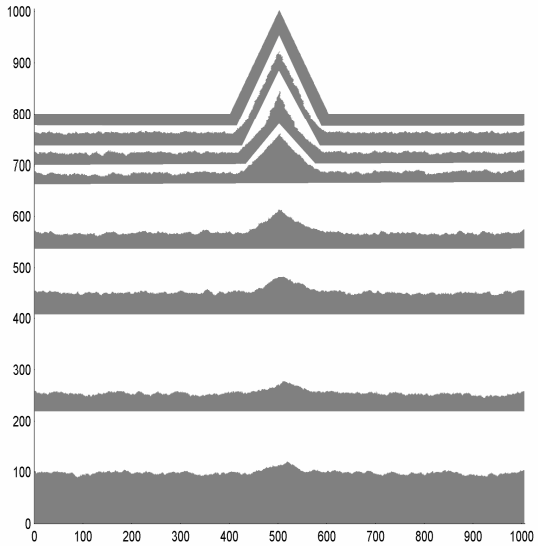


Figure 5-63: Oxidation progression of a surface irregularity

The progression is as expected from the theoretical discussions. The irregularity rapidly diminishes, developing a rounded nature at its convex angles. On the whole, this appears to be a simple and effective way to simulate the oxidative progression of virtually any geometric shape. However, for flake-like particles with internal structural irregularities or cavities, active surface area development is not a simple declining function. It is a complex interplay of the active surface area growth of the cavity which is enlarging, offset by the shrinkage of the overall flake geometry. For example, consider the flake structure shown in Figure 5-64, which has two fissures cut into the centre of the flake in the shape of a cross. A square flake has been chosen in this case, but, as pointed out earlier, the expected conversion behaviours for a square and a circular flake are virtually identical.

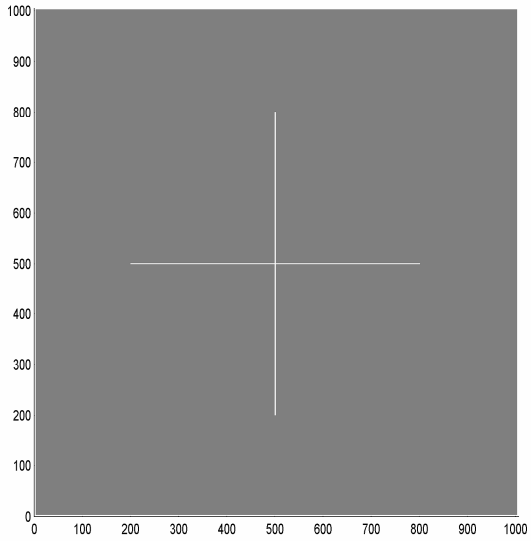


Figure 5-64: Reconstruction of flake structure with fissures

This structure is based on the microstructure observed for RFL graphite in the previous section. From this point forward, the investigation will focus mainly on relating the simulation to the observed behaviour for RFL graphite and its derivatives. The reason for this is the ideal model nature of the RFL material in terms of its large, homogenous flake-like microstructure for the fundamental modelling approach developed and applied in this section. Also, the use of RFL as the model structure eliminates to a large degree the need for a multilayered

simulation. On the whole, the particles are of similar size and shape with fairly intact, flat edges during oxidation, allowing approximation as a single sheet.

The RFL flakes have similar fissures, albeit in a more random orientation, presumably where veins of naturally occurring minerals were trapped within the graphite during formation. The active surface area development for this structure is easily simulated. The simulated ASA development normalised to the initial ASA, i.e. the simulated conversion function, is shown in Figure 5-65. This curve is compared with the conversion function determined experimentally for RFL graphite, shown earlier.

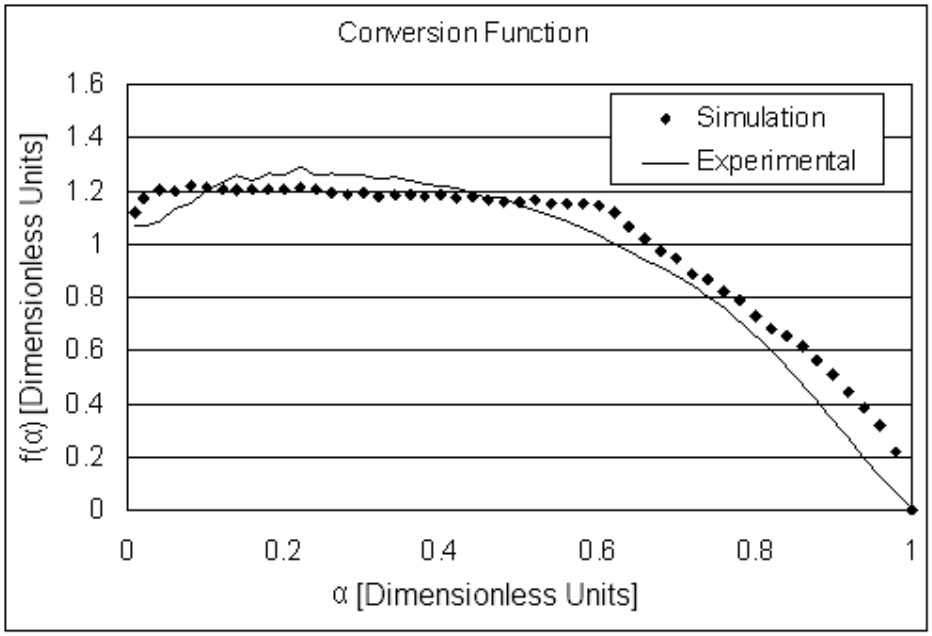


Figure 5-65: Simulated ASA development of flake structure with fissures

The two functions are remarkably similar considering the rough approximation of the true flake microstructure that the simulated cross represents. Two more microstructures were presented during the SEM investigation which can be easily modelled by this simulation. The first is a flake with a very complex and highly erratic microstructure. This may be represented by randomly attaching small blocks to each other within the broader square flake, resulting in the structure depicted in Figure 5-66. The simulated conversion function for this structure, together with the RFL conversion function, is shown in Figure 5-67.

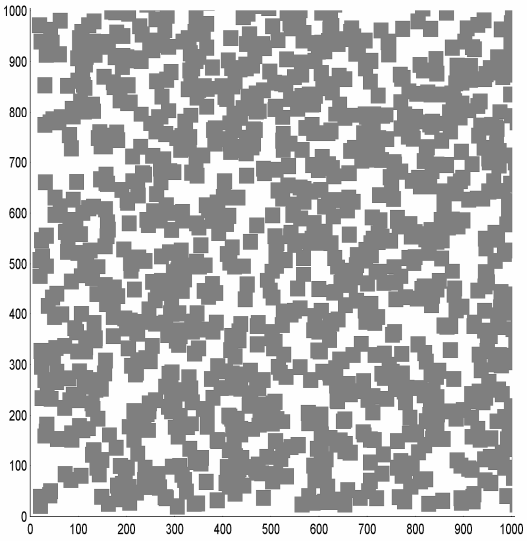


Figure 5-66: Reconstruction of a random, erratic flake structure

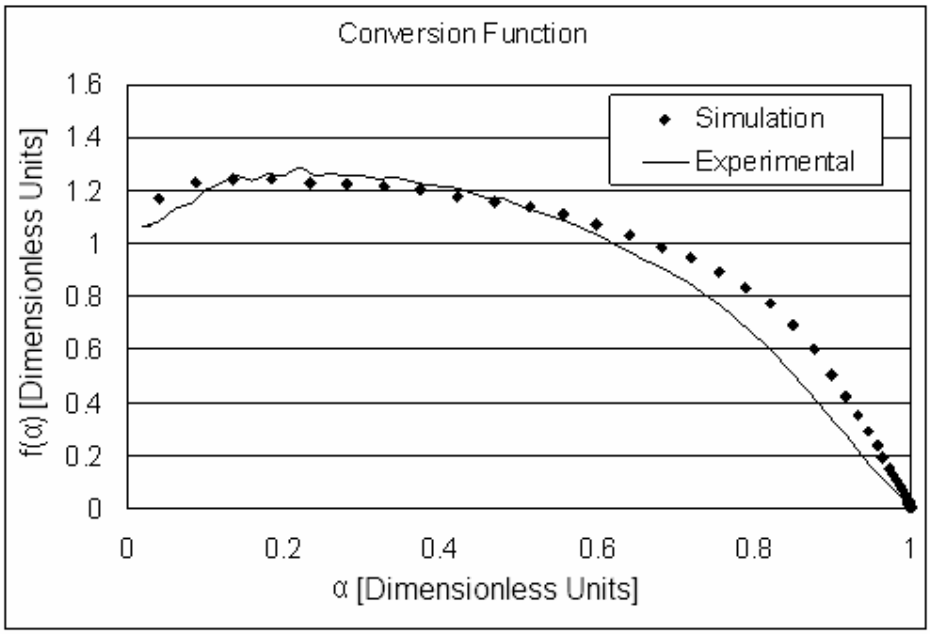


Figure 5-67: Simulated ASA development of a random, erratic flake structure

Again the simulation shows a close resemblance to the experimentally observed conversion function. Finally, the active surface area development of a flake with a few discrete, randomly placed holes is simulated. The origin of these pits is unknown and they could be caused by minute catalytic particles or lattice

defects. Either way, their formation is assumed to be very quick and the only effect relevant to the overall active surface area is expected to be their outward growth. This structure is shown schematically in Figure 5-68.

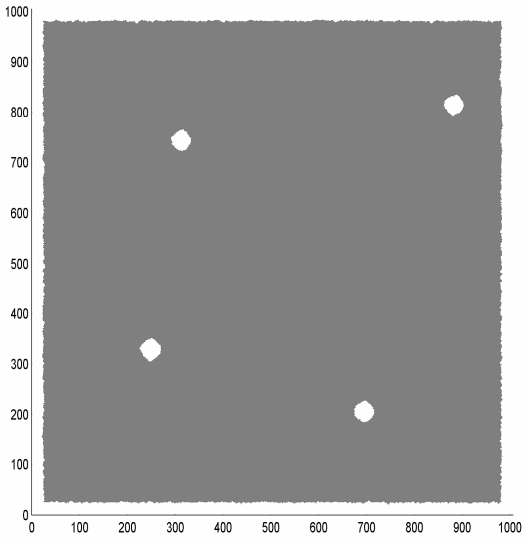


Figure 5-68: Reconstruction of a pitted flake structure

Since the holes are placed randomly, it is necessary to repeat the experiment to obtain an average. The average value for five repeat simulations is compared with the RFL conversion function in Figure 5-69.

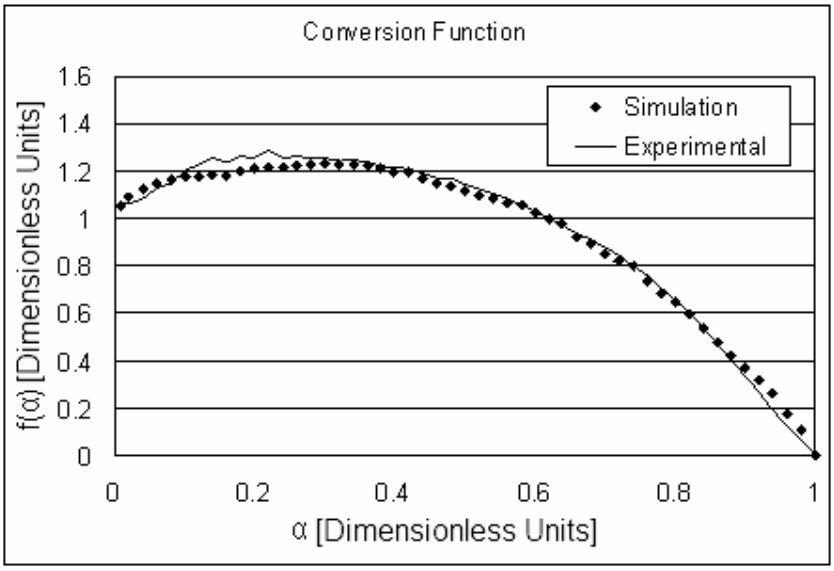


Figure 5-69: Simulated ASA development of a pitted flake structure

In this case the best approximation of the experimentally observed behaviour is obtained. All three simulations model direct representations of physically observed microstructures within the graphite during oxidation. Thus it is unlikely that any particular one of the modelled structures fully represents the true sample behaviour. Instead, it is highly likely that the observed behaviour is a mixture of these and possibly other structures. Of course, it would be impossible to simulate the ASA development of each flake individually. It is currently extremely difficult to measure the very low active surface area of graphite, especially as it develops *in situ* during the oxidation. Thus it is not possible to prove explicitly that the oxidation is governed solely by ASA development.

However, these simulations clearly illustrate the fact that it is possible to represent the reaction rate curve, as a function of conversion, based solely on active surface area considerations. Furthermore, the development of these active surface area structures is easily linked to directly observed microstructures in the oxidised graphite flakes, providing compelling evidence that active surface area development can account for at least one of the observed categories of conversion function, i.e. conversion functions where the reaction rate first increases and then decreases. This indicates that the initial increase in reaction rate is caused by the growth of structural defects within the macrostructure, before coalescence and overall flake shrinkage take over.

It is interesting to note that one of the graphite samples that falls into the other category, i.e. conversion functions that decline across the entire range of conversion, is the purified RFL material: PRFL. However, to fully describe the behaviour of this material, an additional consideration is necessary, namely the particle size distribution as described in the next section.

## 5.7 Particle size distribution effects

The as-received RFL material was wet sieved in ethanol to a fraction between 200 and 250 µm. To a large extent this negated any effects due to a particle size distribution. However, during heat treatment impurities were evaporated from large fissures within the particles, inevitably resulting in particle fracture and the creation of a particle size distribution. Thus to fully describe the

behaviour of the material after treatment it was necessary to take this effect into account.

The easiest way to examine the effect of a particle distribution on the observed conversion function is to subdivide the distribution into discrete segments, allow each segment to react on its own as a function of time and at each time interval sum over the entire distribution to obtain the true global behaviour. Consider the distribution of discs with particle radii as shown in Figure 5-70, where $n_{part}$ is the number of particles having a specific particle radius, $r_{part}$.

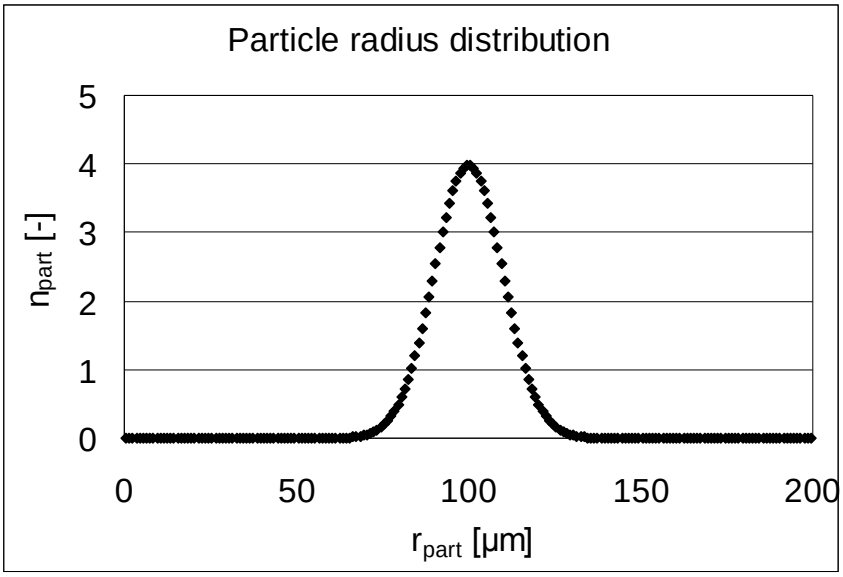


Figure 5-70: Particle radius distribution

Based on Eq. (5.26), the following expression holds:

$$\mathrm{R}_{\mathrm{T0}} = \frac{d\alpha}{dt} = k^{0}_{ASA}(T)ASA_0 f^{0}(\alpha) \quad (5.51)$$

but

$$ASA_0 = 2\pi r_{t=0} d \quad (5.52)$$

Thus for each particle radius a unique version of expression (5.51) exists. Expression (5.51) may be integrated as follows:

$$\int_0^{\alpha} \frac{d\alpha}{f^0(\alpha)} = k_{ASA}^0(T) ASA_0 \int_0^t dt \quad (5.53)$$

which yields:

$$g^0(\alpha) = k_{ASA}^0(T) ASA_0 t \quad (5.54)$$

Assuming the conversion function can be numerically integrated to find $g^0(\alpha)$, the value of this function can be calculated at each time interval for each of the respective particle radii. Using a look-up function, the corresponding value of conversion, $\alpha$, at that time can be found since

$$m = m_0(1-\alpha) = \pi r_{t=0}^2 d \rho_C (1-\alpha) \quad (5.55)$$

The mass of each particle can also be determined and the total mass can be calculated by multiplying each particle mass by the number of particles and summing across all radii. The result of this procedure applied to the ideal disc function is shown in Figure 5-71.

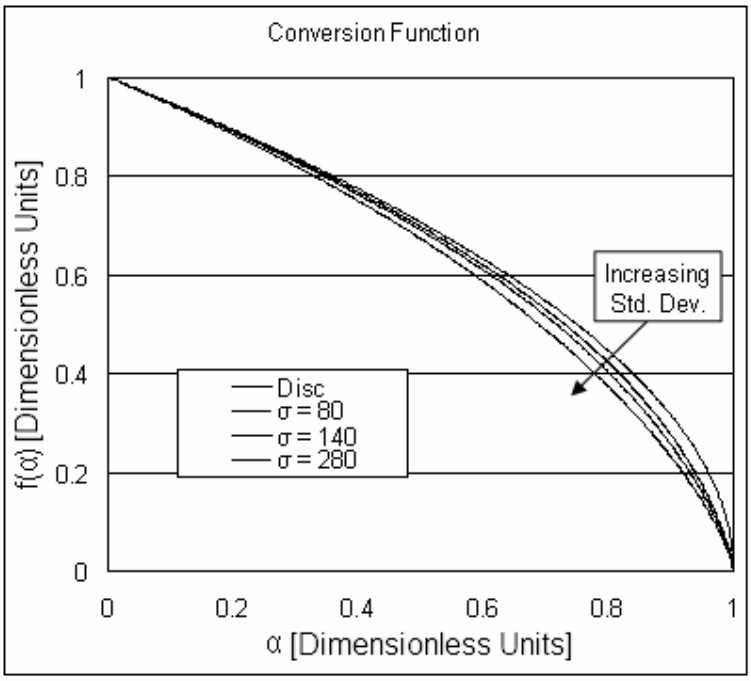


Figure 5-71: Effect of particle distribution on disc behaviour

The effect is small but noticeable: as a progressively larger standard deviation is applied, the conversion function becomes more linear. The approach can be generalised under two assumptions:

- The active surface area of the particle scales linearly with the characteristic dimension.
- The particle mass scales with the square of the characteristic dimension.

Both of these assumptions are also valid when considering a square flake as opposed to a disc. Returning to the observed conversion function for the purified RFL graphite (PRFL), one notices that the conversion function of this material initially rapidly declines, followed by a more gradual decay. As mentioned during the microstructural investigation, this graphite exhibits fine surface structures caused by the evaporation of impurities from the graphite flake lattice. The model graphite shown in Figure 5-72 was therefore considered as an approximation of this structure. This model contains a variety of randomly shaped holes at the flake edge.

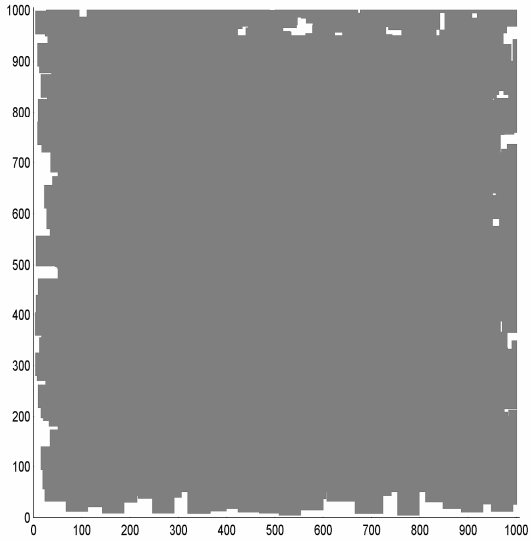


Figure 5-72: Reconstruction of the fine edge structure of the purified flake

The conversion function for this model is shown in Figure 5-73, compared with the experimental conversion function for PRFL graphite.

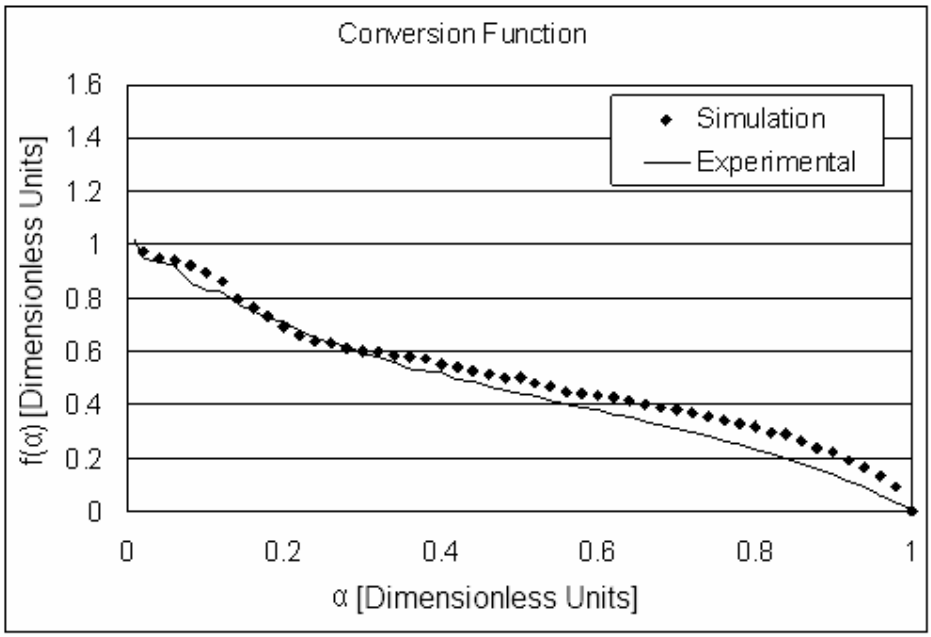


Figure 5-73: Simulated ASA development of flake with fine edge structure

The agreement is very good, with the exception of a slight deviation at high conversions. Since this model is roughly a square flake, the assumptions mentioned earlier are satisfied. If a small particle size distribution is now applied to this conversion function, the composite model result is as shown in Figure 5-74, again compared with the experimental conversion function for PRFL graphite.

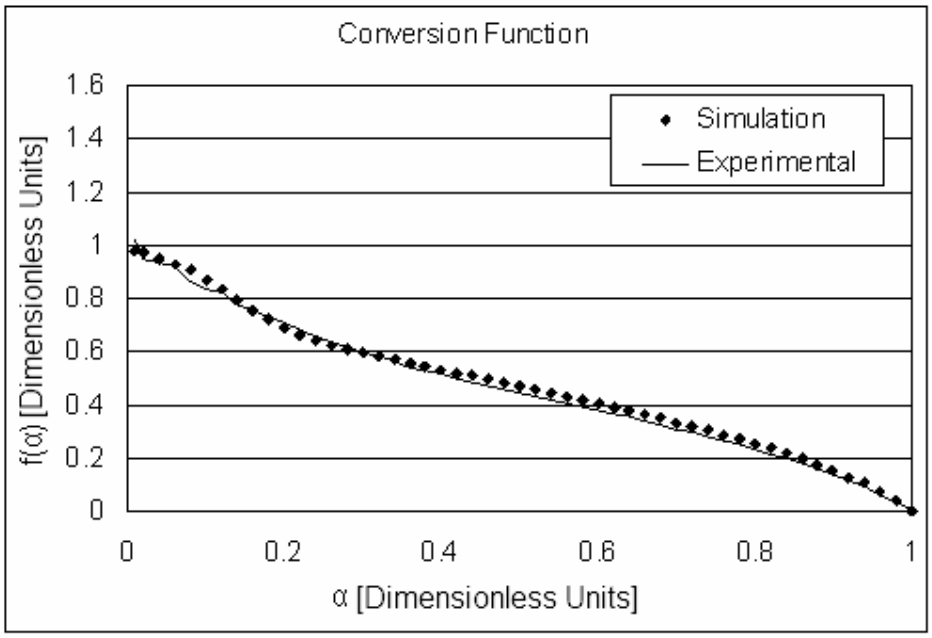


Figure 5-74: Simulated ASA development of flake with fine edge structure – small particle size distribution

There is excellent agreement between this model and the experimentally observed conversion function. Thus a purified RFL graphite flake is adequately represented by a square flake with a fine edge structure, in conjunction with a small particle size distribution. It is unlikely that the sample undergoes gross structural changes during the heat treatment. Rather, it was observed that the impurities are removed. As stated earlier, it is difficult to determine whether the pits mentioned previously are caused by the action of catalytic impurities or lattice defects. Instead, the pits were assumed to exist at the start of the simulation and simply allowed to evolve.

If the pits were caused by catalysts, they were removed during the heat treatment. On the other hand, if the pits were created by lattice defects, it is possible that these were annealed during heat treatment, depending on the type of defect that was present. In either case, the re-incorporation of pitting behaviour into the model that appears to represent the purified material should simply yield the as-received behaviour. To a large extent this is found to be the case, as can be seen in Figure 5-75. Here the PRFL model suggested above is simply modified to include several randomly positioned holes. The conversion function obtained is compared with the as-received conversion function.

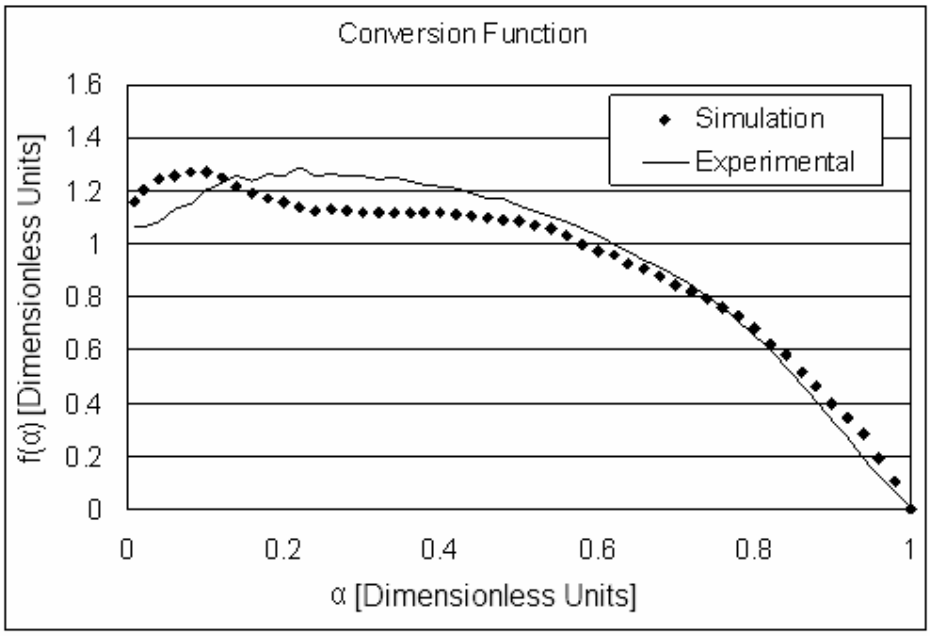


Figure 5-75: Simulated ASA development of PRFL model with holes

The agreement of the simulation with the experimental observation is not perfect, especially at low conversions. However, for a large part of the conversion range the pitting-modified PRFL model acceptably recovers the as-received behaviour. Several reasons may exist for the inaccuracy of the simulation at low conversion, including differences between the pitting model and the other applicable models, i.e. fissures or erratic structures. Despite this, the model still provides a credible explanation for the observed transition from as-received to purified material, which is consistent with expectations of the heat treatment.

## 5.8 Surface complex effects

The very low active surface area and hence low surface complex concentrations found in graphite make it very difficult to study the effects these complexes have on the reaction. From the literature survey it is clear that these complexes are still fairly poorly understood and their contribution to the kinetics is unclear. Several possible reaction schemes have been proposed to account for the kinetic pathways whereby surface complexes play a role in the carbon-oxygen reaction. Two simplified reaction schemes were chosen to represent two key aspects of the proposed reaction pathways:

- The first scheme involves the formation of two separate surface complexes, one stable and one unstable, plus an interconversion reaction between the two species. This scheme is represented by the following reactions:

$$C_f + O_2(g) \xrightarrow{k_1} C^{stable}(O_2) \quad (5.56)$$

$$C_f + O_2(g) \xrightarrow{k_2} C^{unstable}(O_2) \quad (5.57)$$

$$C^{unstable}(O_2) \xrightarrow{k_3} CO_2(g) + C_f \quad (5.58)$$

$$C^{stable}(O_2) \xrightarrow{k_4} C^{unstable}(O_2) \quad (5.59)$$

- The second scheme also involves the formation of two separate surface complexes, one stable and one unstable. However, in this case the stable surface complex is considered to be a reactionary intermediate. This is similar to the scheme suggested by Ahmed and Back [203] and to the three-step semi-global mechanism suggested by Hurt and Calo [214]. This scheme is represented by the following reactions:

$$C_f + O_2(g) \xrightarrow{k_1} C^{stable}(O_2) \quad (5.60)$$

$$C_f + O_2(g) \xrightarrow{k_2} C^{unstable}(O_2) \quad (5.61)$$

$$C^{unstable}(O_2) \xrightarrow{k_3} CO_2(g) + C_f \quad (5.62)$$

$$C^{stable}(O_2) + O_2(g) \xrightarrow{k_4} C^{stable}(O_2) + CO_2(g) \quad (5.63)$$

These schemes allow the effects of the surface complex phenomena on the overall conversion function to be explored. However, in order to incorporate these reaction schemes into the analytical modelling technique introduced in

Section 5.3, a few additional considerations are necessary. Firstly, the underlying assumption for the analytical model is a homogeneous edge-recession rate. For the purposes of approximating the experimental behaviour this is adequate, but when it becomes necessary to keep track of the surface species present during this recession, difficulties arise. In essence, the analytical disc model assumes that all the random edge recession that took place in the real experiment during a given time step can be accumulated, and a new average diameter is calculated which represents the new active surface area. Thus all the active sites are evenly redistributed along the new circumference of the disc.

However, in the current situation these sites are occupied by different surface complexes, some stable and some unstable, while some sites are vacant. A method for calculating the redistribution as a function of the shrinking diameter is not immediately evident. For example, assume that half the surface is occupied by unstable surface complexes, of which half desorb and half remain during a given time step. The other half of the surface is occupied by stable surface complexes that undergo no change. The mass of carbon desorbed with the surface complexes represents the amount of carbon reacted and can be used to calculate a new particle mass, which in turn allows a new diameter to be determined. However, this will lead to a new active surface area which is smaller than the original surface. Presumably, however, for each active surface complex desorbed, a new vacant site was formed. Thus, in total, the number of sites, i.e. vacant sites and sites with both unstable and stable surface complexes, has remained the same from a site balance perspective. However, this is in contradiction with the new active surface area, which is smaller and represents a reduction in the total number of sites.

A simplified approximation would be to calculate the total amount of active surface area available at a given time using the current mass and the circular disc model. Based on an initial starting value for the stable and unstable surface complex coverage, a change in each of these values can be calculated on the basis of one of the reaction schemes proposed earlier. The number of free or vacant sites is then calculated by difference, between the total number of sites and those occupied by the surface complexes. Thus the surface complexes remain the same, but additional vacant sites are created only as allowed by the available surface area. To fully account for the vacant site balance, a far more

detailed understanding of site creation and regeneration during desorption is necessary, based on the graphite crystal structure.

For reaction scheme one, mass loss occurs via reaction (5.58) only, and thus the reaction rate can be defined as:

$$\frac{dm}{dt} = -k_3 C_U \quad (5.64)$$

where $C_U$ represents the surface area occupied by the unstable surface complex.

A comparison with Eq. (5.22) reveals that:

$$\frac{d\alpha}{dt} = \frac{-1}{m_0}\frac{dm}{dt} = \frac{k_3 C_U}{m_0} = \frac{k_{ASA}(T)ASA}{m_0} \quad (5.65)$$

Thus $k_3 = k_{ASA}(T)$ and the values given in Table 5-1 may be used. The ASA of vacant sites may be calculated by $C_F = ASA - C_U - C_S$, where $C_S$ is the ASA occupied by stable surface complexes. From the reaction expressions, the changes in the stable and unstable ASAs may be calculated as:

$$\frac{dC_U}{dt} = k_2 C_F - k_3 C_U + k_4 C_S \quad (5.66)$$

$$\frac{dC_S}{dt} = k_1 C_F - k_4 C_S \quad (5.67)$$

Based on these expressions, an analytical model can be constructed using the ideal disc model for the active surface area calculation, i.e. $ASA = ASA_0 (1 - \alpha)^{0.5}$. The arbitrarily chosen starting set of model parameters are summarised in Table 5-8.

Table 5-8: Surface complex model parameters

| | | |
|---|---|---|
| $k_1$ | 0 | $g/m^2/s$ |
| $k_2$ | 1 | $g/m^2/s$ |
| $k_3 = k_{ASA}(T)$ | 0.0062 | $g/m^2/s$ |
| $k_4$ | 0 | $g/m^2/s$ |
| D | 225 | µm |
| d | 20 | µm |
| Δt | 0.01 | min |
| $E_A$ | 180 | kJ/mol |
| $T_0$ | 700 | ºC |
| β | 0 | ºC/min |
| $ASA_0$ | 0.1 | $m^2/g$ |

A final assumption regarding the initial distribution of surface complexes is needed. As a simple starting point, the sample is presumed to be initially fully covered by the unstable surface complex. The reaction rate constants for reactions (5.56) and (5.59) are set to zero and the rate constant for reaction (5.57) is set arbitrarily high. This amounts to conditions similar to those present in the original disc simulation. The resulting simulated conversion function is shown in Figure 5-76, from which it can be seen that the model suitably recreates the expected disc behaviour, indicating correct model operation.

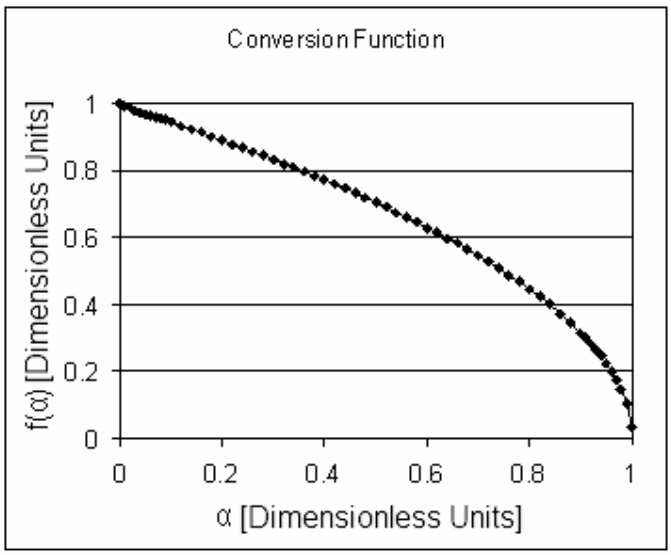


Figure 5-76: Conversion function for surface complex model 1

Furthermore, the active site coverage may be calculated where $X_i$ represents the fraction of the total ASA occupied by a given surface complex (U or S) or vacant/unoccupied surface area (F). A plot of these fractions for the current reaction parameters is shown in Figure 5-77.

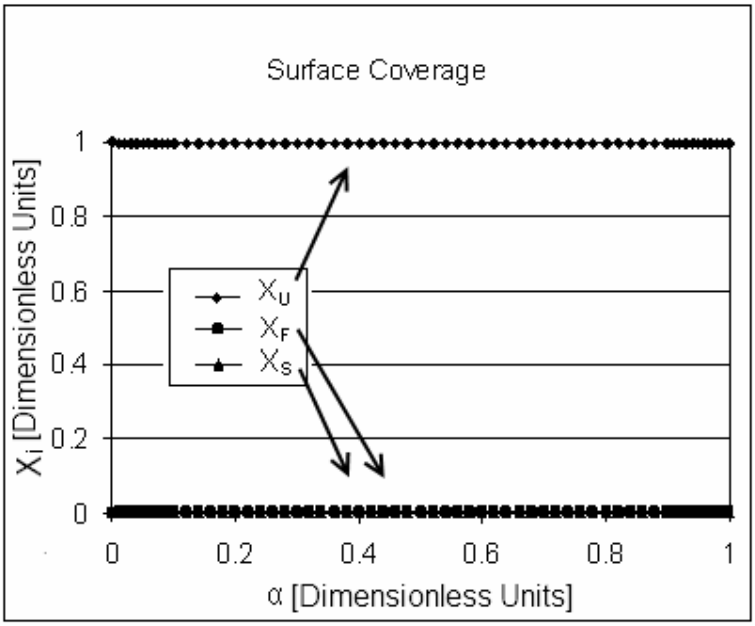


Figure 5-77: Surface coverage fractions for surface complex model 1

As expected, the surface is completely covered by unstable surface complexes and no vacant sites or stable complexes are formed. A slightly more realistic scenario involving a slightly lower reaction rate, the result of setting $k_2$ = 0.012, is shown in Figure 5-78.

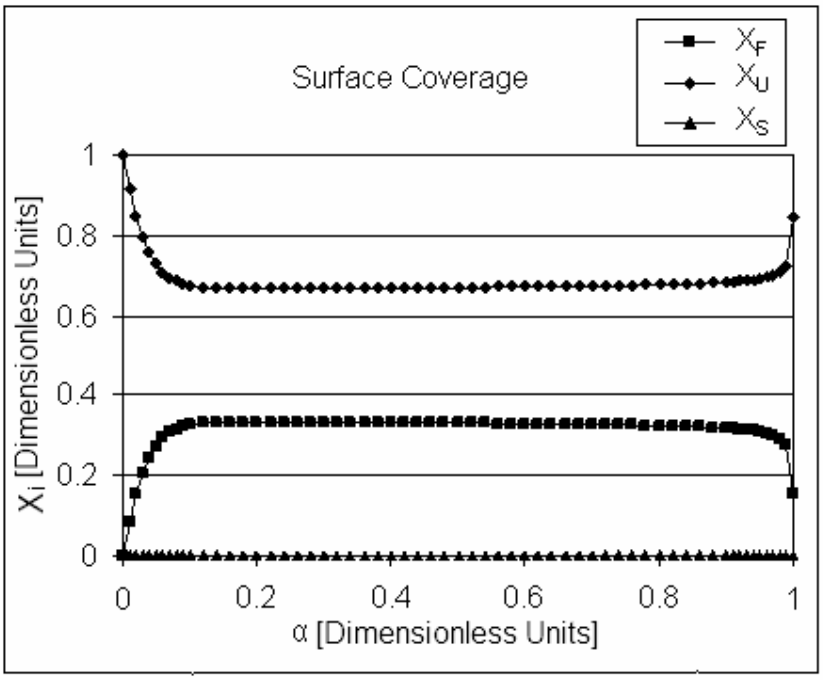


Figure 5-78: Surface coverage fractions for surface complex model 2

In this case a pseudo-steady state develops between the vacant sites and the unstable surface complexes, with the steady state surface complex fraction equal to $k_3/(k_3 + k_2)$. Beyond this point the disc behaviour controls the reaction rate and subsequently the shape of the conversion function, as shown in Figure 5-79. The standard disc model with a multiplier of 0.66 is added to this figure for comparative purposes.

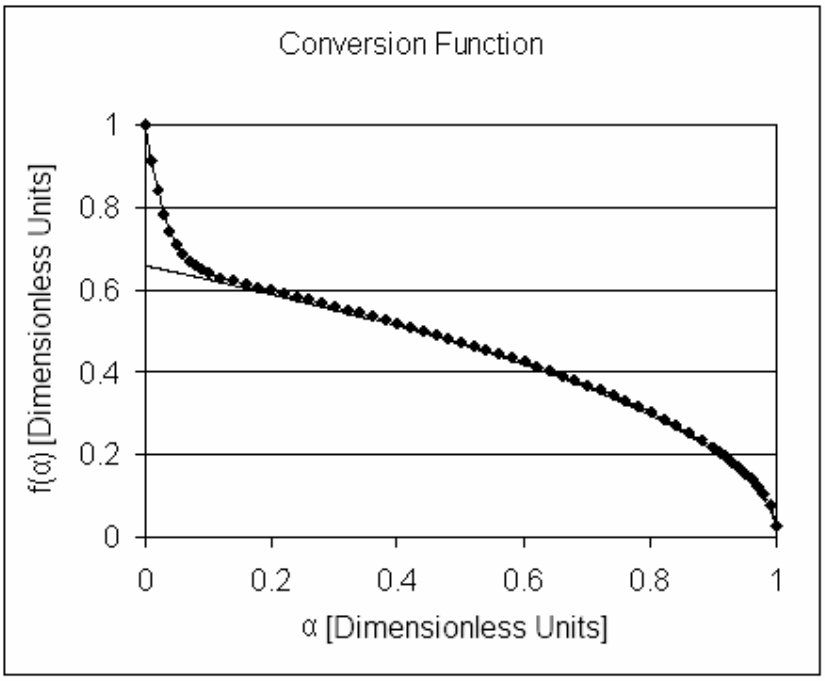


Figure 5-79: Conversion function for surface complex model 2

If the active site conversion to unstable surface complex is dropped further, for example to $k_2$ = 0.003, the population reverses to being dominated by vacant sites, as shown in Figure 5-80. In this extreme case the reaction rate is severely depressed, but the conversion function is affected only during the initial part of the reaction, as seen in Figure 5-81.

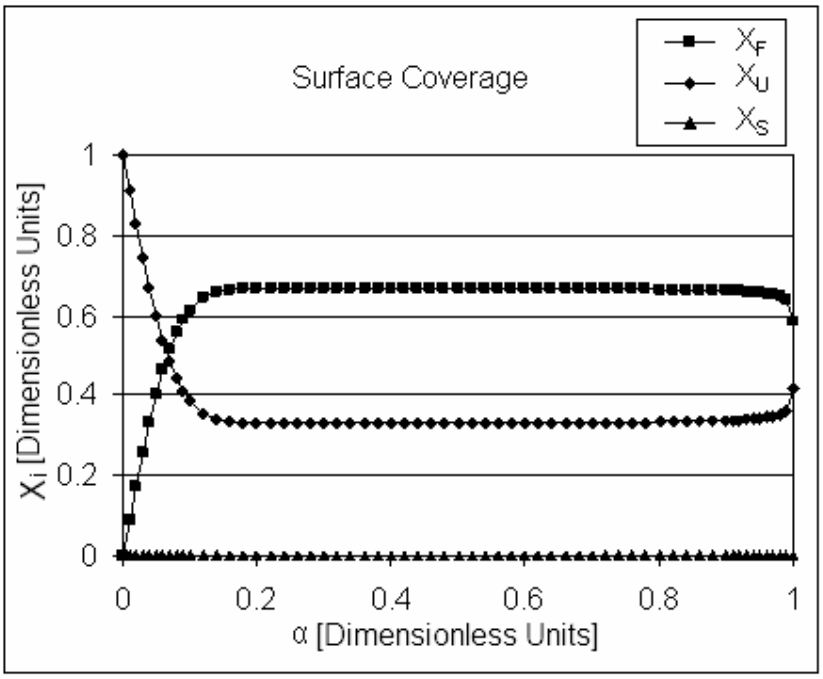


Figure 5-80: Surface coverage fractions for surface complex model 3

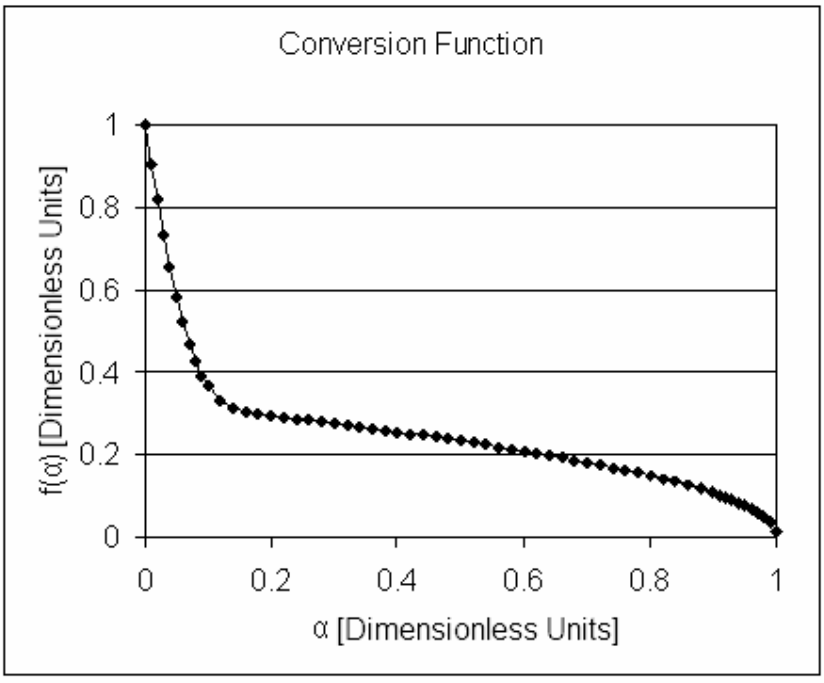


Figure 5-81: Conversion function for surface complex model 3

It is possible to extend this effect to higher conversions by decreasing both reaction rate constants. For example, shown in Figure 5-82 is the case for

$k_2$ = 0.0015, $k_3$ = 0.0015. However, it should be noted that at this point the reaction rate is no longer representative of the experimentally observed reaction rate.

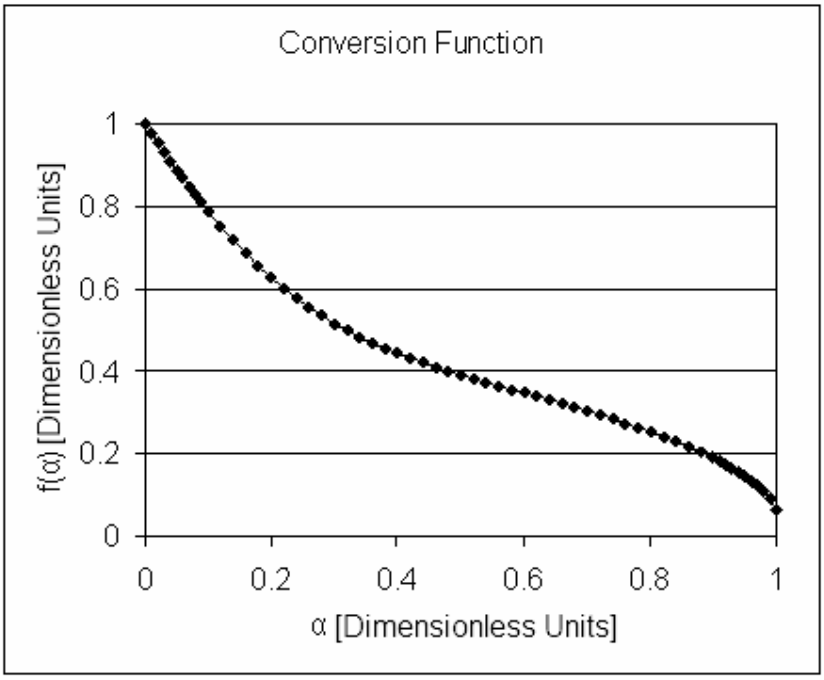


Figure 5-82: Conversion function for surface complex model 4

Reverting to the more realistic configuration of $k_2$ = 0.012, $k_3$ = 0.0062, it is interesting to note the case where the active surface area is presumed to be initially covered by vacant sites alone. The result for this simulation is shown in Figure 5-83.

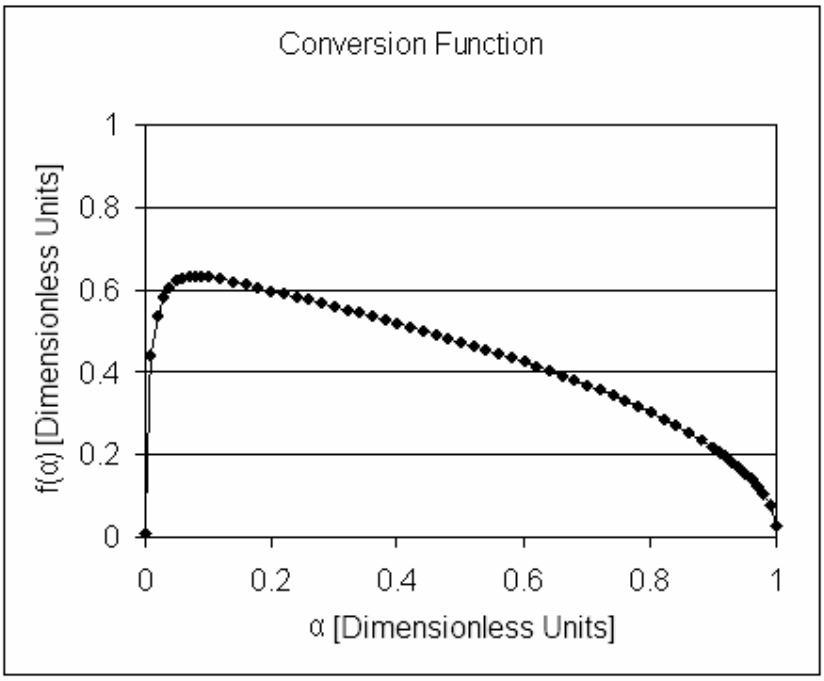


Figure 5-83: Conversion function for surface complex model 5

In this case the reaction rate is initially zero and then rapidly increases as the unstable complexes accumulate until the pseudo-steady state is achieved, at which point the disc behaviour takes over. The stable surface complex may now be introduced by setting the formation rate, $k_1$, to a non-zero value. If the stable complex is not allowed to decay into an unstable complex, these complexes simply accumulate and lead to the unrealistic situation where a zero reaction rate is achieved before complete conversion, as shown in Figure 5-84 for $k_1$ = 0.001, $k_2$ = 0.012, $k_3$ = 0.0062, $k_4$ = 0.

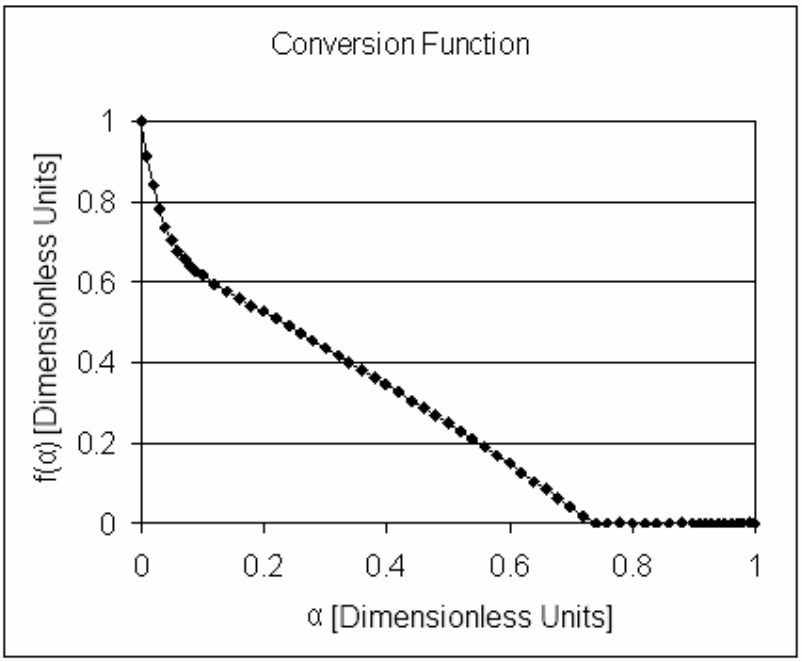


Figure 5-84: Conversion function for surface complex model 6

If the decay rate is now set to a non-zero value, e.g. $k_4$ = 0.001, a more complex behaviour is possible where the stable complex slowly accumulates as the reaction progresses, as shown in Figure 5-85.

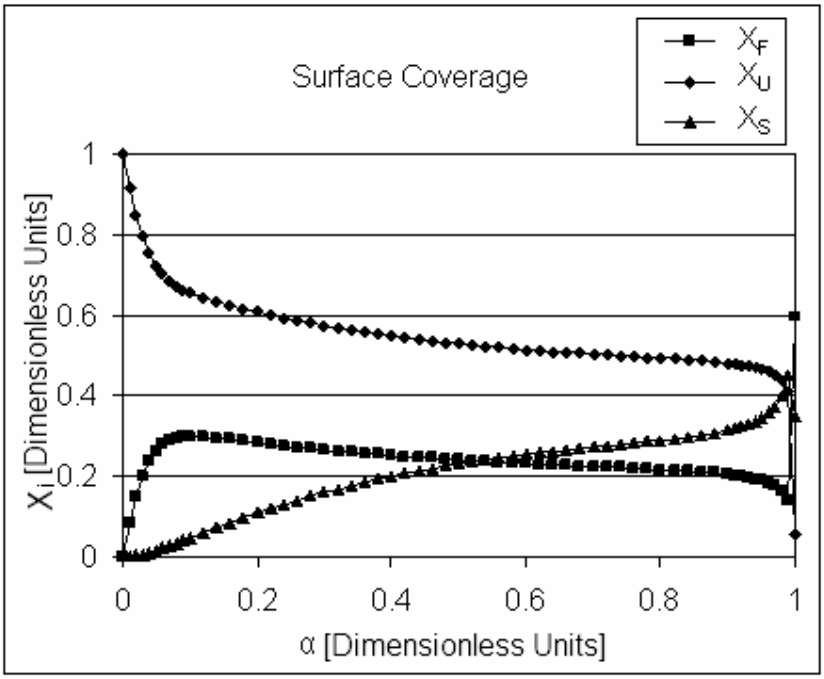


Figure 5-85: Surface coverage fractions for surface complex model 7

In this case a significant departure from the expected disc behaviour is observed, as shown in Figure 5-86.

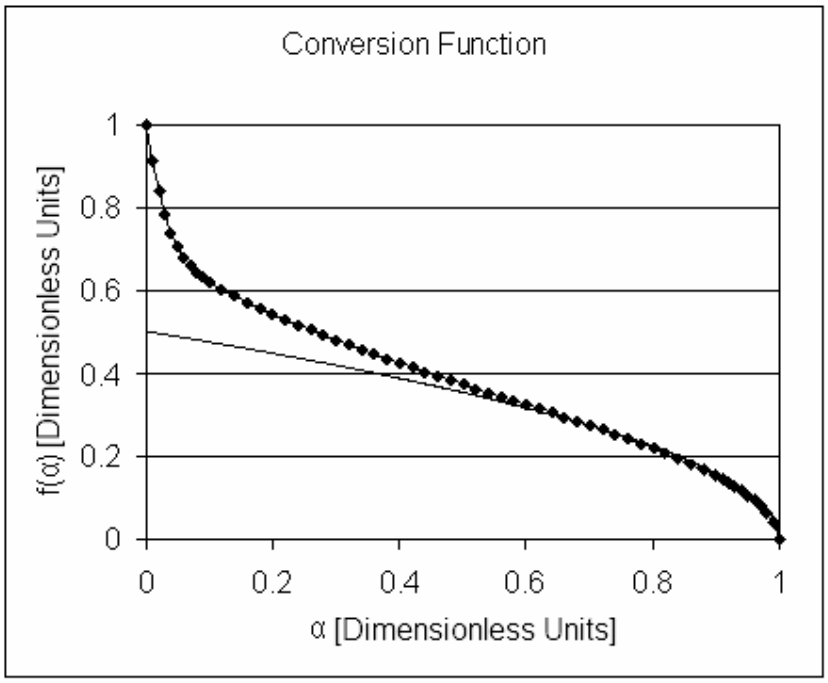


Figure 5-86: Conversion function for surface complex model 7

At this point there are numerous possibilities for plausible configurations of reaction rates. One may allow a more rapid accumulation of the unstable surface complexes, at which point a three-way pseudo-steady state will be developed, as shown in Figure 5-87.

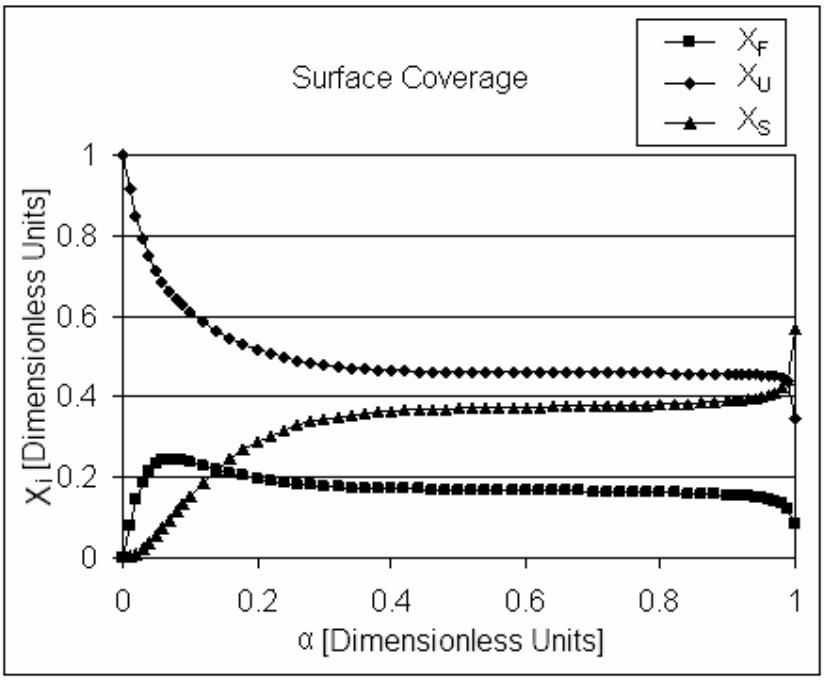


Figure 5-87: Surface coverage fractions for surface complex model 8

Another configuration may allow a more gradual accumulation until the unstable complex dominates the distribution, as shown in Figure 5-88.

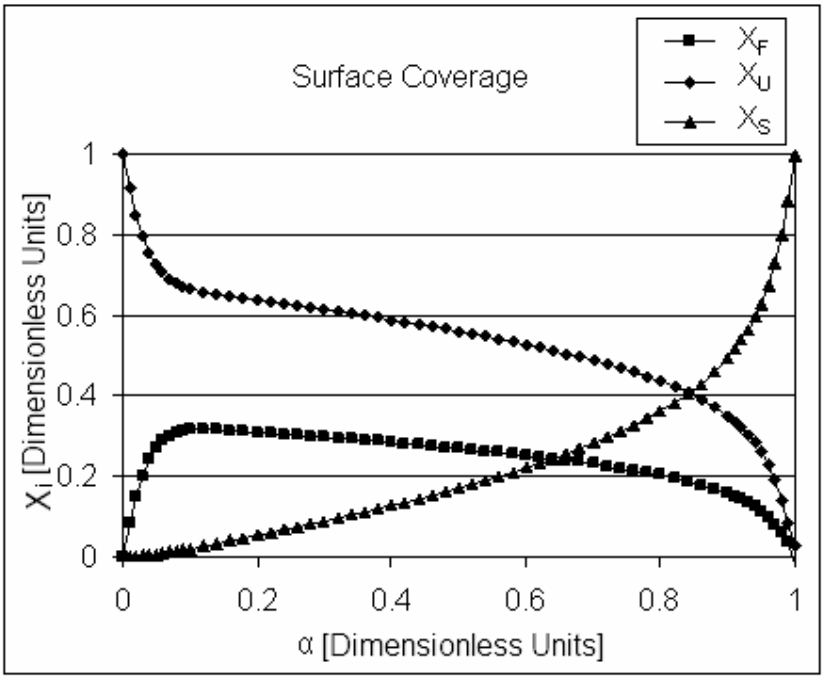


Figure 5-88: Surface coverage fractions for surface complex model 9

Unfortunately, with no *a priori* method of selecting between the possible configurations, drawing pertinent conclusions regarding these complexes becomes difficult. A similar qualitative investigation can be applied to the second reaction scheme, beginning with a configuration that yields behaviour identical to that of the previous scheme, as shown in Figure 5-89, with $k_1$ = 0.0002, $k_2$ = 0.012, $k_3$ = 0.0062, $k_4$ = 0.002.

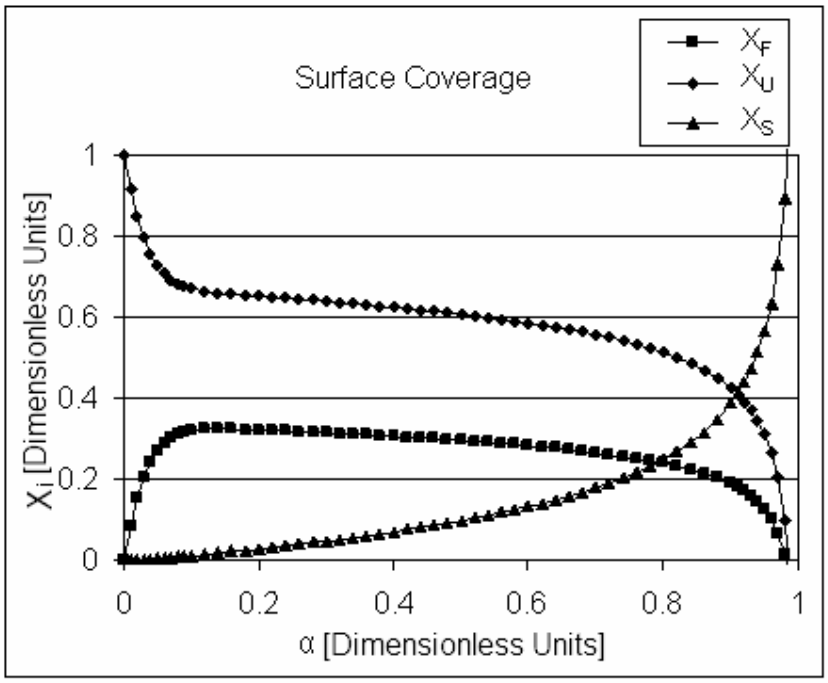


Figure 5-89: Surface coverage fractions for surface complex model 10

However, based on the literature survey, this secondary reaction is expected to have a significantly higher reaction rate. If the rate constant is increased to $k_4$ = 0.02, the conversion function shown in Figure 5-90 is obtained. This figure demonstrates a critical flaw in this scheme. Because the stable complexes have no reaction pathway to decay, they remain on the surface until full conversion. However, they continually uplift the reaction rate, leading to the unfeasible situation where a non-zero reaction rate is achieved at full conversion. This scheme is therefore unlikely to be correct.

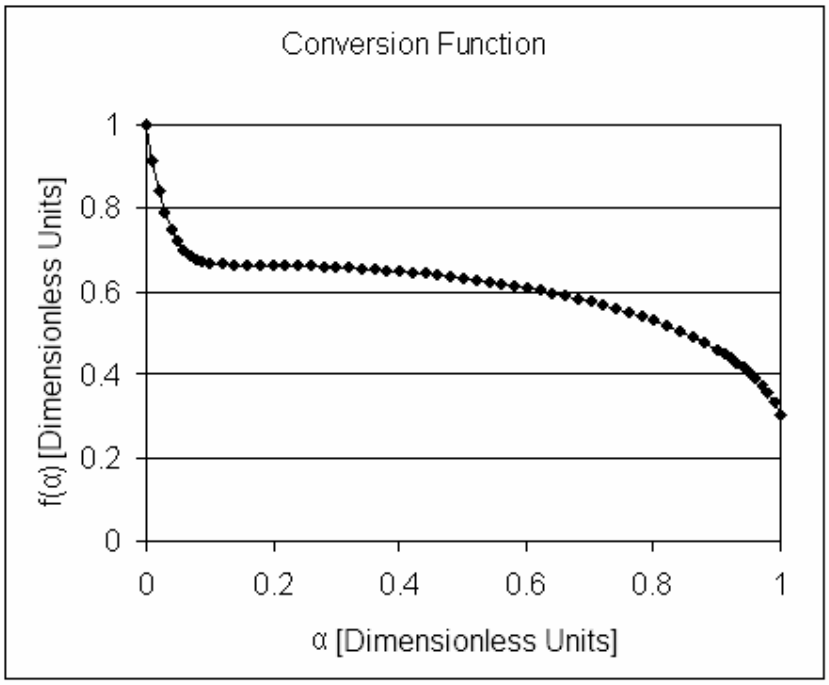


Figure 5-90: Conversion function for surface complex model 10

This section illustrates the myriad of complex influences that two simple kinetic schemes involving surface complexes can have on the observed conversion functions. However, in most cases the underlying geometric conversion function remains largely intact over large regions of conversion. Thus it may be tentatively stated that surface complex development mainly influences the reaction rate during the initial regions of burn-off, until a pseudo-steady state develops between the surface species. Beyond this point the inherent active surface area development takes over and governs the reaction rate.

Although a variety of influences on the shape of the conversion function are possible, none can explain the rising, then decreasing nature of a large portion of the observed conversion functions. Furthermore, these surface complexes are expected to have temperature-dependent formation and decay characteristics. Such behaviour is in direct contradiction to the observation that for a given sample of graphite the conversion function remains consistent, not only across a wide range of isothermal temperatures, but also during non-isothermal testing. Furthermore, these effects are not expected to vary from sample to sample. All the samples considered are highly crystalline graphite and thus surface heterogeneity should be minimal. These complexes are therefore

unlikely to explain sample-to-sample variations in the observed conversion functions for experiments carried out in similar temperature ranges.

Surface complex formation and the achievement of steady state is likely to be an additional factor influencing the ineffectiveness of Galwey's method at low and high conversions. Unfortunately, it is not possible to prove this influence theoretically unless the activation energy for each of the different reaction rate constants is known. Based on this investigation and the facts just stated, it is likely that surface complex development influences the oxidation and should be investigated further. However, the dominant factor that provides an explanation for the observed behaviours across the board remains the development of the active surface area.